Dynamics and Stability of Rolling Viscoelastic Tires

by

Trevor Potter

A dissertation submitted in partial satisfaction of the
requirements for the degree of
Doctor of Philosophy

in

Applied Mathematics

in the

Graduate Division

of the

University of California, Berkeley

Committee in charge:

Professor Jon Wilkening, Chair
Professor Sanjay Govindjee
Professor James Sethian
Professor Ole Hald

Spring 2013

Dynamics and Stability of Rolling Viscoelastic Tires

Copyright 2013
by
Trevor Potter

DISCLAIMER

This document was prepared as an account of work sponsored by the United States Government. While this document is believed to contain correct information, neither the United States Government nor any agency thereof, nor the Regents of the University of California, nor any of their employees, makes any warranty, express or implied, or assumes any legal responsibility for the accuracy, completeness, or usefulness of any information, apparatus, product, or process disclosed, or represents that its use would not infringe privately owned rights. Reference herein to any specific commercial product, process, or service by its trade name, trademark, manufacturer, or otherwise, does not necessarily constitute or imply its endorsement, recommendation, or favoring by the United States Government or any agency thereof, or the Regents of the University of California. The views and opinions of authors expressed herein do not necessarily state or reflect those of the United States Government or any agency thereof or the Regents of the University of California.

DE-AC02-05CH11231

Abstract

Dynamics and Stability of Rolling Viscoelastic Tires

by

Trevor Potter

Doctor of Philosophy in Applied Mathematics

University of California, Berkeley

Professor Jon Wilkening, Chair

Current steady state rolling tire calculations often do not include treads because treads destroy the rotational symmetry of the tire. We describe two methodologies to compute time periodic solutions of a two-dimensional viscoelastic tire with treads: solving a minimization problem and solving a system of equations. We also expand on work by Oden and Lin on free spinning rolling elastic tires in which they disovered a hierachy of N-peak steady state standing wave solutions. In addition to discovering a two-dimensional hierarchy of standing wave solutions that includes their N-peak hiearchy, we consider the effects of viscoelasticity on the standing wave solutions. Finally, a commonplace model of viscoelasticity used in our numerical experiments led to non-physical elastic energy growth for large tire speeds. We show that a viscoelastic model of Govindjee and Reese remedies the problem.

To Mom and Dad

Contents

Contents **ii**

List of Figures **iv**

1 Introduction **1**
1.1 Treaded tires and time periodic solutions 1
1.2 Bifurcations from steady state solutions 2
1.3 A comparison of viscoelastic models for the spinning tire 2
1.4 Layout of the present work 3

2 Continuum Mechanics: Viscoelastic Materials **6**
2.1 Kinematics 6
2.2 Balance Laws 6
2.3 The Cauchy stress tensor 7
2.4 The Reference configuration 7
2.5 Constitutive relations 9
2.6 The stored energy function 10
2.7 Viscoelastic model 11
2.8 Two-dimensional formulation 13
2.9 Domain and Boundary conditions 14
2.10 Weak formulation 17
2.11 Linearization 18

3 Time periodic and steady state solutions **20**
3.1 Time periodic solutions for the treaded tire 20
3.2 Time periodic solutions for the smooth tire 23
3.3 Steady state solutions 23
3.4 Hamiltonian structure of the elastic equations 26

4 Numerical methods **27**
4.1 Displacement formulation 27
4.2 Finite element framework 28

4.3 The discretized equations 30
4.4 Numerical solution of the discretized equations 33
4.5 Eigenvalues of the Steady State Problem 34
4.6 Numerical computation of the operator $\mathcal{U}_T$ 34
4.7 Solving the time periodic equations 36
4.8 Parallelization 38

5 Results **39**
5.1 Choice of units and constants 39
5.2 Example computation of a time periodic solution 39
5.3 Time evolution of stress of the treaded tire 42
5.4 A rotating viscoelastic oval 44
5.5 Example computation of steady state solutions and eigenvalues 44
5.6 Bifurcations of the free spinning tire 48
5.7 Instability of the linear viscoelastic model 54

6 Conclusions **62**

Bibliography **63**

A The linearized equations **66**

List of Figures

2.1 The plot on the left shows the smooth tire corresponding to the reference domain $\mathcal{B}$. The plot on the right is a treaded tire corresponding to the reference domain $\mathcal{B}_{.1,8}$. 15
2.2 The plot above shows the positioning of the road and indicates the traction forces experienced by the edge by vectors pointing upward. The vectors increase in magnitude the deeper the tire penetrates the road. The direction of rotation is also indicated. 16

3.1 The top figure is the reference configuration with material points X and $X_R = \mathbf{R}^{\mathsf{T}}(T)X$. At bottom left is the deformed configuration at time 0. At bottom right is the deformed configuration at time T, for which the tire is the same shape as at time 0. We observe that $\boldsymbol{\phi}(X_R, T) = \boldsymbol{\phi}(X, 0)$. 21

4.1 The reference element $\tilde{E}$ with nodes $\tilde{p}_{kl}$ is plotted on the left. The shape function $\tilde{\psi}_{2,3}$ is plotted on the domain $\tilde{E}$ on the right. 29
4.2 The reference element $\tilde{E}$ is mapped by $S_{4,1}$ to the r-θ plane. The grid of elements in the r-θ plane is then mapped by the polar coordinate transformation T onto the reference domain $\mathcal{B}_{.1,5}$. We also plot the grid of nodes p_{ij} in $\mathcal{B}_{.1,5}$. 30

5.1 Plot of the tire as it rotates counterclockwise from one tread to the next. Red indicates high first principal stress while blue indicates low first principal stress. 40
5.2 Plots of the evolution of the first principal stress over one revolution. The plots represent points at different distances from the hub, from furthest to closest. . 42
5.3 Plots of the evolution of the first principal stress over one revolution. The plots represent points at different locations along the edge of the tire. The top plot is at a tread peak, the bottom plot is at a tread trough, and the third plot is midway between. 43
5.4 Plots of traction over one tire revolution. The plots represent points at different locations along the edge of the tire. The top plot is at a tread peak, the bottom plot is at a tread trough, and the middle plot is midway between. 45

5.5 Plots of shear stresses of material points along the hub over one tire revolution. The plots represent points at different locations along the hub of the tire. The top plot is radially in line with a tread peak, the bottom plot with a tread trough, and the middle plot is midway between. 46
5.6 Plots of a simple oscillating mode of the oval over one period. 46
5.7 The top plot is angular displacement of the right-most tip of the oval over a full revolution of the oval. The oscillation near $0.05 - 0.15$ seconds corresponds to the opposite end (left-most tip) of the oval contacting the road. The large displacement near $0.2 - 0.27$ seconds corresponds to the right-most tip itself contacting the road. The bottom plot displays $\mathrm{Re}\,(e^{\lambda t})$, where λ is the eigenvalue corresponding to the fundamental mode. The similar frequency and rate of decay of the two plots near 0.1 seconds indicate the excitation of the fundamental mode is captured in the top plot. 47
5.8 Plots of the smallest eigenvalues of $\mathcal{A}_e[\mathbf{z}_\omega]$. Here ω_c is near 210 Hertz. 49
5.9 Plot of the λ_i and $\bar{\lambda}_i$. The leftmost X corresponds to λ_{12} while the rightmost X corresponds to λ_2. 50
5.10 Plot of eigenvectors corresponding to ω_{12} and ω_5. The plots are colored according to the displacement from the reference configuration, with red being high displacment and blue being little displacement. 50
5.11 Plot of the real $\boldsymbol{\phi}$ component of eigenvectors outside of the N-peak hierarchy discoverd by Oden and Lin. The plots are colored according to the displacement from the reference configuration, with red being high displacment and blue being little displacement. 51
5.12 Plots of the real part of a_1 for various eigenvectors. The top left plot corresponds to the $\mathbf{e}_i$. The top right plot corresponds to N-peak bifurcations with extra radial complexity. The bottom plots correspond to eigenvectors with even greater radial complexity. 52
5.13 Plot of the $\lambda_{i,2}$ and $\bar{\lambda}_{i,2}$. The leftmost X corresponds to $\lambda_{12,2}$ while the rightmost X corresponds to $\lambda_{4,2}$. 52
5.14 Plots of the smallest eigenvalues of $\mathcal{A}[\mathbf{z}^v_\omega]$ in the viscoelastic case. Here ω^v_c is near 285 Hertz. 53
5.15 Plot of eigenvectors corresponding to ω^v_{12} and ω^v_5. The plots on the top are colored according to the displacement from the reference configuration, with red being high displacment and blue being little displacement. The plots below are colored according to the frobenius norm of the viscoelastic stress tensor. 55
5.16 Plot of the real and imaginary components of the eigenvalues corresponding to the ω^v_i. The leftmost X corresponds to ω^v_{12} while the rightmost X corresponds to ω^v_3. 56

5.17 The upper plot shows the elastic energy for the steady state solution to the linear viscoelastic model perturbed in the direction of $\mathbf{e}_3^v$. We repeat the calculation for three mesh sizes. The discrepancy between the finer meshes is barely visible on the plot. The lower plot shows the error when halving the time step for the finest mesh. 57
5.18 We plot the elastic energy for the steady state solution to the elastic model perturbed in the direction of $\mathbf{e}_3^v$. Unlike the viscoelastic case, the elastic energy does not increase. 58
5.19 The top plot shows the radial displacement on the edge of the tire for the expanding initial state for the two viscoelasticity models. The bottom plot shows the error between the models. The error between the models is several orders of magnitude smaller than the displacement so that only a single plot can be seen in the top panel. 59
5.20 The top plot shows the vertical displacements of the rightmost edge of the tire for the twisting initial state. The bottom plot shows the error between the models. The error between the models is several orders of magnitude smaller than the displacement so that only a single plot can be seen in the top panel. 59
5.21 Plot of the elastic energy for the same initial condition as in Fig. 5.17, but using the nonlinear model of viscoelasticity. Unlike the linear viscoelastic model case, the elastic energy does not increase, on average. 60
5.22 Plot of the real and imaginary components of the eigenvalues corresponding to the ω_i^v using the nonlinear viscoelastic model. The leftmost X corresponds to ω_{12}^v while the rightmost X corresponds to ω_3^v. The real part of the eigenvalues is negative, bounded well away from zero, and sloping downward. 61
5.23 Rescaled version of the lower plot of 5.22, which shows the slope of the real part of the eigenvalues. 61

Acknowledgments

Firstly, my deep gratitude goes to my advisor and friend Jon Wilkening, who is ever supportive, cheerful, encouraging, and through whom all of this work is possible. His excitement for mathematics is contagious and I've enjoyed our many discussions, whether on topic or not.

I owe special thanks to Sanjay Govindjee, whose helpful insights and perspective on tire mechanics and viscoelasticity has allowed my research to go farther than I hoped.

I've benefited greatly from the enthusiastic teaching and advice of Ole Hald, as well as the courses of Per-Olof Persson, G.I. Barenblatt, Alexandre Chorin, Jim Demmel, and Ming Gu. Chris Rycroft has saved me countless hours of frustration with his patient help compiling and configuring software.

The mathematics group at the Lawrence Berkeley National Laboratory is an amazing place to bounce ideas around with brilliant scientists, run massively parallel jobs, and distract oneself with a game of Tipp-Kick. Thanks to Paul Concus, Barbara Salisbury, and Valerie Heatlie for holding things together and thanks to fellow students and postdocs Matti Morzfeld, August Johansson, Ethan Atkins, Marcus Roper, Ben Stamm, Erica Isaacson, Robert Saye, Jeff Donatelli, Michaeel Kazi, Jakub Kominiarczuk, Brad Froehle, Ben Preskill, and Jue Chen. Finally, much gratitude to Jamie Sethian for his dedicated leadership and encouragement.

I've had the great luck of having wonderful colleagues throughout my time in Berkeley. Special thanks to my officemates and great friends Alan Wilder and José Alameida for many balcony parties, marker throwing games, and chalkboard technique lessons. Thanks to Jeff Doker for introducing me to Scotch tasting, Baobab, and t-shirt design. It was great tossing frisbee in Memorial Glade with you guys, and the rest of the IM team: Ivan Ventura, Morgan Brown, Cynthia Vinzant, Dustin Cartwright, Aaron Kleinman, Mark Howison, Mike Hartglass, Dan Berwick, Rob Bayer, Aaron Mazel-Gee, James Tener, Ian Herbert and more. I would also like to thank Julie Wu for culinary adventures and helpful advice; and Kevin Lin for always being willing to grab a drink. Finally, I'd like to thank Diogo Oliveira e Silva for our discussions on topics of all kinds, exceptional hospitality, and zest for life.

Outside of grad school, I've been supported by many friends, old and new. Many thanks to Peter Hughes for always welcoming me back to Minnesota, Anders Peterson for skiing lessons, Scott Fitzloff for surfing lessons, Andy Bowles for pool lessons, Michelle Peterson for Catan lessons, Julie Van Scoy for used clothes, and Jill Melaas for kayaking to Turtle River Lake with me. I am grateful to Lisa Stewart, Elizabeth DuVal, Yael Almog, and Vito Evola for sharing the Chez Walnut experience with me. Thanks to my current housemates and friends Stephan Adams and Perri Al-Rahim, who kindly helped proof this document.

To my family: you are my greatest blessing. Thank you all; to Douglas for your love of learning and late night chats, to Leland and Leah for your kindness and sense of justice in the world, to Eleva for your loyalty and passion for the environment. To Mom and Dad: I truly could not have even begun, much less finished, this journey without your constant love and belief. I love you all dearly.

Chapter 1

Introduction

The design and modeling of rolling tires is an industrially and socially important engineering problem. Every year in the US, approximately 300 to 375 million tires are replaced [5]. Many of these replacements are due to a complex fracture process [25, 13], for which we would like a methodology to compute the internal strains of the tire. To do this, one must solve the nonlinear equations of elasticity and for more accuracy, incorporate viscoelastic effects. Due to the complex geometry involved, the finite element method is preferred. The problem is often formulated using a change of variables that allows a time-independent computation of the steady state stresses of the rolling tire [22, 4, 24, 26, 19, 12, 20, 27, 14]. This problem is well studied, but the literature only addresses tires with tread patterns that are invariant with the respect to rotation of the tire, while in practice, tread patterns are more complex.

1.1 Treaded tires and time periodic solutions

For a treaded tire, the change of variables commonly used to solve the steady state problem is no longer possible. That choice of change of variables relies on the radial symmetry of the reference configuration which is destroyed by the addition of treads. While most tires exhibit tread patterns that are not invariant with respect to the rotation of the tire, we exploit the fact that tread patterns are typically periodic with respect to the rotation of the tire. That is, if one rotates the tire by some angle θ, the treads will line up with their original position. The upshot is that although we cannot search for steady state solutions of the treaded tire problem, we are able to search for time periodic solutions. Time periodic solutions of PDE have been studied by Wilkening and Ambrose [2, 1], and we follow their method of defining a nonlinear functional of the initial conditions which measures the error between the initial condition and the solution to the PDE evaluted at a later time T, the proposed period. Minimizing this functional allows us to find time periodic solutions of treaded tires and investigate the stresses occuring at different regions of the treads. We also propose a Newton-Krylov method to solve a system of equations that solves the time periodic problem.

1.2 Bifurcations from steady state solutions

When searching for a steady state solution to a free-spinning tire, we expect to find a radially symmetric solution. However, Oden and Lin [24] discovered that for tire speeds higher than a certain critical value ω_c, there exist many more solutions that bifurcate from the radially symmetric solution. They posited that there is a hierarchy of solutions with N peaks and that as we approach the speed ω_c from above, we find N-peak solutions where N is monotonically increasing toward infinity. We show that there are solutions outside of this hierarchy, which appear to be N-peak solutions, but display more radial complexity. Our results suggest there is an entire two-dimensional hierarchy of N-peak solutions that includes the hiearchy of Oden and Lin.

Oden and Lin discovered these bifurcations by linearizing the steady state equations about the radially symmetric solution and observing when the corresponding Jacobian matrix becomes singular. The null-space of the Jacobian indicates bifurcation directions toward N-peak solutions. In contrast, we track eigenvectors of the Jacobian matrix corresponding to bifurcations toward N-peak solutions and observe when their corresponding eigenvalues become zero. This is particularly useful when viscoelasticity is added, for which we used the viscoelastic model of Govindjee and Simo [15]. In that case, we discover the Jacobian matrix never becomes singular and hence no bifurcations are found. However, the eigenvectors corresponding to the N-peak solutions still persist, but their corresponding eigenvalues never become zero due to a real component. We expect that the real component of these eigenvectors is negative due the damping effect of viscoelasticity. This is indeed the case for low tire speeds, but we observe that the real component of the eigenvectors corresonding to the N-peak solutions increases as the tire speed increases, and eventually becomes positive for a fast enough tire speed. This surpising result led us to reconsider our viscoelastic model.

1.3 A comparison of viscoelastic models for the spinning tire

Following the discovery of eigenvalues with positive real part for the free spinning viscoelastic model, we evolve the tire for various initial conditions at the tire speed corresponding to the positive real part eigenvalues. We observe that for every initial condition we try, the elastic energy of the tire increases exponentially. In contrast, with no viscoelasticity, the elastic energy of the system remains bounded for all time. Thus at high tire speeds, the viscoelastic model described in [15] displays nonphysical behavior.

This viscoelastic model is based on a model of Simo [31] which is found in many finite element codes. Similar approaches were used in [17, 18]. However, in [28] Govindjee and Reese noted that the model of Simo has not been proven to satisfy the 2nd Law of Thermodynamics and the linearity of the model restricts its validity to strain states near elastic equilibrium. This is consistent with our observations, since at higher speeds the tire moves farther from elastic equilibrium. To address these issues Govindjee and Reese proposed a

new viscoelastic model in [29] for which the 2nd Law of Thermodynamics can be proven. We repeat our computations with this model and observe none of the elastic energy growth we observed with the model of Govindjee and Simo. This provides evidence that the viscoelastic model of Govindjee and Reese [29] is appropriate for modeling viscoelastic effects in materials far from elastic equilibrium.

1.4 Layout of the present work

We begin the present work by describing the equations of elasticity and our viscoelastic model in chapter 2. The tire is modeled as a compressible Mooney-Rivlin material. The stored energy function $\mathbf{\Psi}$ depends on the three invariants of the Cauchy-Green deformation tensor. Rubber is often modeled as an incompressible material, but instead we model it as compressible with a bulk modulus several orders of magnitude larger than the shear modulus. We incorporate viscoelasticity into our model following the work of Govindjee and Simo [15]. This entails adding independent variables to our model that represent the viscoelastic effects and couple to our original equations of elasticity. Our model system is a two-dimensional annulus and we use plane strain to reduce the three-dimensional equations. The choices of compressible versus incompressible, two-dimensional versus three-dimensional, and plane strain versus plane stress are made in order to make the problem more computationally tractable. Periodic treads on the tire are described by a sinusoidal perturbation of the outer edge of the tire for which we can vary the amplitude and frequency of the treads (See Fig. 2.1). The addition of a road is modeled by a strong traction force that is applied if the tire boundary penetrates beneath the surface of the road. Finally, in chapter 2 we also describe the weak form of the equations and their linearization. These allow us to apply the finite element method as well as compute derivatives needed for numerical minimization and root-finding algorithms.

We turn to the formulation of a time periodic solution to the tire problem in chapter 3, as well as our formulation of the steady state problem. Many previous works [22, 4, 24, 26, 19, 12, 20, 27, 14] use a change of variables $\widetilde{X} = \mathbf{R}(t)X$, where $\mathbf{R}(t)$ is the rotation matrix describing the rotation of the tire up to time t. The equations of motion are then reformulated with this change of variables, and the steady state solution to the spinning tire becomes a static problem, i.e. the transformed motion of the tire under this change of variables, $\widetilde{\boldsymbol{\phi}}$, satisfies $\widetilde{\boldsymbol{\phi}}(\widetilde{X}, t) = \widetilde{\boldsymbol{\phi}}(\widetilde{X}, 0)$ for all time. The formulation of a time periodic solution is similar: $\widetilde{\boldsymbol{\phi}}(\widetilde{X}, T) = \widetilde{\boldsymbol{\phi}}(\widetilde{X}, 0)$, where T is the period. However, we cannot use this change of variables with the treaded tire, since $\mathbf{R}(t)X$ only maps back onto the reference domain for discrete values of t, and hence the reformulated evolution equations are not defined. Instead, we consider the untransformed motion, $\boldsymbol{\phi}$, and define a time periodic solution to satisfy $\boldsymbol{\phi}(\mathbf{R}^{\mathsf{T}}(T)X, T) = \boldsymbol{\phi}(X, 0)$. We also show that the viscoelastic stress tensor $\mathbf{Q}$, an independent variable in the viscoelastic model, must satisfy $\mathbf{R}\mathbf{Q}(\mathbf{R}^{\mathsf{T}}(T)X, T)\mathbf{R}^{\mathsf{T}} = \mathbf{Q}(X, 0)$. However, we do use the change of variables $\widetilde{X} = \mathbf{R}(t)X$ to describe our approach to solving

the steady state problem. This is particularly useful because it is easy to show that the transformed motion $\widetilde{\boldsymbol{\phi}}$ is Hamiltonian in the absence of viscoelasticity.

Chapter 4 describes the numerical methods we employ. The finite element method is our core numerical tool to describe the rolling tire and its evolution. We use non-isoparametric, isogeometric quartic elements. An 8th order Runge-Kutta method is used to evolve the motion of the tire. When computing time periodic solutions, we evolve an initial condition $\boldsymbol{\phi}(X, 0)$ until time T to obtain $\boldsymbol{\phi}(X, T)$. We would like to compare $\boldsymbol{\phi}(\mathbf{R}^{\mathsf{T}}(T)X, T)$ to the initial condition $\boldsymbol{\phi}(X, 0)$. However, because $\boldsymbol{\phi}(\mathbf{R}^{\mathsf{T}}(T)X, T)$ may not align with our finite element mesh, we use a Fourier series representation of the solution to compute $\boldsymbol{\phi}(\mathbf{R}^{\mathsf{T}}(T)X, T)$. To compute time periodic functions we describe two methods. The first is to minimize a nonlinear functional using the Levenberg-Marquardt algorithm which requires dense linear algebra. This second is to solve a system of equations using a Newton-Krylov method, which only requires matrix-vector products. To solve the steady state equations we use Newton's method which requires solving $Ax = b$ for sparse A. When investigating the stability and bifurcations about steady state solutions, we compute eigenvalues of a sparse matrix using ARPACK. Finally, we discuss the use of parallelization in our algorithms.

Our results are discussed in chapter 5. Typical computations of time periodic solutions, steady state solutions, and eigenvalus problems are described, including choices of parameters and computational resources needed. Based on our computation of a time periodic solution for a treaded tire with a road, we investigate the internal stresses at material points in the tire such as in the tread troughs, on the tread crests, or near the hub of the tire. We can plot the evolution of these stresses as the treaded tire makes a full revolution. The time periodic method captures structural frequencies of the material, which we demonstrate by finding a time periodic motion of an oval-like viscoelastic body and comparing its observed oscillations with its structural frequencies as determined by an eigenvalue analysis.

Next, we turn to the eigenvalue analysis of bifurcations from steady state solutions with no road. We linearize our differential operator about radially symmetric steady state solutions and plot the smallest eigenvalues while varying the tire speed. In the elastic case, we observe only imaginary eigenvalues, some of which correspond to the N-peak eigenvectors found by Oden and Lin [24], in addition to more complicated eigenvectors that Oden and Lin did not report. The corresponding eigenvalues pass through 0 and lead to bifurcations from the radially symmetric steady state solution. A spectral decomposition shows that the additional eigenvectors possess more radial complexity than those found by Oden and Lin. When viscoelasticity is added, we observe similar eigenvectors, except their corresponding eigenvalues have non-zero real part and hence do not correspond to bifurcations from the radially symmetric steady state solution. The real parts of these eigenvalues are negative but increase with the tire speed until they become positive.

Finally, we describe the viscoelastic model proposed by Govindjee and Reese [29] and compare it with Govindjee and Simo's model. Evolving the equations of motion demonstrates the the exponential growth of the elastic energy with Govindjee and Simo's model. A mesh refinement study indicates that the exponential growth is not a numerical artifact. In contrast, stability of the elastic energy is observed for the model of Govindjee and Reese

using the same initial conditions. We note that the model of Govindjee and Reese poses no extra numerical difficulties and we repeat some time periodic computations using their model. We also repeat our eigenvalue computations and observe that the real part of the eigenvalues corresponding to the N-peak solutions remains negative, bounded away from zero, and decreasing as the tire speed increases.

Chapter 2

Continuum Mechanics: Viscoelastic Materials

2.1 Kinematics

We present the equations of three-dimensional elasticity, following Marsden and Hughes [23]. Let $\mathcal{B} \subset \mathbb{R}^3$ be a reference configuration for our elastic body. Assume our body undergoes a motion which is described by a function $x = \boldsymbol{\phi}(X, t)$, where $X \in \mathcal{B}$ are material points and $x \in \mathbb{R}^3$ are spatial points. Given a time t, we denote the configuation of $\mathcal{B}$ by $B_t = \boldsymbol{\phi}(\mathcal{B}, t)$. The velocity and acceleration of the motion $\boldsymbol{\phi}$ are given by $\dot{\boldsymbol{\phi}}$ and $\ddot{\boldsymbol{\phi}}$, respectively.

The 3×3 matrix of partial derivatives of $\boldsymbol{\phi}$ is denoted $\mathbf{F} = D\boldsymbol{\phi}$. This matrix is called the deformation gradient and its components are $\mathbf{F}_{ij} = \partial \boldsymbol{\phi}^i / \partial X^j$.

2.2 Balance Laws

Let $\rho(x, t)$ be the mass density of the deformed body at time t and let $\rho_R(X)$ be the mass density in the reference configuration. We assume conservation of mass for any subbody $\mathcal{C} \subset \mathcal{B}$. For this, let $C_t = \boldsymbol{\phi}(\mathcal{C}, t)$ be the configuration of the subbody at time t. Then conservation of mass can be written:

$$\int_{\mathcal{C}} \rho_R(X)\, dX = \int_{C_t} \rho(x, t)\, dx\,. \tag{2.1}$$

Applying the change of variables $x = \boldsymbol{\phi}(X, t)$, we can compute

$$\int_{\mathcal{C}} \rho_R(X)\, dX = \int_{\mathcal{C}} \rho(x, t) J(X, t)\, dX\,, \tag{2.2}$$

where $J = \det(\mathbf{F})$ is the Jacobian of $\boldsymbol{\phi}$. Since (2.1) holds true for any subbody $\mathcal{C}$, $\rho_R = J\rho$. Below, we assume ρ_R is constant.

The body $\mathcal{B}$ experiences forces across any internal surface. We denote $\mathbf{t}(x, t, \mathbf{n})$ the force per unit area across a surface through x with unit normal $\mathbf{n}$ and we call $\mathbf{t}$ the Cauchy traction.

Then balance of momentum for a subbody $\mathcal{C}$ with boundary $\partial\mathcal{C}$ is:

$$\frac{d}{dt}\int_{\mathcal{C}_t} \rho\dot{\boldsymbol{\phi}}\, dx = \int_{\partial\mathcal{C}_t} \mathbf{t}(x, t, \mathbf{n})\, da\,, \tag{2.3}$$

where $\mathbf{n}$ is the unit normal to $\mathcal{C}_t$.

2.3 The Cauchy stress tensor

Cauchy's theorem states that $\mathbf{t}(x, t, \mathbf{n})$ is linear in $\mathbf{n}$. We can write $\mathbf{t}(x, t, \mathbf{n}) = \boldsymbol{\sigma}(x, t)^{\mathsf{T}}\mathbf{n}$, where $\boldsymbol{\sigma}$ is a 3×3 matrix called the Cauchy stress tensor. From balance of angular momentum, it can be proven that $\boldsymbol{\sigma}$ is a symmetric tensor.

In terms of $\boldsymbol{\sigma}$, balance of momentum becomes

$$\frac{d}{dt}\int_{\mathcal{C}_t} \rho\dot{\boldsymbol{\phi}}\, dx = \int_{\partial\mathcal{C}_t} \boldsymbol{\sigma}\mathbf{n}\, da\,. \tag{2.4}$$

2.4 The Reference configuration

For many numerical methods, it is convenient to work on a domain that is not moving in time; hence, we restate balance of momentum in the reference frame. To this end, we define the Piola transform $\mathcal{T}$, which maps a vector field $\mathbf{w}(x, t)$ in the deformed configuration to a vector field $\mathbf{W}(X, t)$ in the reference configuration by $\mathbf{W} = \mathcal{T}(\mathbf{w}) = J\mathbf{F}^{-1}\mathbf{w}(x, t)$. The factor of J is present because it leads to the following nice relationship:

$$\int_{\partial C_t} \mathbf{w}\cdot\mathbf{n}\, da = \int_{\partial\mathcal{C}} \mathbf{W}\cdot\mathbf{N}\, dA\,. \tag{2.5}$$

This can be proved by first showing through direct calculation that $\mathrm{DIV}\, J\mathbf{F}^{-1} = \mathbf{0}$ and using this to verify that $\mathrm{DIV}\,\mathbf{W} = J \operatorname{div} \mathbf{w}$:

$$\begin{aligned}
\mathrm{DIV}\,\mathbf{W} &= \frac{\partial \mathbf{W}^i}{\partial X^i} \\
&= \frac{\partial (J \frac{\partial X^i}{\partial x^j} \mathbf{w}^j)}{\partial X^i} \\
&= \frac{\partial (J \frac{\partial X^i}{\partial x^j})}{\partial X^i} \mathbf{w}^j + J \frac{\partial X^i}{\partial x^j} \frac{\partial \mathbf{w}^j}{\partial X^i} \\
&= 0 + J \frac{\partial X^i}{\partial x^j} \frac{\partial \mathbf{w}^j}{\partial x^k} \frac{\partial x^k}{\partial X^i} \\
&= J \delta^k_j \frac{\partial \mathbf{w}^j}{\partial x^k} \\
&= J \frac{\partial \mathbf{w}^k}{\partial x^k} \\
&= J \operatorname{div} \mathbf{w} \,.
\end{aligned} \tag{2.6}$$

Using the change of variables formula, we can then complete the proof of (2.5):

$$\begin{aligned}
\int_{\partial \mathcal{C}} \mathbf{W} \cdot \mathbf{N} \, dA &= \int_{\mathcal{C}} \mathrm{DIV}\,\mathbf{W} \, dX \\
&= \int_{\mathcal{C}} J \operatorname{div} \mathbf{w} \, dX \\
&= \int_{C_t} \operatorname{div} \mathbf{w} \, dx \\
&= \int_{\partial C_t} \mathbf{w} \cdot \mathbf{n} \, da \,.
\end{aligned} \tag{2.7}$$

Similarly, for a tensor $\mathbf{a}$ and its Piola transform $\mathbf{A}$ we have

$$\int_{\partial C_t} \mathbf{a}\mathbf{n} \, da = \int_{\partial \mathcal{C}} \mathbf{A}\mathbf{N} \, dA \,, \tag{2.8}$$

where the Piola transform for a tensor is defined as $\mathbf{A} = \mathcal{T}(\mathbf{a}) = J\mathbf{a}\mathbf{F}^{-T}$.

Using (2.5) and change of variables, we can restate balance of momententum (2.4) in the reference configuration:

$$\frac{d}{dt} \int_{\mathcal{C}} \rho_R \dot{\boldsymbol{\phi}} \, dX = \int_{\partial \mathcal{C}} J \boldsymbol{\sigma} \mathbf{F}^{-T} \mathbf{N} \, dA \,. \tag{2.9}$$

We define the first Piola-Kirkhhoff stress tensor to be the Piola Transform of $\boldsymbol{\sigma}$, that is $\mathbf{P} = \mathcal{T}(\boldsymbol{\sigma}) = J\boldsymbol{\sigma}\mathbf{F}^{-T}$. Then balance of momentum becomes

$$\frac{d}{dt} \int_{\mathcal{C}} \rho_R \dot{\boldsymbol{\phi}} \, dX = \int_{\partial \mathcal{C}} \mathbf{P}\mathbf{N} \, dA \,, \tag{2.10}$$

with pointwise form

$$\rho_R \ddot{\boldsymbol{\phi}} = \mathrm{DIV}\,\mathbf{P} \,. \tag{2.11}$$

2.5 Constitutive relations

We may solve (2.11) given a way to compute $\mathbf{P}$ based on the motion $\boldsymbol{\phi}$. A material is called Cauchy elastic if $\mathbf{P}$ can be written as a function of X and the deformation gradient $\mathbf{F}$. We consider a subclass of Cauchy elastic materials called hyperelastic (or Green elastic) materials for which there exists an elastic stored energy function $\boldsymbol{\Psi}(X, \mathbf{F})$ such that $\mathbf{P}(X, \mathbf{F}) = \partial\boldsymbol{\Psi}/\partial\mathbf{F}$. In coordinates, $\mathbf{P}(X, \mathbf{F})_{ij} = (\partial\boldsymbol{\Psi}/\partial\mathbf{F}_{ij})$. We can justify that $\boldsymbol{\Psi}$ is an energy function by defining the total energy to be

$$\mathcal{E}(X, \mathbf{F}, \dot{\boldsymbol{\phi}}) = \int_{\mathcal{B}} \left[\frac{\rho_R}{2}\dot{\boldsymbol{\phi}} \cdot \dot{\boldsymbol{\phi}} + \boldsymbol{\Psi}(X, \mathbf{F})\right] dX \tag{2.12}$$

and showing that $\mathcal{E}$ is constant in time. Assume either free boundary conditions or dirichlet boundary conditions:

$$\begin{aligned} \mathbf{PN} &= \mathbf{0} \text{ on } \partial\mathcal{B} \qquad &&\text{(free boundary)} \\ \boldsymbol{\phi} = \dot{\boldsymbol{\phi}} &= \mathbf{0} \text{ on } \partial\mathcal{B} \qquad &&\text{(dirichlet boundary)}\,, \end{aligned} \tag{2.13}$$

where $\mathbf{N}$ is the outward unit normal of $\partial\mathcal{B}$. We discuss boundary conditions for the tire in §2.9 below. We can now compute $\frac{d}{dt}\mathcal{E} = 0$ using our definitions above and integration by parts:

$$\begin{aligned} \frac{d}{dt}\mathcal{E} &= \frac{d}{dt}\int_{\mathcal{B}} \frac{\rho_R}{2}\dot{\boldsymbol{\phi}} \cdot \dot{\boldsymbol{\phi}} + \boldsymbol{\Psi}(X, \mathbf{F}) \\ &= \int_{\mathcal{B}} \rho_R \ddot{\boldsymbol{\phi}} \cdot \dot{\boldsymbol{\phi}} + \frac{\partial\boldsymbol{\Psi}}{\partial\mathbf{F}} : \frac{d}{dt}\mathbf{F} \\ &= \int_{\mathcal{B}} \rho_R \ddot{\boldsymbol{\phi}} \cdot \dot{\boldsymbol{\phi}} + \mathbf{P} : D\dot{\boldsymbol{\phi}} \\ &= \int_{\mathcal{B}} \rho_R \ddot{\boldsymbol{\phi}} \cdot \dot{\boldsymbol{\phi}} - \int_{\mathcal{B}} \operatorname{DIV}\mathbf{P} \cdot \dot{\boldsymbol{\phi}} + \int_{\partial\mathcal{B}} \mathbf{PN} \cdot \dot{\boldsymbol{\phi}} \\ &= \int_{\mathcal{B}} \left(\rho_R \ddot{\boldsymbol{\phi}} - \operatorname{DIV}\mathbf{P}\right) \cdot \dot{\boldsymbol{\phi}} + 0 \\ &= 0\,. \end{aligned} \tag{2.14}$$

Several assumptions about the elastic material reduce the possible energy functions $\boldsymbol{\Psi}$. Firstly, we assume the material is homogenous, so that $\boldsymbol{\Psi}$ and hence $\mathbf{P}$ do not depend explicitly on X. Second, we assume material frame indifference, i.e. a rigid rotation of the material should not change its elastic properties. This can be expressed as

$$\mathbf{P}(\mathbf{VF}) = \mathbf{VP}(\mathbf{F}) \text{ for all } \mathbf{V}\,, \tag{2.15}$$

where $\mathbf{V}$ is a proper rotation matrix, i.e. $\mathbf{V}$ is orthogonal and $\det\mathbf{V} = 1$. This implies $\boldsymbol{\Psi}(\mathbf{VF}) = \boldsymbol{\Psi}(\mathbf{F})$.

Apply the polar decomposition of matrices to $\mathbf{F}$ and write $\mathbf{F} = \mathbf{T}\mathbf{U}$, where $\mathbf{T}$ is a rotation matrix and $\mathbf{U} = \sqrt{\mathbf{F}^\top\mathbf{F}}$. We have that $\boldsymbol{\Psi}(\mathbf{F}) = \boldsymbol{\Psi}(\mathbf{U})$ and hence $\boldsymbol{\Psi}$ only depends on $\mathbf{F}$ through $\mathbf{C} \stackrel{\text{def}}{=} \mathbf{F}^\top\mathbf{F}$. $\mathbf{C}$ is known as the right Cauchy-Green deformation tensor.

Thirdly, we assume our material has no preferred directions, or is isotropic. This is expressed via $\mathbf{P}(\mathbf{F}\mathbf{V}) = \mathbf{P}(\mathbf{F})$ for all $\mathbf{V}$. Similar to frame indifference, we have $\boldsymbol{\Psi}(\mathbf{F}\mathbf{V}) = \boldsymbol{\Psi}(\mathbf{F})$.

Assuming frame indifference, homogeneity, and isotropy, we can restrict the form of $\boldsymbol{\Psi}$. The polar decomposition and eigenvalue decomposition for symmetric matrices implies $\mathbf{F} = \mathbf{T}\sqrt{\mathbf{C}} = \mathbf{T}\mathbf{V}\boldsymbol{\Lambda}\mathbf{V}^\top$. $\mathbf{T}, \mathbf{V}$ are rotation matrices and $\boldsymbol{\Lambda}$ is a diagonal matrix with entires $\lambda_i = \sqrt{\nu_i}$, where the ν_i are the eigenvalues of $\mathbf{C}$. Applying frame indifference and isotropy, $\boldsymbol{\Psi}(\mathbf{F}) = \boldsymbol{\Psi}(\boldsymbol{\Lambda})$. Hence, $\boldsymbol{\Psi}$ is a function of the eigenvalues ν_i of C and furthermore $\boldsymbol{\Psi}$ is symmetric in the ν_i since the eigenvalues can appear in any order. $\boldsymbol{\Psi}$ can also be considered as a function of the invariants I_1, I_2, I_3 of $\mathbf{C}$. We recall that the invariants of $\mathbf{C}$ are given by

$$\begin{aligned} I_1 &= \operatorname{tr}\mathbf{C} = \nu_1 + \nu_2 + \nu_3\,, \\ I_2 &= \det\mathbf{C}\operatorname{tr}\mathbf{C}^{-1} = \frac{1}{2}[(\operatorname{tr}\mathbf{C})^2 - \operatorname{tr}\mathbf{C}^2] = \nu_1\nu_2 + \nu_1\nu_3 + \nu_2\nu_3\,, \\ I_3 &= \det\mathbf{C} = \nu_1\nu_2\nu_3\,. \end{aligned} \tag{2.16}$$

The invariants of $\mathbf{C}$ are also the coefficients of the characteristic polynomial of $\mathbf{C}$, so they completely determine the eigenvalues ν_i and vice-versa.

Since $\boldsymbol{\Psi}$ depends on $\mathbf{F}$ through $\mathbf{C}$, using the chain rule, we can write

$$\mathbf{P} = \frac{\partial\boldsymbol{\Psi}}{\partial\mathbf{F}} = \frac{\partial\boldsymbol{\Psi}}{\partial\mathbf{C}}\frac{\partial\mathbf{C}}{\partial\mathbf{F}} = 2\mathbf{F}\frac{\partial\boldsymbol{\Psi}}{\partial\mathbf{C}}\,. \tag{2.17}$$

The tensor $\mathbf{S} = 2\frac{\partial\boldsymbol{\Psi}}{\partial\mathbf{C}}$ is called the second Piola-Kirkhhoff stress tensor. It is symmetric, since $\boldsymbol{\sigma}$ is symmetric and $\mathbf{S} = \mathbf{F}^{-1}\mathbf{P} = \mathbf{F}^{-1}J\boldsymbol{\sigma}\mathbf{F}^{-T}$.

2.6 The stored energy function

We choose the stored energy function $\boldsymbol{\Psi}(I_1, I_2, I_3)$ to be

$$\boldsymbol{\Psi} = \frac{\kappa}{4}\left(I_3 - \log I_3 - 1\right) + \frac{\mu}{2}(1-s)\left(I_1 - \log I_3 - 3\right) + \frac{\mu}{2}s\left(I_2 - 2\log I_3 - 3\right)\,. \tag{2.18}$$

The first term penalizes for volume change. The constant κ is known as the bulk modulus and measures the material's resistance to compression and expansion. $\frac{\kappa}{4}\left(I_3 - \log I_3 - 1\right)$ goes to infinity as either I_3 goes to zero or infinity. The second and third terms account for shear stresses. They are chosen to be linear in I_1 and I_2 for simplicity. μ measures the material's resistance to shear and is known as the shear modulus. $s \in [0, 1]$ can be chosen to balance the two shear terms. The constants $1, 3$ and 3 in each of the three terms are chosen so that when $\mathbf{C}$ is the identity, each term of the energy is 0. The coefficients of $\log I_3$ in the

second and third terms are chosen so that $\mathbf{P}(\mathbf{I}) = \mathbf{0}$, where $\mathbf{I}$ is the identity matrix. This ensures that there are no stresses in the undeformed state.

Our stored energy function also satisfies requirements described in [3] and [30] to prove that minimizers of our stored energy function exist. Namely, it can be shown that if $s \in (0,1)$, $\mathbf{\Psi}$ is polyconvex, as defined in Ball [3], and $\mathbf{\Psi}$ satisfies the growth conditions of Müller, Qi, and Yan [30]:

$$\begin{aligned} \mathbf{\Psi} &\to \infty \text{ as } I_3 \to 0^+ \,, \\ \mathbf{\Psi}(I_1, I_2, I_3) &\geq c_1(I_1 + I_2^{\frac{3}{4}}) - c_0 \,, \quad c_1 > 0 \,. \end{aligned} \tag{2.19}$$

Given mixed traction-displacement boundary conditions, it is proved in [30] that there exist minimizers to our stored energy function in an appropriate Sobelev space. In this work, we are concerned with initial value evolution problems with more complicated boundary conditions, where the existence theorems of Ball [3] and Müller, Qi, and Yan [30] do not apply. However, those results suggest that our stored energy function is a sensible choice.

We compute the first Piola-Kirkhhoff stress tensor $\mathbf{P}(\mathbf{F}) = \partial\mathbf{\Psi}/\partial\mathbf{F}$. First, we compute $\partial I_i/\partial\mathbf{C}$:

$$\frac{\partial I_1}{\partial \mathbf{C}} = \mathbf{I} \,, \qquad \frac{\partial I_2}{\partial \mathbf{C}} = I_1\mathbf{I} - \mathbf{C} \,, \qquad \frac{\partial I_3}{\partial \mathbf{C}} = I_3\mathbf{C}^{-1} \,. \tag{2.20}$$

We then have:

$$\begin{aligned} \frac{\partial \mathbf{\Psi}}{\partial \mathbf{C}} &= \frac{\kappa}{4}(I_3 - 1)\mathbf{C}^{-1} + \frac{\mu}{2}(1-s)(\mathbf{I} - \mathbf{C}^{-1}) + \frac{\mu}{2}s(I_1\mathbf{I} - \mathbf{C} - 2\mathbf{C}^{-1}) \\ \mathbf{P} &= \frac{\partial \mathbf{\Psi}}{\partial \mathbf{F}} = 2\mathbf{F}\frac{\partial \mathbf{\Psi}}{\partial \mathbf{C}} \\ &= \frac{\kappa}{2}(I_3 - 1)\mathbf{F}^{-T} + \mu(1-s)(\mathbf{F} - \mathbf{F}^{-T}) + \mu s(I_1\mathbf{F} - \mathbf{F}\mathbf{C} - 2\mathbf{F}^{-T}) \,. \end{aligned} \tag{2.21}$$

2.7 Viscoelastic model

We introduce viscoelasticity to our model, i.e. we add some mechanism by which stresses that a material point experiences at time t_1 will still have an effect at a later time t_2. This gives us a new constitutive model $\mathbf{P}_{total} = \mathbf{P}_e + \mathbf{P}_v$, where $\mathbf{P}_v$ accounts for stresses arising from viscoelasticity and $\mathbf{P}_e$ is the purely elastic consititive function described above.

Given the viscoelastic stress tensor $\mathbf{P}_v$, below we will adopt a new notation to account for the viscoelastic stresses. $\mathbf{P}_e$ and $\mathbf{S}_e$ will refer to the purely elastic stress tensors already described and $\mathbf{\Psi}_e$ will refer to the elastic stored energy function described above. $\mathbf{P} = \mathbf{P}_e + \mathbf{P}_v$ will refer to the total first Piola-Kirkhhoff stress tensor while $\mathbf{S} = \mathbf{S}_e + \mathbf{S}_v$ will refer to the total second Piola-Kirkhhoff stress tensor, with $\mathbf{S}_v \stackrel{\text{def}}{=} \mathbf{F}^{-1}\mathbf{P}_v$.

Our mechanism of viscoelasticity follows the model of Govindjee and Simo [15]. We introduce the viscoelastic stress tensor

$$\mathbf{Q}(t) = \int_{-\infty}^{t} \exp\left(\frac{-(t-s)}{\tau}\right) \dot{\mathbf{S}}_e(s)\, ds \,. \tag{2.22}$$

By differentiating (2.22), we find that $\mathbf{Q}$ solves the differential equation

$$\dot{\mathbf{Q}}(t) = -\frac{1}{\tau}\mathbf{Q}(t) + \dot{\mathbf{S}}_e(t)\,. \tag{2.23}$$

If the weighting $\exp\left(-(t-s)/\tau\right)$ was not present, $\mathbf{Q}(t) = \mathbf{S}_e(t)$. From the differential equation (2.23), we see that $\mathbf{Q}(t)$ is driven by the term $\dot{\mathbf{S}}_e$ to evolve as $\mathbf{S}_e$, with the weighting contributing the damping term $-\frac{1}{\tau}\mathbf{Q}(t)$. The parameter τ indicates how quickly the weight goes to zero as one looks further back in time and how quickly changes in $\mathbf{S}_e$ are damped out. τ is called the relaxation time because it gives the timescale over which the material relaxes, i.e. the timescale over which deformations away from equilibrium are damped out.

We incorporate $\mathbf{Q}$ into our model by setting $\mathbf{S}_v$ equal to $\mathbf{Q}$, weighted by a paramter ν:

$$\mathbf{S}_v(t) = \nu\mathbf{Q}(t)\,. \tag{2.24}$$

This implies that $\mathbf{P}_v$ is given by

$$\mathbf{P}_v = \mathbf{F}\mathbf{S}_v\,, \tag{2.25}$$

which gives us the constitutive equation for viscoelasticity. Our new equations of motion are given by

$$\rho_R\ddot{\boldsymbol{\phi}} = \mathrm{DIV}\,\mathbf{P} = \mathrm{DIV}[\mathbf{P}_e + \nu\mathbf{F}\mathbf{Q}]\,. \tag{2.26}$$

When evolving $\mathbf{Q}$, we use the differential equation form (2.23) so that values of $\dot{\mathbf{S}}_e$ from past times do not need to be stored. According to the integral equation (2.22), in order to define $\mathbf{Q}$, the motion $\boldsymbol{\phi}$ must be known for all previous times. To solve an initial value problem beginning at $t = 0$, we specify an initial value $\mathbf{Q}_0 = \mathbf{Q}(X, 0)$, which is equivalent to assuming that

$$\int_{-\infty}^{0} \exp\left(\frac{-(t-s)}{\tau}\right)\dot{\mathbf{S}}_e(s)\,ds = \mathbf{Q}_0\,. \tag{2.27}$$

In order to evolve $\mathbf{Q}$ using the differential equation (2.23), we need to compute the time derivative $\dot{\mathbf{S}}_e$. This can be expressed in terms of the deformation gradient $\mathbf{F}$ and the gradient of the velocity $\dot{\mathbf{F}} = D\dot{\boldsymbol{\phi}}$. We compute:

$$\begin{aligned}
\dot{\mathbf{C}} &= \dot{\mathbf{F}}^{\mathsf{T}}\mathbf{F} + \mathbf{F}^{\mathsf{T}}\dot{\mathbf{F}} \\
\dot{\det\mathbf{C}} &= \det\mathbf{C}\,\mathrm{tr}(\mathbf{C}^{-1}\dot{\mathbf{C}}) \\
\dot{\mathbf{C}^{-1}} &= -\mathbf{C}^{-1}\dot{\mathbf{C}}\mathbf{C}^{-1} \\
\dot{\mathbf{S}}_e &= \frac{\kappa}{2}\left[(\dot{\det\mathbf{C}})\mathbf{C}^{-1} + (\det\mathbf{C} - 1)\dot{\mathbf{C}^{-1}}\right] \\
&\quad + \mu(1-s)\left(-\dot{\mathbf{C}^{-1}}\right) + \mu s\left((\mathrm{tr}\,\dot{\mathbf{C}})\mathbf{I} - \dot{\mathbf{C}} - 2\dot{\mathbf{C}^{-1}}\right)\,.
\end{aligned} \tag{2.28}$$

We note that the model of Govindjee and Simo [15] assumes that only viscous shear stresses are important and uses the deviatoric operator DEV to define $\mathbf{Q}$ and $\mathbf{S}_v$:

$$\begin{aligned} \mathrm{DEV}(t)\mathbf{A} &\stackrel{\text{def}}{=} \mathbf{A} - \frac{1}{3}\,\mathrm{tr}(\mathbf{A}\mathbf{C}(t))\mathbf{C}(t)^{-1} \\ \mathbf{Q}(t) &= \int_{-\infty}^{t} \exp\left(\frac{-(t-s)}{\tau}\right) \frac{d}{ds}\left(\mathrm{DEV}(s)\mathbf{S}_e(s)\right)\, ds \\ \mathbf{S}_v(t) &= \nu\,\mathrm{DEV}(t)\mathbf{Q}(t)\,. \end{aligned} \tag{2.29}$$

For simplicity, we do not include the DEV operator into our model, but note that doing so is feasible.

2.8 Two-dimensional formulation

We reduce the full three-dimensional equations in euclidean coordinates $X = (X^1, X^2, X^3)$ to equations only involving $\breve{X} = (X^1, X^2)$. Two common ways to perform this reduction are known as plane stress and plane strain. We adopt plane strain, whereby we assume there is no component of strain in the X_3 direction. Thus the motion $\boldsymbol{\phi}$ is of the form

$$\boldsymbol{\phi}(X^1, X^2, X^3, t) = (\boldsymbol{\phi}^1(X^1, X^2), \boldsymbol{\phi}^2(X^1, X^2), X^3, t) = (\breve{\boldsymbol{\phi}}(\breve{X}, t), X^3)\,. \tag{2.30}$$

$\mathbf{F}$ is of the form $\begin{bmatrix} * & * & 0 \\ * & * & 0 \\ 0 & 0 & 1 \end{bmatrix} = \begin{bmatrix} \breve{\mathbf{F}} & \mathbf{0} \\ \mathbf{0} & 1 \end{bmatrix}$, where $\breve{\mathbf{F}}$ is a 2×2 matrix. Subsequently, if $\mathbf{A}$ is a 3×3 matrix, $\breve{\mathbf{A}}$ is defined to be its upper 2×2 minor. Similarly, $\mathbf{C}$ is of the form $\begin{bmatrix} \breve{\mathbf{C}} & \mathbf{0} \\ \mathbf{0} & 1 \end{bmatrix}$. We can compute that $\mathbf{S}_e = 2\partial\boldsymbol{\Psi}_e/\partial\mathbf{C}$ is of the form $\begin{bmatrix} \breve{\mathbf{S}}_e & \mathbf{0} \\ \mathbf{0} & \zeta_{\mathbf{S}} \end{bmatrix}$, where $\zeta_{\mathbf{S}}$ is a function only of X^1 and X^2. From the definition of $\mathbf{Q}$ in (2.22), $\mathbf{Q}$ and hence $\mathbf{S}_v$ also have the same form as $\mathbf{S}_e$. Finally, this implies that $\mathbf{P} = \mathbf{F}(\mathbf{S}_e + \mathbf{S}_v)$ has the form $\begin{bmatrix} \breve{\mathbf{P}} & \mathbf{0} \\ \mathbf{0} & \zeta_{\mathbf{P}} \end{bmatrix}$, where $\zeta_{\mathbf{P}}$ is a function only of X^1 and X^2. From the equations of motion

$$\rho_R\ddot{\boldsymbol{\phi}} = \mathrm{DIV}\,\mathbf{P}\,, \tag{2.31}$$

the third component of $\ddot{\boldsymbol{\phi}}$ is zero due to $\zeta_{\mathbf{P}}$ being a function only of X^1 and X^2. This justifies that solving the problem $\rho_R\ddot{\boldsymbol{\phi}} = \mathrm{DIV}\,\mathbf{P}$ with the constraint

$$\boldsymbol{\phi}(X^1, X^2, X^3, t) = (\breve{\boldsymbol{\phi}}(\breve{X}, t), X_3) \tag{2.32}$$

is equivalent to solving the two-dimensional problem $\rho_R\breve{\boldsymbol{\phi}}_{tt} = \mathrm{DIV}\,\breve{\mathbf{P}}$.

However, instead of computing the 3×3 matrix $\mathbf{P}$ and then extracting it's upper left 2×2 minor $\breve{\mathbf{P}}$, we would like to do all computations with 2×2 matrices. This is easy since the

definitions of $\mathbf{F}, \mathbf{C}, \mathbf{Q}$, etc. above hold true for their counterparts $\breve{\mathbf{F}}, \breve{\mathbf{C}}, \breve{\mathbf{Q}}$ with one exception arising from the fact that given a 3×3 matrix $\mathbf{A}$ of the form $\begin{bmatrix} \breve{\mathbf{A}} & \mathbf{0} \\ \mathbf{0} & 1 \end{bmatrix}$, then $\operatorname{tr}\mathbf{A} = \operatorname{tr}\breve{\mathbf{A}} + 1$. This implies that $\breve{I}_1$ should be defined as $\operatorname{tr}\breve{\mathbf{C}} + 1$ instead of $\operatorname{tr}\breve{\mathbf{C}}$. Using this, we then make the following definitions and redefinitions:

$$\begin{aligned}
\breve{\mathbf{F}} &= D\breve{\boldsymbol{\phi}} \\
\breve{J} &= \det \breve{\mathbf{F}} \\
\breve{\mathbf{C}} &= \breve{\mathbf{F}}^{\mathsf{T}}\breve{\mathbf{F}} \\
\breve{I}_1 &= \operatorname{tr}\breve{\mathbf{C}} + 1 \\
\breve{I}_3 &= \det \breve{\mathbf{C}} \\
\breve{\mathbf{S}}_e &= \frac{\kappa}{2}(\breve{I}_3 - 1)\mathbf{C}^{-1} + \mu(1-s)(\breve{\mathbf{I}} - \breve{\mathbf{C}}^{-1}) + \mu s(\breve{I}_1\breve{\mathbf{I}} - \breve{\mathbf{C}} - 2\breve{\mathbf{C}}^{-1}) \\
\breve{\mathbf{Q}}(t) &= \int_{-\infty}^{t} \exp\left(\frac{-(t-s)}{\tau}\right)\frac{d}{ds}\left(\breve{\mathbf{S}}_e(s)\right)\, dt \\
\breve{\mathbf{S}}_v &= \nu\breve{\mathbf{Q}} \\
\breve{\mathbf{P}} &= \breve{\mathbf{F}}(\breve{\mathbf{S}}_e + \breve{\mathbf{S}}_v)\,.
\end{aligned} \tag{2.33}$$

One can check that these definitions of $\breve{\mathbf{F}}, \breve{\mathbf{S}}_e, \breve{\mathbf{P}}$ etc. agree with the definitions given before as upper 2×2 matrix minors. Hence we can compute $\breve{\mathbf{P}}$ and evolve $\breve{\boldsymbol{\phi}}$ without 3×3 matrix computations. For ease of notation, we will subsequently drop the breve and always refer to the two-dimensional quantities and not their three-dimensional counterparts.

2.9 Domain and Boundary conditions

We model the two-dimensional smooth tire as an annulus about the origin with inner radius r_1 and outer radius r_2. The reference configuration is then given by the set

$$\mathcal{B} = \{(X_1, X_2)\,|\, r_1 \le \|X\|_2 \le r_2\}\ . \tag{2.34}$$

The inner boundary $\Gamma_h = \{X|\ \|X\|_2 = r_1\}$ is called the hub and the outer boundary $\Gamma_e = \{X|\ \|X\|_2 = r_2\}$ is called the edge.

Observe that the smooth tire above can be seen as the image of the set $A = \{(r,\theta)|\, r_1 \le r \le r_2,\ 0 \le \theta < 2\pi\}$ under the polar coordinate map $T(r,\theta) = (r\cos\theta, r\sin\theta)$. To obtain a treaded tire, we can perturb this map:

$$\begin{aligned}
T_{\varepsilon,\beta}(r,\theta) &= \psi(r,\varepsilon,\beta)(\cos\theta, \sin\theta) \\
\psi(r,\varepsilon,\beta) &= r + \varepsilon(r - r_1)\cos(\beta\theta)\,.
\end{aligned} \tag{2.35}$$

We define the reference configuration for the treaded tire to be $\mathcal{B}_{\varepsilon,\beta} = T_{\varepsilon,\beta}(A)$ with hub $\Gamma_h = \{T_{\varepsilon,\beta}(r,\theta)\,|\, r = r_1,\ 0 \le \theta < 2\pi\}$ and edge $\Gamma_e = \{T_{\varepsilon,\beta}(r,\theta)\,|\, r = r_2,\ 0 \le \theta < 2\pi\}$. We

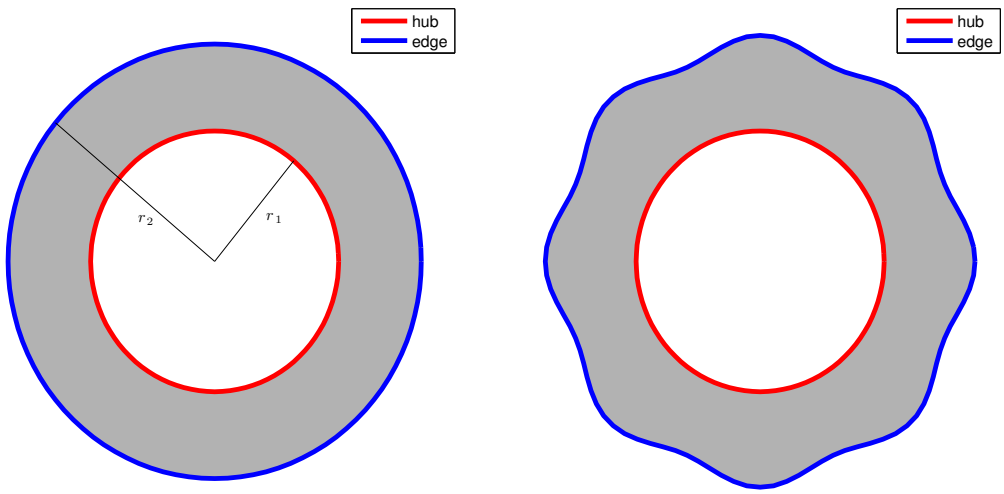

Figure 2.1: The plot on the left shows the smooth tire corresponding to the reference domain $\mathcal{B}$. The plot on the right is a treaded tire corresponding to the reference domain $\mathcal{B}_{.1,8}$.

have chosen $T_{\varepsilon,\beta}$ so that at r_1, $T_{\varepsilon,\beta} = T$; hence the hub is the same for the treaded and smooth tires. However, the edge of the treaded tire is a circle with β bumps, or treads.

We prescribe the boundary conditions for the smooth and treaded tires. The tire is spun at a speed ω along the hub so that

$$\boldsymbol{\phi}(X,t) = \mathbf{R}(t)X \text{ on } \Gamma_h\,, \tag{2.36}$$

where $\mathbf{R}(t)$ is the rotation matrix given by $\begin{bmatrix} \cos(\omega t) & -\sin(\omega t) \\ \sin(\omega t) & \cos(\omega t) \end{bmatrix}$. The time derivative of $\mathbf{R}(t)$, which is needed below, is given by

$$\dot{\mathbf{R}}(t) = \omega \begin{bmatrix} -\sin(\omega t) & -\cos(\omega t) \\ \cos(\omega t) & -\sin(\omega t) \end{bmatrix}\,. \tag{2.37}$$

On the edge, we either have a free surface or the tire is contacting the road. The free surface is described by the absence of stresses in the outward normal direction along the boundary of the reference configuration and given by the formula $\mathbf{PN} = \mathbf{0}$.

Tire contact with the road is modeled by prescribing a force pushing against the edge of the tire if the edge penetrates beneath the surface of the road. More specifically, let $h > r_1$ be the distance from the x^1-axis to the road, so that the road is lying along $x^2 = -h$. If X is a point on the edge and $\boldsymbol{\phi}^2 = \boldsymbol{\phi}^2(X) < -h$, we consider a force of magnitude $\delta\gamma(-h - \boldsymbol{\phi}^2)$ per unit reference area in the x^2 direction, $\mathbf{e}_2$. We apply this force at the point $x = \boldsymbol{\phi}(X)$ in the deformed configuration. In precise terms: at a point X on the edge with outward normal $\mathbf{N}$ of the reference configuration, we have

$$\mathbf{PN} = \delta\gamma(-h - \boldsymbol{\phi}^2)\mathbf{e}_2\,. \tag{2.38}$$

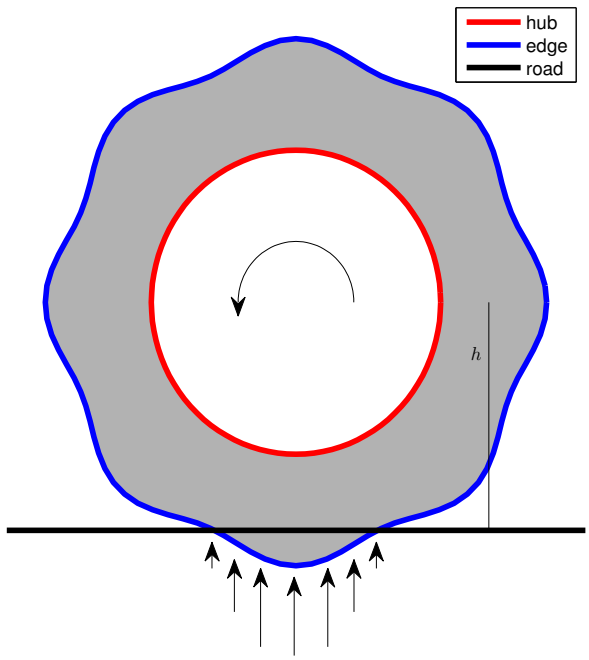

Figure 2.2: The plot above shows the positioning of the road and indicates the traction forces experienced by the edge by vectors pointing upward. The vectors increase in magnitude the deeper the tire penetrates the road. The direction of rotation is also indicated.

We require that $\gamma(0) = 0$ and γ be monotonically increasing. $\delta > 0$ is a parameter we choose to ensure that road is sufficiently strong so that there is little tire penetration into the road.

Both the free boundary condition and the road boundary condition on the edge can be expressed as the single condition

$$\mathbf{PN} = \delta\gamma(-h - \boldsymbol{\phi}^2)\mathbf{e}_2\,, \tag{2.39}$$

if we choose γ such that $\gamma(z) = 0$ for $z \leq 0$. We define

$$\mathbf{h} = \delta\gamma(-h - \boldsymbol{\phi}^2)\mathbf{e}_2\,. \tag{2.40}$$

Thus our boundary conditions are

$$\begin{aligned} \boldsymbol{\phi}(X,t) &= \mathbf{R}(t)X \text{ on } \Gamma_h \\ \mathbf{PN} &= \mathbf{h} \text{ on } \Gamma_e\,. \end{aligned} \tag{2.41}$$

2.10 Weak formulation

Thus far, the partial differential equation we wish to solve is

$$\begin{aligned} \rho_R \ddot{\boldsymbol{\phi}} &= \mathrm{DIV}\,\mathbf{P} \text{ on } \mathcal{B} \\ \dot{\mathbf{Q}} &= -\frac{1}{\tau}\mathbf{Q} + \dot{\mathbf{S}}_e \text{ on } \mathcal{B}\,, \end{aligned} \tag{2.42}$$

with boundary conditions

$$\begin{aligned} \boldsymbol{\phi}(X,t) &= \mathbf{R}(t)X \text{ on } \Gamma_h \\ \mathbf{PN} &= \mathbf{h} \text{ on } \Gamma_e\,. \end{aligned} \tag{2.43}$$

It is useful to reformulate the problem as first order differential equation, since our numerical time stepping algorithms are designed for first order equations. We introduce velocity as an independent variable $\boldsymbol{\nu}$, which must satisfy the boundary condition

$$\boldsymbol{\nu}(X,t) = \dot{\mathbf{R}}(t)X \text{ on } \Gamma_h\,. \tag{2.44}$$

The equations of motion become

$$\begin{aligned} \dot{\boldsymbol{\phi}} &= \boldsymbol{\nu} \text{ on } \mathcal{B} \\ \rho_R \dot{\boldsymbol{\nu}} &= \mathrm{DIV}\,\mathbf{P} \text{ on } \mathcal{B} \\ \dot{\mathbf{Q}} &= -\frac{1}{\tau}\mathbf{Q} + \dot{\mathbf{S}}_e \text{ on } \mathcal{B}\,, \end{aligned} \tag{2.45}$$

with boundary conditions

$$\begin{aligned} \boldsymbol{\phi}(X,t) &= \mathbf{R}(t)X \text{ on } \Gamma_h \\ \boldsymbol{\nu}(X,t) &= \dot{\mathbf{R}}(t)X \text{ on } \Gamma_h \\ \mathbf{PN} &= \mathbf{h} \text{ on } \Gamma_e\,. \end{aligned} \tag{2.46}$$

We express the weak form of these equations, which are needed to apply the finite element method. We first define some function spaces: Let H be the Sobelev space of all functions $f : \mathcal{B} \to \mathbb{R}^2$ which are square integrable and have a square integrable weak derivative. Let H_{hub} be H restricted to those functions which are 0 on the hub. Let $\mathbb{S}$ be the space of 2×2 symmetric matrices and let $H_{\mathbb{S}}$ be the corresponding sobelev space for matrix valued functions $\mathbf{K} : \mathcal{B} \to \mathbb{S}$. Let $\mathbf{H} = H \times H \times H_{\mathbb{S}}$ and $\mathbf{H}_{hub} = H_{hub} \times H_{hub} \times H_{\mathbb{S}}$.

We define our solution function space $\mathbf{V}$: Given a final solution time T, let $\mathbf{V}$ be the set of all $(\boldsymbol{\phi}, \boldsymbol{\nu}, \mathbf{Q}) \in \mathbf{H} \times [0,T]$ such that $\boldsymbol{\phi}(t)$ is twice continuously differentiable in time, and $\boldsymbol{\nu}(t)$ and $\mathbf{Q}(t)$ are once continuously differentiable in time. Our test function space is the set of all triples $(\zeta, \eta, K) \in \mathbf{H}_{hub}$. Formally, we multiply (2.45) by the test functions, integrate, and apply integration by parts to obtain

$$
\begin{aligned}
\int_{\mathcal{B}} \dot{\boldsymbol{\phi}} \cdot \zeta &= \int_{\mathcal{B}} \boldsymbol{\nu} \cdot \zeta \\
\int_{\mathcal{B}} \rho_R \dot{\boldsymbol{\nu}} \cdot \eta &= -\int_{\mathcal{B}} \mathbf{P} : D\eta + \int_{\Gamma_e} \mathbf{h} \cdot \eta \\
\int_{\mathcal{B}} \dot{\mathbf{Q}} : K &= \int_{\mathcal{B}} \left(-\frac{1}{\tau} \mathbf{Q} + \dot{\mathbf{S}}_e \right) : K \,.
\end{aligned}
\tag{2.47}
$$

We define a weak solution to (2.45) to be a triple $(\boldsymbol{\phi}, \boldsymbol{\nu}, \mathbf{Q}) \in \mathbf{V}$ that satisfies (2.47) for all $(\zeta, \eta, K) \in \mathbf{H}_{hub}$ and for all $t \in [0, T]$. Additionally, $\boldsymbol{\phi}$ and $\boldsymbol{\nu}$ must satisfy the boundary conditions $\boldsymbol{\phi}(X, t) = \mathbf{R}(t)X$, $\boldsymbol{\nu}(X, t) = \dot{\mathbf{R}}(t)X$. The boundary condition $\mathbf{PN} = \mathbf{h}$ on Γ_e has been incorporated via the term $\int_{\Gamma_e} \mathbf{h} \cdot \eta$ arising from integration by parts.

We can consider the differential equation defined by (2.47) as a mapping from an initial function triple $(\boldsymbol{\phi}_0, \boldsymbol{\nu}_0, \mathbf{Q}_0) \in \mathbf{H}$ to the evolved solution at time T, $(\boldsymbol{\phi}(T), \boldsymbol{\nu}(T), \mathbf{Q}(T)) \in \mathbf{H}$. This defines a nonlinear mapping $\mathbf{H} \to \mathbf{H}$. When convenient, we denote the triples $(\boldsymbol{\phi}, \boldsymbol{\nu}, \mathbf{Q})$ as $\mathbf{z}$ and write $\mathbf{z}_0$ for initial conditions $(\boldsymbol{\phi}_0, \boldsymbol{\nu}_0, \mathbf{Q}_0)$.

2.11 Linearization

We next compute the linearization of the weak form equations (2.47). First, we clarify our notation: given a function f of $\mathbf{z}$, we use the notation $\hat{f}$ to denote the directional derivative of f about the point $\mathbf{z}$ in a direction $\hat{\mathbf{z}} = (\hat{\boldsymbol{\phi}}, \hat{\boldsymbol{\nu}}, \widehat{\mathbf{Q}})$:

$$
\hat{f} \stackrel{\text{def}}{=} \frac{d}{d\varepsilon}\Big|_{\varepsilon=0} f(\mathbf{z} + \varepsilon \hat{\mathbf{z}}) \,. \tag{2.48}
$$

Furthermore, we require that a direction $\hat{\mathbf{z}} = (\hat{\boldsymbol{\phi}}, \hat{\boldsymbol{\nu}}, \widehat{\mathbf{Q}})$ live in the tangent space $\boldsymbol{\mathcal{T}}(\mathbf{H}_{hub} \times [0, T])$ so that $\mathbf{z} + \varepsilon \hat{\mathbf{z}}$ satisfies the boundary conditions on the hub. If there is danger of confusion, we write $\hat{f}[\mathbf{z}]$ to indicate the point about which f is linearized.

We write the weak form equations as a bilinear form:

$$
\begin{aligned}
\mathcal{L}(\zeta, \eta, K; \mathbf{z}) = &\int_{\mathcal{B}} (\dot{\boldsymbol{\phi}} - \boldsymbol{\nu}) \cdot \zeta \\
&+ \int_{\mathcal{B}} \rho_R \dot{\boldsymbol{\nu}} \cdot \eta + \int_{\mathcal{B}} \mathbf{P} : D\eta - \int_{\Gamma_e} \mathbf{h} \cdot \eta \\
&+ \int_{\mathcal{B}} \left(\dot{\mathbf{Q}} + \frac{1}{\tau} \mathbf{Q} - \dot{\mathbf{S}}_e \right) : K \,.
\end{aligned}
\tag{2.49}
$$

Supressing the dependence of $\mathcal{L}$ on (ζ, η, K), we choose a direction $\hat{\mathbf{z}}$ and compute

$$\begin{aligned}\mathcal{L}(\mathbf{z}+\varepsilon\hat{\mathbf{z}}) = &\int_{\mathcal{B}} (\dot{\boldsymbol{\phi}} + \varepsilon\dot{\hat{\boldsymbol{\phi}}} - \boldsymbol{\nu} - \varepsilon\dot{\hat{\boldsymbol{\nu}}}) \cdot \zeta \\ &+ \left(\int_{\mathcal{B}} \rho_R(\dot{\boldsymbol{\nu}} + \varepsilon\dot{\hat{\boldsymbol{\nu}}}) \cdot \eta + \int_{\mathcal{B}} \mathbf{P}(\mathbf{z}+\varepsilon\hat{\mathbf{z}}) : D\eta - \int_{\Gamma_e} \mathbf{h}(\mathbf{z}-\varepsilon\hat{\mathbf{z}}) \cdot \eta \right) \\ &+ \left(\int_{\mathcal{B}} \left((\dot{\mathbf{Q}} + \varepsilon\dot{\widehat{\mathbf{Q}}} + \frac{1}{\tau}(\mathbf{Q} - \varepsilon\widehat{\mathbf{Q}}) - \dot{\mathbf{S}}_e(\mathbf{z}-\varepsilon\hat{\mathbf{z}}) \right) : K \right) .\end{aligned} \tag{2.50}$$

Here, we are considering $\mathbf{P}, \mathbf{h}$ and $\dot{\mathbf{S}}_e$ as functions of $\mathbf{z}$. Next, we take the derivative with respect to ε to obtain $\widehat{\mathcal{L}}$:

$$\begin{aligned}\widehat{\mathcal{L}} &= \frac{d}{d\varepsilon}|_{\varepsilon=0}\mathcal{L}(\mathbf{z}+\varepsilon\hat{\mathbf{z}}) \\ &= \int_{\mathcal{B}} (\dot{\hat{\boldsymbol{\phi}}} - \hat{\boldsymbol{\nu}}) \cdot \zeta \\ &+ \left(\int_{\mathcal{B}} \rho_R \dot{\hat{\boldsymbol{\nu}}} \cdot \eta + \int_{\mathcal{B}} \widehat{\mathbf{P}} : D\eta - \int_{\Gamma_e} \widehat{\mathbf{h}} \cdot \eta \right) \\ &+ \left(\int_{\mathcal{B}} \left(\dot{\widehat{\mathbf{Q}}} + \frac{1}{\tau}\widehat{\mathbf{Q}} - \dot{\widehat{\mathbf{S}}}_e \right) : K \right) .\end{aligned} \tag{2.51}$$

The weak form equations corresponding to $\widehat{\mathcal{L}}$ are then

$$\begin{aligned}\int_{\mathcal{B}} \dot{\hat{\boldsymbol{\phi}}} \cdot \zeta &= \int_{\mathcal{B}} \hat{\boldsymbol{\nu}} \cdot \zeta \\ \int_{\mathcal{B}} \rho_R \dot{\hat{\boldsymbol{\nu}}} \cdot \eta &= -\int_{\mathcal{B}} \widehat{\mathbf{P}} : D\eta + \int_{\Gamma_e} \widehat{\mathbf{h}} \cdot \eta \\ \int_{\mathcal{B}} \dot{\widehat{\mathbf{Q}}} : K &= \int_{\mathcal{B}} \left(-\frac{1}{\tau}\widehat{\mathbf{Q}} + \dot{\widehat{\mathbf{S}}}_e \right) : K .\end{aligned} \tag{2.52}$$

We call the above equations the linearized weak form equations. Consequently, given $\mathbf{z}$ which solves the weak form equations (2.47) and $\hat{\mathbf{z}}$ which solves the linearized weak form equations (2.52), $\mathbf{z} + \varepsilon\hat{\mathbf{z}}$ solves the weak form equations (2.47) to order ε^2. See the appendix for a detailed computation of $\widehat{\mathbf{P}}, \widehat{\mathbf{h}}$, and $\dot{\widehat{\mathbf{S}}}_e$ in terms of $\mathbf{z}$ and $\hat{\mathbf{z}}$.

Chapter 3

Time periodic and steady state solutions

3.1 Time periodic solutions for the treaded tire

We seek solutions to the evolution equations (2.47) for the treaded rolling tire that return to the same shape as their initial configuration after some period T. Due to the boundary conditions on the hub, the standard time periodic correlation $\boldsymbol{\phi}(X,T) = \boldsymbol{\phi}(X,0)$ can only hold when $T = 2\pi n/\omega$ for positive integer n; i.e. the tire makes one or more full revolutions. Since we are interested in the shape of the tire returning to its initial shape and not necessarily a material point returning to its initial location (see Fig. 3.1), we instead look for motions of the tire which satisfy

$$\boldsymbol{\phi}(\mathbf{R}^{\mathsf{T}}(T)X,T) = \boldsymbol{\phi}(X,0)\,. \tag{3.1}$$

Thus if a material point X is mapped by $\boldsymbol{\phi}(0)$ to a point x in the deformed configuration, $\boldsymbol{\phi}(T)$ maps the material point $X_R = \mathbf{R}^{\mathsf{T}}(T)X$ to the same point x in the deformed configuration. $X_R = \mathbf{R}^{\mathsf{T}}(T)X$ is obtained by rotating X backwards for time T. Fig. 3.1 demonstrates this situation with $T\omega = \pi/2$, so that the tire makes a quarter revolution.

The number of tread blocks, β, constrains the possible values of the period T. Since the tread blocks must align with the initial configuration, $T = 2\pi n/(\beta\omega)$, where n is any positive integer.

To formalize the operation of "rotating X backwards", we define the operator $\mathcal{U}_T$ which transforms a function f defined on $\mathcal{B}\times\mathbb{R}$ by

$$\mathcal{U}_T(f)(X,T) = f(\mathbf{R}^{\mathsf{T}}X,T)\,. \tag{3.2}$$

(Note: we write $\mathbf{R}$ for $\mathbf{R}(T)$ or $\mathbf{R}(t)$ when there is little danger of confusion.)

Using $\mathcal{U}_T$, we can rewrite the time periodic condition on $\boldsymbol{\phi}$ as (dropping the dependence on X)

$$\mathcal{U}_T\boldsymbol{\phi}(T) = \boldsymbol{\phi}(0)\,. \tag{3.3}$$

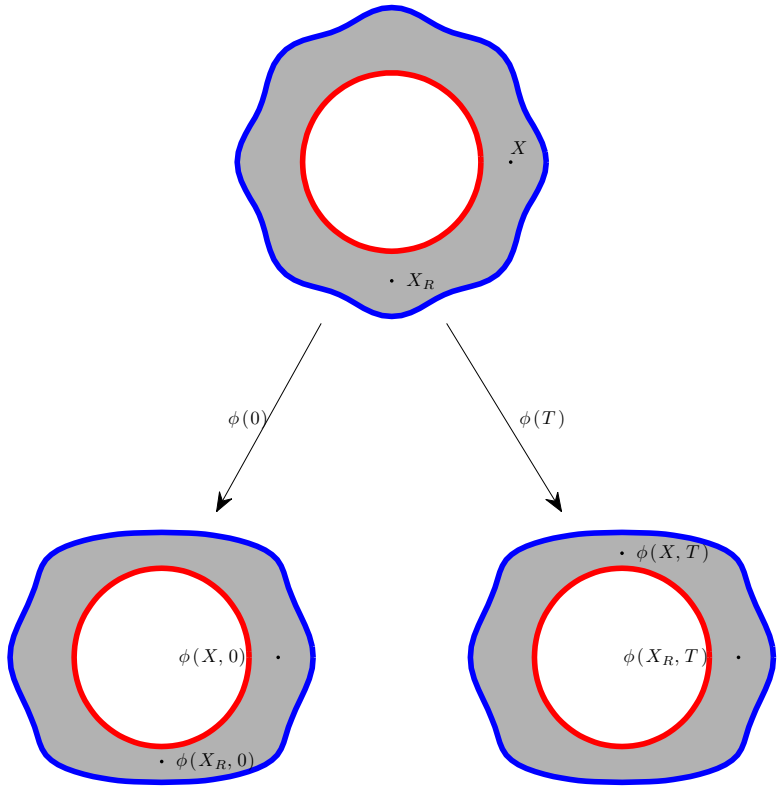

Figure 3.1: The top figure is the reference configuration with material points X and $X_R = \mathbf{R}^\mathsf{T}(T)X$. At bottom left is the deformed configuration at time 0. At bottom right is the deformed configuration at time T, for which the tire is the same shape as at time 0. We observe that $\boldsymbol{\phi}(X_R, T) = \boldsymbol{\phi}(X, 0)$.

The velocity of a time periodic motion behaves similarly:

$$\mathcal{U}_T \boldsymbol{\nu}(T) = \boldsymbol{\nu}(0)\,. \tag{3.4}$$

However, we do not expect $\mathbf{Q}$ to satisfy $\mathbf{Q}(\mathbf{R}^\mathsf{T}X, T) = \mathbf{Q}(X, 0)$, because $\mathbf{Q}$ is a tensor defined on the reference configuration and does not map to the deformed configuration as do $\boldsymbol{\phi}$ and $\boldsymbol{\nu}$. Instead, we compute that if $\boldsymbol{\phi}(\mathbf{R}^\mathsf{T}X, T) = \boldsymbol{\phi}(X, 0)$, then

$$\begin{aligned} \mathbf{F}(\mathbf{R}^\mathsf{T}X, T)\mathbf{R}^\mathsf{T} &= \mathbf{F}(X, 0) \\ \mathbf{R}\mathbf{C}(\mathbf{R}^\mathsf{T}X, T)\mathbf{R}^\mathsf{T} &= \mathbf{C}(X, 0)\,. \end{aligned} \tag{3.5}$$

One can verify that $\mathbf{S}_e$ follows the same relationship as $\mathbf{C}$:

$$\mathbf{R}\mathbf{S}_e(\mathbf{R}^\mathsf{T}X, T)\mathbf{R}^\mathsf{T} = \mathbf{S}_e(X, 0)\,. \tag{3.6}$$

Since time periodicity with period T also implies $\boldsymbol{\phi}(\mathbf{R}^\mathsf{T}X, T + s) = \boldsymbol{\phi}(X, s)$ and hence $\mathbf{R}\mathbf{S}_e(\mathbf{R}^\mathsf{T}X, T + s)\mathbf{R}^\mathsf{T} = \mathbf{S}_e(X, s)$, we can check from the definition of $\mathbf{Q}$ in (2.22) that $\mathbf{Q}$

satisfies

$$\mathbf{R}\mathbf{Q}(\mathbf{R}^{\mathsf{T}}X,T)\mathbf{R}^{\mathsf{T}} = \mathbf{Q}(X,0)\,. \tag{3.7}$$

Thus we define a time periodic solution with period T to satisfy

$$\begin{aligned} \mathcal{U}_T\boldsymbol{\phi}(T) &= \boldsymbol{\phi}(0) \\ \mathcal{U}_T\boldsymbol{\nu}(T) &= \boldsymbol{\nu}(0) \\ \mathbf{R}\mathcal{U}_T\mathbf{Q}(T)\mathbf{R}^{\mathsf{T}} &= \mathbf{Q}(0)\,. \end{aligned} \tag{3.8}$$

We define the linear operator $\boldsymbol{\mathcal{U}}_T : \mathbf{H} \to \mathbf{H}$ by

$$\boldsymbol{\mathcal{U}}_T((\boldsymbol{\phi},\boldsymbol{\nu},\mathbf{Q})) = (\mathcal{U}_T\boldsymbol{\phi}, \mathcal{U}_T\boldsymbol{\nu}, \mathbf{R}\mathcal{U}_T\mathbf{Q}\mathbf{R}^{\mathsf{T}})), \tag{3.9}$$

and the functional $\mathcal{F}_T : \mathbf{H} \to \mathbf{H}$ by

$$\mathcal{F}_T(\mathbf{z}_0) = \boldsymbol{\mathcal{U}}_T(\mathbf{z}(T)) - \mathbf{z}_0, \tag{3.10}$$

where $\mathbf{z}$ solves the weak form equations with initial condition $\mathbf{z}_0$. We may now write the time periodic equations (3.8) as

$$\mathcal{F}_T(\mathbf{z}_0) = \mathbf{0}\,. \tag{3.11}$$

To solve $\mathcal{F}_T(\mathbf{z}_0) = \mathbf{0}$ we will apply Newton's method which requires the derivative of $\mathcal{F}_T(\mathbf{z}_0)$ with respect to $\mathbf{z}_0$:

$$\widehat{\mathcal{F}}_T = \boldsymbol{\mathcal{U}}_T(\hat{\mathbf{z}}(T)) - \hat{\mathbf{z}}_0\,. \tag{3.12}$$

Here $\hat{\mathbf{z}}(X,t)$ evolves according to the linearized equations (2.52) with initial condition $\hat{\mathbf{z}}_0$.

Given this definition of time periodic solution for the tire, we seek initial conditions $\mathbf{z}_0 = (\boldsymbol{\phi}_0, \boldsymbol{\nu}_0, \mathbf{Q}_0)$ that give rise to a time periodic solution. In addition to solving the equation $\mathcal{F}_T(\mathbf{z}_0) = \mathbf{0}$, we can find solutions by defining a scalar functional $\mathcal{G}_T$ which gives a measure of how close a given initial condition comes to satisfying time periodicity:

$$\mathcal{G}_T(\mathbf{z}_0) = \frac{1}{2}\int_{\mathcal{B}} \|\mathcal{U}_T\boldsymbol{\phi}(T) - \boldsymbol{\phi}_0\|^2 + \|\mathcal{U}_T\boldsymbol{\nu}(T) - \boldsymbol{\nu}_0\|^2 + \|\mathbf{R}\mathcal{U}_T\mathbf{Q}(T)\mathbf{R}^{\mathsf{T}} - \mathbf{Q}_0\|^2\,. \tag{3.13}$$

The norm $\|\cdot\|$ used for the $\boldsymbol{\phi}$ and $\boldsymbol{\nu}$ terms is the euclidean norm, while the norm used for the $\mathbf{Q}$ term is the frobenius norm. These norms are also nondimensionalized by characteristic length factors u_{char}, v_{char} and Q_{char}, respectively. These norms arise from inner products, which we shall denote by $\langle\cdot,\cdot\rangle$.

The utility of $\mathcal{G}_T$ is that we can minimize it over initial conditions $\mathbf{z}_0$ and if $\mathcal{G}_T$ is zero, then we have found a time periodic solution. Minimization algorithms often require the derivative of the objective function, so we compute the directional derivative of $\mathcal{G}_T$ at a point $\mathbf{z}_0 = (\boldsymbol{\phi}_0, \boldsymbol{\nu}_0, \mathbf{Q}_0)$ with respect to a variation $\hat{\mathbf{z}}_0 = (\hat{\boldsymbol{\phi}}_0, \hat{\boldsymbol{\nu}}_0, \widehat{\mathbf{Q}}_0)$:

$$\begin{aligned} \hat{\mathcal{G}}_T = \int_{\mathcal{B}} &\left\langle \mathcal{U}_T\boldsymbol{\phi}(T) - \boldsymbol{\phi}_0\,,\, \mathcal{U}_T\hat{\boldsymbol{\phi}}(T) - \hat{\boldsymbol{\phi}}_0 \right\rangle \\ &+ \langle \mathcal{U}_T\boldsymbol{\nu}(T) - \boldsymbol{\nu}_0\,,\, \mathcal{U}_T\hat{\boldsymbol{\nu}}(T) - \hat{\boldsymbol{\nu}}_0 \rangle \\ &+ \left\langle \mathbf{R}\mathcal{U}_T\mathbf{Q}(T)\mathbf{R} - \mathbf{Q}_0\,,\, \mathbf{R}\mathcal{U}_T\widehat{\mathbf{Q}}(T)\mathbf{R}^{\mathsf{T}} - \widehat{\mathbf{Q}}_0 \right\rangle\,, \end{aligned} \tag{3.14}$$

where $(\boldsymbol{\phi}, \boldsymbol{\nu}, \mathbf{Q})$ evolve according to the weak form equations and $(\hat{\boldsymbol{\phi}}, \hat{\boldsymbol{\nu}}, \widehat{\mathbf{Q}})$ evolve according to the linearized weak form equations.

3.2 Time periodic solutions for the smooth tire

In contrast to the treaded tire case, time periodic solutions of the smooth tire can be sought for any period T. In addition, the period can be allowed to vary as an independent variable, in which case root-finding or minimization algorithms require derivatives of $\mathcal{F}_T$ and $\mathcal{G}_T$ with respect to T. In turn, these depend on the T derivative of $\mathcal{U}_T$:

$$\begin{aligned} \frac{\partial}{\partial T}\left(\mathcal{U}_T f\right) &= \frac{\partial}{\partial T}\left(f(\mathbf{R}^\mathsf{T} X, T)\right) = \frac{\partial f}{\partial T}(\mathbf{R}^\mathsf{T} X, T) + Df(\mathbf{R}^\mathsf{T} X, T)\dot{\mathbf{R}}^\mathsf{T} X \\ &= \frac{\partial f}{\partial T}(\mathbf{R}^\mathsf{T} X, T) + Df(\mathbf{R}^\mathsf{T} X, T)\dot{\mathbf{R}}^\mathsf{T}\mathbf{R}\mathbf{R}^\mathsf{T} X = \mathcal{U}_T\left(\frac{\partial f}{\partial T} - Df\boldsymbol{\Omega} X\right), \end{aligned} \tag{3.15}$$

where $\boldsymbol{\Omega}$ is the skew-symmetric matrix

$$\boldsymbol{\Omega} = \dot{\mathbf{R}}\mathbf{R}^\mathsf{T} = \omega \begin{bmatrix} 0 & -1 \\ 1 & 0 \end{bmatrix}. \tag{3.16}$$

Note that $\boldsymbol{\Omega}$ is independent of T, even though $\mathbf{R}$ and $\dot{\mathbf{R}}$ do depend on T. We return to the derivatives of $\mathcal{G}_T$ and $\mathcal{F}_T$ with respect to T:

$$\begin{aligned} \frac{\partial}{\partial T}\mathcal{G}_T = &\int_{\mathcal{B}} \left\langle \mathcal{U}_T\boldsymbol{\phi}(T) - \boldsymbol{\phi}_0\,, \mathcal{U}_T(\dot{\boldsymbol{\phi}}(T) - D\boldsymbol{\phi}(T)\boldsymbol{\Omega} X)\right\rangle \\ &+ \langle \mathcal{U}_T\boldsymbol{\nu}(T) - \boldsymbol{\nu}_0\,, \mathcal{U}_T(\dot{\boldsymbol{\nu}}(T) - D\boldsymbol{\nu}(T)\boldsymbol{\Omega} X)\rangle \\ &+ \Big\langle \mathbf{R}\mathcal{U}_T\mathbf{Q}(T)\mathbf{R} - \mathbf{Q}_0\,, \mathcal{U}_T\Big(\mathbf{R}(\dot{\mathbf{Q}}(T) - D\mathbf{Q}(T)\boldsymbol{\Omega} X)\mathbf{R}^\mathsf{T} \\ &+ \dot{\mathbf{R}}\mathbf{Q}(T)\mathbf{R}^\mathsf{T} + \mathbf{R}\mathbf{Q}(T)\dot{\mathbf{R}}^\mathsf{T}\Big)\Big\rangle\,, \end{aligned} \tag{3.17}$$

$$\frac{\partial}{\partial T}\mathcal{F}_T = \begin{pmatrix} \mathcal{U}_T(\dot{\boldsymbol{\phi}}(T) - D\boldsymbol{\phi}(T)\boldsymbol{\Omega} X) \\ \mathcal{U}_T(\dot{\boldsymbol{\nu}}(T) - D\boldsymbol{\nu}(T)\boldsymbol{\Omega} X) \\ \mathcal{U}_T\left(\mathbf{R}(\dot{\mathbf{Q}}(T) - D\mathbf{Q}(T)\boldsymbol{\Omega} X)\mathbf{R}^\mathsf{T} + \dot{\mathbf{R}}\mathbf{Q}(T)\mathbf{R}^\mathsf{T} + \mathbf{R}\mathbf{Q}(T)\dot{\mathbf{R}}^\mathsf{T}\right) \end{pmatrix}. \tag{3.18}$$

3.3 Steady state solutions

Next we describe the steady state equations for the rolling tire. We define a steady state solution of the smooth tire to be one that satisfies time periodicity for all times t: $\mathcal{F}_t(\mathbf{z}_0) = \mathbf{0}$. In this section, we write $\mathcal{F}(\mathbf{z}_0, t)$ for $\mathcal{F}_t(\mathbf{z}_0)$ so that the steady state equation becomes

$$\mathcal{F}(\mathbf{z}_0, t) = \mathbf{0} \text{ for all } t\,. \tag{3.19}$$

Since time periodicity for the treaded tire is only defined for discrete times, there is no notion of a steady state solution for the treaded tire.

We show below that $\mathbf{z}_0$ satisfying $\partial_t \mathcal{F}(\mathbf{z}_0, 0) = \mathbf{0}$ are steady state solutions. We follow a common approach in the literature for solving the steady state problem (see [4, 24, 26, 19, 12, 20, 27, 14]) and introduce a new spatial variable $\widetilde{X}$ defined by

$$\mathbf{R}(t)\widetilde{X} = X\,. \tag{3.20}$$

We define the motions corresponding to the new variable:

$$\begin{aligned} \widetilde{\boldsymbol{\phi}}(\widetilde{X}, t) &= \boldsymbol{\phi}(X, t) \\ \widetilde{\boldsymbol{\nu}}(\widetilde{X}, t) &= \boldsymbol{\nu}(X, t) \\ \widetilde{\mathbf{Q}}(\widetilde{X}, t) &= \mathbf{R}\mathbf{Q}(X, t)\mathbf{R}^{\mathsf{T}}\,. \end{aligned} \tag{3.21}$$

We refer to the triple $(\widetilde{\boldsymbol{\phi}}, \widetilde{\boldsymbol{\nu}}, \widetilde{\mathbf{Q}})$ as $\widetilde{\mathbf{z}}$. Note that $\widetilde{\mathbf{z}}(\widetilde{X}, t) = \boldsymbol{\mathcal{U}}_t(\mathbf{z}(X, t))$. We also define quantities related to the transformed motion:

$$\begin{aligned} \widetilde{\mathbf{F}} &= \widetilde{D}\widetilde{\boldsymbol{\phi}} \\ \widetilde{\mathbf{C}} &= \widetilde{\mathbf{F}}^{\mathsf{T}}\widetilde{\mathbf{F}} \\ \widetilde{\mathbf{P}}_e &= \frac{\kappa}{2}(\widetilde{I}_3 - 1)\widetilde{\mathbf{F}}^{-T} + \mu(1-s)(\widetilde{\mathbf{F}} - \widetilde{\mathbf{F}}^{-T}) + \mu s(\widetilde{I}_1\widetilde{\mathbf{F}} - \widetilde{\mathbf{F}}\widetilde{\mathbf{C}} - 2\widetilde{\mathbf{F}}^{-T}) \\ \widetilde{\mathbf{P}} &= \widetilde{\mathbf{P}}_e + \nu\widetilde{\mathbf{Q}} \\ \widetilde{\mathbf{h}} &= \delta\gamma(-h - \widetilde{\boldsymbol{\phi}}^2)\mathbf{e}_2 \\ \widetilde{\dot{\mathbf{F}}} &= \widetilde{D}\widetilde{\boldsymbol{\nu}} \\ \widetilde{\dot{\mathbf{C}}} &= \widetilde{\dot{\mathbf{F}}}^{\mathsf{T}}\widetilde{\mathbf{F}} + \widetilde{\dot{\mathbf{F}}}^{\mathsf{T}}\widetilde{\dot{\mathbf{F}}} \\ \widetilde{\dot{\det \mathbf{C}}} &= \det\widetilde{\mathbf{C}}\,\mathrm{tr}(\widetilde{\mathbf{C}}^{-1}\widetilde{\dot{\mathbf{C}}}) \\ \widetilde{\dot{\mathbf{C}^{-1}}} &= -\widetilde{\mathbf{C}}^{-1}\widetilde{\dot{\mathbf{C}}}\widetilde{\mathbf{C}}^{-1} \\ \widetilde{\dot{\mathbf{S}}}_e &= \frac{\kappa}{2}\left[\widetilde{(\dot{\det \mathbf{C}})}\widetilde{\mathbf{C}}^{-1} + (\det\widetilde{\mathbf{C}} - 1)\widetilde{\dot{\mathbf{C}^{-1}}}\right] \\ &\quad + \mu(1-s)\left(-\widetilde{\dot{\mathbf{C}^{-1}}}\right) + \mu s\left((\mathrm{tr}\,\widetilde{\dot{\mathbf{C}}})\mathbf{I} - \widetilde{\dot{\mathbf{C}}} - 2\widetilde{\dot{\mathbf{C}^{-1}}}\right)\,. \end{aligned} \tag{3.22}$$

Here $\widetilde{D}$ refers to differentiation with respect to $\widetilde{X}$. It can be checked that analagous quantities (e.g. $\mathbf{F}$ and $\widetilde{\mathbf{F}}$) are related to each through $\mathbf{R}(t)$ in a simple way, which could also be taken

as definitions. For example,

$$\begin{aligned}
\widetilde{\mathbf{F}}(\widetilde{X},t) &= \mathbf{F}(X,t)\mathbf{R}^{\mathsf{T}} \\
\widetilde{\mathbf{C}}(\widetilde{X},t) &= \mathbf{R}\mathbf{C}(X,t)\mathbf{R}^{\mathsf{T}} \\
\widetilde{\mathbf{P}}_e(\widetilde{X},t) &= \mathbf{P}_e(X,t)\mathbf{R}^{\mathsf{T}} \\
\widetilde{\dot{\mathbf{S}}}_e(\widetilde{X},t) &= \mathbf{R}\dot{\mathbf{S}}_e(X,t)\mathbf{R}^{\mathsf{T}}\,.
\end{aligned} \tag{3.23}$$

Using the above definitions, we can compute that $\widetilde{\mathbf{z}}$ evolves according to the following system of equations:

$$\begin{aligned}
\int_{\mathcal{B}} \dot{\widetilde{\boldsymbol{\phi}}} \cdot \zeta &= \int_{\mathcal{B}} (\widetilde{\boldsymbol{\nu}} - \widetilde{\mathbf{F}}\boldsymbol{\Omega}\widetilde{X}) \cdot \zeta \\
\int_{\mathcal{B}} \dot{\widetilde{\boldsymbol{\nu}}} \cdot \eta &= \int_{\mathcal{B}} -\frac{1}{\rho_R}\widetilde{\mathbf{P}} : \widetilde{D}\eta - \dot{\widetilde{\mathbf{F}}}\boldsymbol{\Omega}\widetilde{X} \cdot \eta + \int_{\Gamma_e} \widetilde{\mathbf{h}} \cdot \eta \\
\int_{\mathcal{B}} \dot{\widetilde{\mathbf{Q}}} : K &= \int_{\mathcal{B}} \left(-\frac{1}{\tau}\widetilde{\mathbf{Q}}(t) + \dot{\widetilde{\mathbf{S}}}_e(t) + \boldsymbol{\Omega}\widetilde{\mathbf{Q}} - \widetilde{\mathbf{Q}}\boldsymbol{\Omega} - \widetilde{D}\widetilde{\mathbf{Q}}\boldsymbol{\Omega}\widetilde{X} \right) : K\,.
\end{aligned} \tag{3.24}$$

This gives an alternative way to define $\mathcal{F}$:

$$\mathcal{F}(\widetilde{\mathbf{z}}_0,t) = \widetilde{\mathbf{z}}(t) - \widetilde{\mathbf{z}}_0\,, \tag{3.25}$$

where $\widetilde{\mathbf{z}}$ evolves according to (3.24). To find a solution to $\mathcal{F}(\widetilde{\mathbf{z}}_0,t) = \mathbf{0}$ for all t, we need only find an initial condition $\widetilde{\mathbf{z}}_0$ that satisifes

$$\partial_t \mathcal{F}(\widetilde{\mathbf{z}}_0,0) = \dot{\widetilde{\mathbf{z}}}_0 = (\dot{\widetilde{\boldsymbol{\phi}}}_0, \dot{\widetilde{\boldsymbol{\nu}}}_0, \dot{\widetilde{\mathbf{Q}}}_0) = \mathbf{0}\,. \tag{3.26}$$

Since at time $t = 0$, $\mathbf{z} = \widetilde{\mathbf{z}}$, we have proved our earlier statement that $\partial_t \mathcal{F}(\mathbf{z}_0,0) = \mathbf{0}$ gives the steady state solution.

Because we are only interested in solving $\partial_t \mathcal{F} = \mathbf{0}$ at time $t = 0$, we define the differential operator $\mathcal{S}(\widetilde{\mathbf{z}}_0) = \partial_t \mathcal{F}(\widetilde{\mathbf{z}}_0,0)$. Below, we drop the subscript 0 and write $\mathcal{S}(\widetilde{\mathbf{z}})$. Given $\widetilde{\mathbf{z}}$, we compute $\dot{\widetilde{\mathbf{z}}} = \mathcal{S}(\widetilde{\mathbf{z}})$ by solving the equations (3.24). The steady state equations can be then be written as

$$\mathcal{S}(\widetilde{\mathbf{z}}) = \mathbf{0}\,. \tag{3.27}$$

We note the linearized equations corresponding to (3.24). For ease of notation, we drop the $\widetilde{\ }$.

$$\begin{aligned}
\int_{\mathcal{B}} \dot{\widehat{\boldsymbol{\phi}}} \cdot \zeta &= \int_{\mathcal{B}} (\widehat{\boldsymbol{\nu}} - \widehat{\mathbf{F}}\boldsymbol{\Omega}X) \cdot \zeta \\
\int_{\mathcal{B}} \dot{\widehat{\boldsymbol{\nu}}} \cdot \eta &= \int_{\mathcal{B}} -\frac{1}{\rho_R}\widehat{\mathbf{P}} : D\eta - \dot{\widehat{\mathbf{F}}}\boldsymbol{\Omega}X \cdot \eta + \int_{\Gamma_e} \widehat{\mathbf{h}} \cdot \eta \\
\int_{\mathcal{B}} \dot{\widehat{\mathbf{Q}}} : K &= \int_{\mathcal{B}} \left(-\frac{1}{\tau}\widehat{\mathbf{Q}}(t) + \dot{\widehat{\mathbf{S}}}_e(t) + \boldsymbol{\Omega}\widehat{\mathbf{Q}} - \widehat{\mathbf{Q}}\boldsymbol{\Omega} - D\widehat{\mathbf{Q}}\boldsymbol{\Omega}X \right) : K\,.
\end{aligned} \tag{3.28}$$

3.4 Hamiltonian structure of the elastic equations

If we ignore viscoelasticity and the presence of the road, the equations of motion are

$$\begin{aligned} \int_{\mathcal{B}} \dot{\boldsymbol{\phi}} \cdot \zeta &= \int_{\mathcal{B}} \boldsymbol{\nu} \cdot \zeta \\ \int_{\mathcal{B}} \rho_R \dot{\boldsymbol{\nu}} \cdot \eta &= -\int_{\mathcal{B}} \mathbf{P}_e : D\eta \,. \end{aligned} \tag{3.29}$$

By virtue of the existence of a stored energy function, this system is Hamiltonian, with the Hamiltonian function given by

$$\int_{\mathcal{B}} \boldsymbol{\Psi}_e + \frac{1}{2}\rho_R \boldsymbol{\nu} \cdot \boldsymbol{\nu} \,. \tag{3.30}$$

This is a non-autonomous system due to the rotation of the hub.

In the case of the transformed variables, from (3.24) we have already computed that $\widetilde{\boldsymbol{\phi}}$ and $\widetilde{\boldsymbol{\nu}}$ satisfy

$$\begin{aligned} \int_{\mathcal{B}} \dot{\widetilde{\boldsymbol{\phi}}} \cdot \zeta &= \int_{\mathcal{B}} (\widetilde{\boldsymbol{\nu}} - \widetilde{\mathbf{F}}\boldsymbol{\Omega}\widetilde{X}) \cdot \zeta \\ \int_{\mathcal{B}} \dot{\widetilde{\boldsymbol{\nu}}} \cdot \eta &= \int_{\mathcal{B}} -\frac{1}{\rho_R}\widetilde{\mathbf{P}}_e : D\eta - \dot{\widetilde{\mathbf{F}}}\boldsymbol{\Omega}\widetilde{X} \cdot \eta \,. \end{aligned} \tag{3.31}$$

A computation shows that the above evolution equations arise from the following autonomous Hamiltonian:

$$\mathcal{H} = \int_{\mathcal{B}} \widetilde{\boldsymbol{\Psi}}_e + \frac{1}{2}\rho_R \widetilde{\boldsymbol{\nu}} \cdot \widetilde{\boldsymbol{\nu}} - \rho_R(\widetilde{\mathbf{F}}\boldsymbol{\Omega}\widetilde{X}) \cdot \widetilde{\boldsymbol{\nu}} \,, \tag{3.32}$$

where $\widetilde{\boldsymbol{\Psi}}_e$ is defined from the invariants of $\widetilde{\mathbf{C}}$ in the same way that $\boldsymbol{\Psi}_e$ is defined from the invariants of $\mathbf{C}$. Let $\mathcal{S}_H$ be the corresponding differential operator for these equations; i.e. $(\dot{\widetilde{\boldsymbol{\phi}}}, \dot{\widetilde{\boldsymbol{\nu}}}) = \mathcal{S}_H(\widetilde{\boldsymbol{\phi}}, \widetilde{\boldsymbol{\nu}})$, where $\dot{\widetilde{\boldsymbol{\phi}}}, \dot{\widetilde{\boldsymbol{\nu}}}, \widetilde{\boldsymbol{\phi}}, \widetilde{\boldsymbol{\nu}}$ satisfy (3.31). In addition, Hamilton's equations hold: $\mathcal{S}_H = (\partial\mathcal{H}/\partial\widetilde{\boldsymbol{\nu}}, -\partial\mathcal{H}/\partial\widetilde{\boldsymbol{\phi}})$.

Below, we discretize our equations and obtain a finite dimensional Hamiltonian system for which we can apply stability theory. In particular, let $\bar{\mathcal{H}}$ be the discretized Hamiltonian and let $\bar{\mathcal{S}}_H$ be the discretization of $\mathcal{S}_H$. The Hessian of $\bar{\mathcal{H}}$ is related to the Jacobian of $\bar{\mathcal{S}}_H$ by $D\bar{\mathcal{S}}_H = \mathcal{J} D^2\bar{\mathcal{H}}$, where $\mathcal{J}$ is the skew-symmetric matrix $\begin{bmatrix} \mathbf{0} & \mathbf{I} \\ -\mathbf{I} & \mathbf{0} \end{bmatrix}$.

When investigating eigenvalues of $D\bar{\mathcal{S}}_H$ in §5.6, we use the following theorem about the stability in Hamiltonian systems. Let $\mathbf{z}$ be a critical point of $\bar{\mathcal{H}}$. If the matrix $D^2\bar{\mathcal{H}}$ is positive definite at $\mathbf{z}$, then $\mathbf{z}$ is Lyapunov stable, since energy level sets near $\bar{\mathcal{H}}(\mathbf{z})$ remain close to $\mathbf{z}$. In turn, Lyrapunov stability implies that the eigenvalues of $D\bar{\mathcal{S}}_H$ are purely imaginary, since otherwise $\mathbf{z}$ would be linearly unstable either forward or backward in time.

Chapter 4

Numerical methods

4.1 Displacement formulation

The equations of motion for the viscoelastic tire evolve the three variables $\boldsymbol{\phi}, \boldsymbol{\nu}, \mathbf{Q}$. However, our numerical methods evolve the displacement from the steady rolling motion instead of evolving the full motion. Let the displacement variable $\mathbf{u}$ and its velocity $\mathbf{v}$ be given by

$$\begin{aligned} \mathbf{u}(X,t) &\stackrel{\text{def}}{=} \boldsymbol{\phi}(X,t) - \mathbf{R}(t)X \\ \mathbf{v}(X,t) &\stackrel{\text{def}}{=} \dot{\mathbf{u}}(X,t) = \boldsymbol{\nu}(X,t) - \dot{\mathbf{R}}(t)X\,. \end{aligned} \tag{4.1}$$

From these we can compute $\mathbf{F}$, $\dot{\mathbf{F}}$ by

$$\mathbf{F} = D\mathbf{u} + \mathbf{R}\,, \quad \dot{\mathbf{F}} = D\mathbf{v} + \dot{\mathbf{R}}\,; \tag{4.2}$$

hence we may compute $\mathbf{P}, \mathbf{h}, \dot{\mathbf{S}}_e$ etc. as before. We also have

$$\dot{\mathbf{v}} = \dot{\boldsymbol{\nu}} + \omega^2 \mathbf{R} X\,, \tag{4.3}$$

since $\ddot{\mathbf{R}} = -\omega^2 \mathbf{R}$. The displacement equations are

$$\begin{aligned} \int_{\mathcal{B}} \dot{\mathbf{u}} \cdot \zeta &= \int_{\mathcal{B}} \mathbf{v} \cdot \zeta \\ \int_{\mathcal{B}} \rho_R(\dot{\mathbf{v}} - \omega^2 \mathbf{R} X) \cdot \eta &= -\int_{\mathcal{B}} \mathbf{P} : D\eta + \int_{\Gamma_e} \mathbf{h} \cdot \eta \\ \int_{\mathcal{B}} \dot{\mathbf{Q}} : K &= \int_{\mathcal{B}} \left(-\frac{1}{\tau}\mathbf{Q} + \dot{\mathbf{S}}_e \right) : K\,, \end{aligned} \tag{4.4}$$

with boundary conditions that $\mathbf{u}$ and $\mathbf{v}$ are zero on Γ_h.

The time periodic solutions equations (3.8) and functional $\mathcal{G}_T$ (3.13) become

$$\begin{aligned} \mathcal{U}_T \mathbf{u}(T) &= \mathbf{u}(0) \\ \mathcal{U}_T \mathbf{v}(T) &= \mathbf{v}(0) \\ \mathbf{R}\mathcal{U}_T \mathbf{Q}(T) \mathbf{R}^{\mathsf{T}} &= \mathbf{Q}(0)\,, \end{aligned} \tag{4.5}$$

$$\mathcal{G}_T(\mathbf{z}_0) = \frac{1}{2}\int_{\mathcal{B}} \|\mathcal{U}_T\mathbf{u}(T) - \mathbf{u}_0\|^2 + \|\mathcal{U}_T\mathbf{v}(T) - \mathbf{v}_0\|^2 + \|\mathbf{R}\mathcal{U}_T\mathbf{Q}(T)\mathbf{R}^\mathsf{T} - \mathbf{Q}_0\|^2 \,. \tag{4.6}$$

We also define the transformed displacement variables:

$$\begin{aligned} \widetilde{\mathbf{u}}(\widetilde{X},t) &\stackrel{\text{def}}{=} \widetilde{\boldsymbol{\phi}}(\widetilde{X},t) - \widetilde{X} \\ \widetilde{\mathbf{v}}(\widetilde{X},t) &\stackrel{\text{def}}{=} \widetilde{\boldsymbol{\nu}}(\widetilde{X},t) - \boldsymbol{\Omega}\widetilde{X} \,. \end{aligned} \tag{4.7}$$

The equations (3.24) for the displacement variables can be written

$$\begin{aligned} \int_{\mathcal{B}} \dot{\widetilde{\mathbf{u}}} \cdot \zeta &= \int_{\mathcal{B}} (\widetilde{\mathbf{v}} + \boldsymbol{\Omega}\widetilde{X}) \cdot \zeta - (\widetilde{D}\widetilde{\mathbf{u}} + \mathbf{I})\boldsymbol{\Omega}\widetilde{X} \cdot \zeta \\ \int_{\mathcal{B}} \dot{\widetilde{\mathbf{v}}} \cdot \eta &= \int_{\mathcal{B}} \left[-\frac{1}{\rho_R}\widetilde{\mathbf{P}} : \widetilde{D}\eta - (\widetilde{D}\widetilde{\mathbf{v}} + \boldsymbol{\Omega})\boldsymbol{\Omega}\widetilde{X} \cdot \eta \right] + \int_{\Gamma_e} \frac{1}{\rho_R}\widetilde{\mathbf{h}} \cdot \eta \\ \int_{\mathcal{B}} \dot{\widetilde{\mathbf{Q}}} : K &= \int_{\mathcal{B}} \left(-\frac{1}{\tau}\widetilde{\mathbf{Q}} + \dot{\widetilde{\mathbf{S}}}_e \right) : K - \widetilde{D}\widetilde{\mathbf{Q}}\boldsymbol{\Omega}\widetilde{X} : K \\ &\quad + \int_{\mathcal{B}} \boldsymbol{\Omega}\widetilde{\mathbf{Q}} : K - \widetilde{\mathbf{Q}}\boldsymbol{\Omega} : K \,. \end{aligned} \tag{4.8}$$

4.2 Finite element framework

We employ the finite element method to solve the weak form equations (4.4) with quartic quadrilateral C^0 elements. More specifically, the reference element $\tilde{E}$ is the square $[-1,1] \times [-1,1]$ with nodes $\tilde{p}_{kl},\ 1 \le k,l \le 5$, such that $\tilde{p}_{kl} = (\tilde{x}_k, \tilde{x}_l)$, where $\tilde{x}_1 = -1, \tilde{x}_2 = -.5, \tilde{x}_3 = 0, \tilde{x}_4 = .5, \tilde{x}_5 = 1$. Let the polynomials $\tilde{L}_k,\ 1 \le k \le 5$ be the unique quartic polynomials that are 1 at $\tilde{x}_m$, $m = k$, and 0 on $\tilde{x}_m$, $m \ne k$. Equivalently, $\tilde{L}_k(\tilde{x}_l) = \delta_{kl}$. We then define the shape functions on $\tilde{E}$ to be $\tilde{\psi}_{kl}(\tilde{x}^1, \tilde{x}^2) = \tilde{L}_k(\tilde{x}^1)\tilde{L}_l(\tilde{x}^2)$. Fig. 4.1 plots the reference element $\tilde{E}$ and one of its shape functions, $\psi_{2,3}$.

We cover our reference domain $\mathcal{B}$ with elements by mapping copies of the reference element to the r-θ plane and then applying the polar coordinate mapping $T(r,\theta)$. More precisely, we first choose the number of circumreferential elements e_c and the number of radial elements e_r. We define element E_{ij}, $1 \le i \le e_c$, $1 \le j \le e_r$, as the image of the reference element $\tilde{E}$ under the map $T \circ S_{ij}$, where S_{ij} is the linear scaling and shifting transformation

$$S_{ij}(\tilde{x}^1, \tilde{x}^2) = \left(r_1 + \frac{r_2 - r_1}{e_r}\left[\frac{\tilde{x}^1 + 1}{2} + j - 1\right], \frac{2\pi}{e_c}\left[\frac{\tilde{x}^2 + 1}{2} + i - 1\right] \right) , \tag{4.9}$$

and T is the polar coordinate transformation

$$T(r,\theta) = (r\cos\theta, r\sin\theta) \,. \tag{4.10}$$

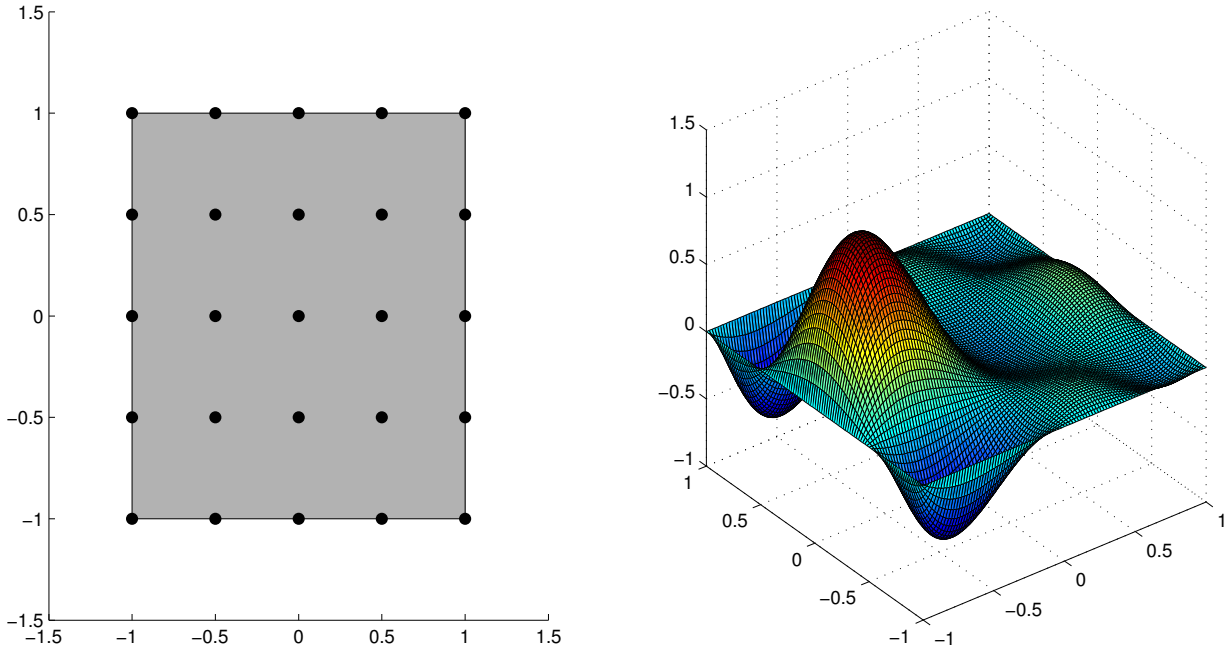

Figure 4.1: The reference element $\tilde{E}$ with nodes $\tilde{p}_{kl}$ is plotted on the left. The shape function $\tilde{\psi}_{2,3}$ is plotted on the domain $\tilde{E}$ on the right.

The images of the reference nodes $\tilde{p}_{ij}$ under these maps creates a grid of nodes p_{ij}, $1 \leq i \leq n_c$, $1 \leq j \leq n_r$ where $n_c = 4e_c$, $n_r = 4e_r + 1$. The location of the p_{ij} are given by

$$p_{ij} = T\left(r_1 + \frac{r_2 - r_1}{n_r - 1}(j-1), \frac{2\pi}{n_c}(i-1)\right). \tag{4.11}$$

We also consider the array of nodes p_{ij} as a single list which is denoted with a single index: p_k, $k = 1, \ldots, n_p$, where $n_p = n_c n_r$ is the total number of nodes. The list p_k is in lexicographic order in the indices i, j; the nodes on the hub are listed first and the nodes on the edge are listed last. Fig. 4.2 plots the maps S_{ij}, T, and the grid of nodes p_{ij}.

Next, we define the local shape functions on the E_{ij} as the push forward of the reference shape functions via the map $T \circ S_{ij}$. That is, $\psi_{ijkl} = \tilde{\psi}_{kl} \circ S_{ij}^{-1} \circ T^{-1}$. We define the global shape functions ψ_k corresponding to the nodes p_k as follows: ψ_k is the function which is zero outside any element not containing p_k and takes the value of the shape function corresponding to p_k within any element containing p_k. The ψ_k are well defined since it can be verified that local shape functions of adjacent elements corresponding to some node in the intersection agree everywhere on the intersection. However, the derivatives of these local shape functions do not agree on the intersection, hence the ψ_k are continuous, but have discontinuous derivatives. Since derivatives of the ψ_k are continuous within a given element, the weak derivative of ψ_k is square integrable.

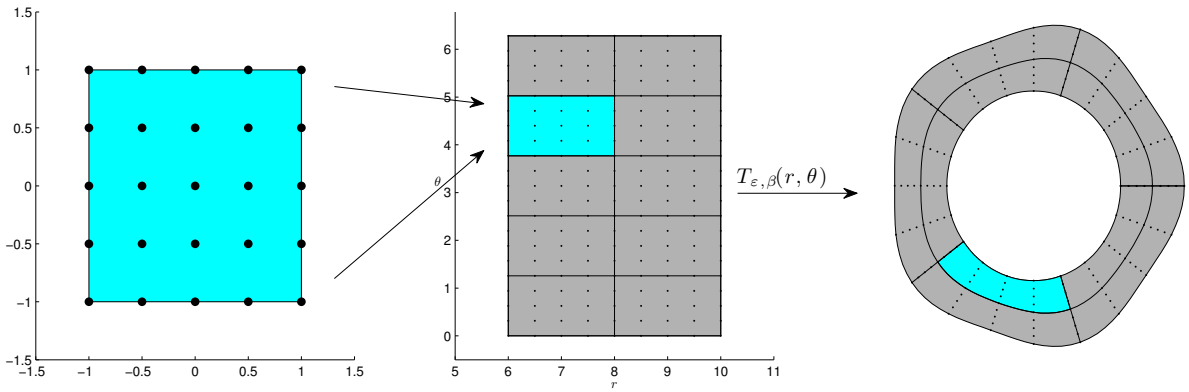

Figure 4.2: The reference element $\tilde{E}$ is mapped by $S_{4,1}$ to the r-θ plane. The grid of elements in the r-θ plane is then mapped by the polar coordinate transformation T onto the reference domain $\mathcal{B}_{.1,5}$. We also plot the grid of nodes p_{ij} in $\mathcal{B}_{.1,5}$.

We have described our finite element framework only for the smooth tire $\mathcal{B}$, but the treatment of the treaded tire $\mathcal{B}_{\varepsilon,\beta}$ is the same provided we replace the polar coordinate map T with $T_{\varepsilon,\beta}$.

Note that our finite element framework is not isoparametric. For example, the curved edges are the elements in Fig. 4.2 are not given by polynomial interpolation of the nodes. This has the advantage that it produces elements which exactly match our tire geometry for any values of e_c and e_r (i.e. isogeometric), without adding significant increase in computation. This approach is dependent on having a convenient description of the geometry, namely the maps T and $T_{\varepsilon,\beta}$.

4.3 The discretized equations

We use the finite element framework to numerically solve the displacement equations (4.4). First, we approximate our test function space $\mathbf{H}_{hub}$ with a finite dimensional space built up from our shape functions ψ_k. Let $\bar{H}$ be the span of $\{\psi_k \mathbf{e}_i\}$, where the $\mathbf{e}_i$ are the euclidean basis vectors of $\mathbb{R}^2$. $\bar{H}$ is a $2n_p$-dimensional subspace of H and any function in H can be approximated by a function in $\bar{H}$ as we refine our mesh. Let $\bar{H}_{hub}$ be $\bar{H} \cap H_{hub}$, i.e. the span of $\{\psi_k \mathbf{e}_i\}$ for ψ_k whose corresponding node p_k is not on the hub. There are $n_h = n_p - n_c$ such nodes, so $\bar{H}_{hub}$ has dimension $2n_h$ and its basis is given by $\{\psi_k \mathbf{e}_i | n_c < k \leq n_p\}$. For ease of notation, let $\psi'_k = \psi_{k+n_c}$, $1 \leq k \leq n_h$ so that we may write the basis of $\bar{H}_{hub}$ as $\{\psi'_k \mathbf{e}_i\}$.

We similarly define $\bar{H}_{\mathbb{S}}$ to be the span of $\{\psi_k \mathbf{E}_i\}$, where the $\mathbf{E}_i$, are the following basis for $\mathbb{S}$:

$$\mathbf{E}_1 = \begin{bmatrix} 1 & 0 \\ 0 & 0 \end{bmatrix}, \mathbf{E}_2 = \begin{bmatrix} 0 & 1 \\ 1 & 0 \end{bmatrix}, \mathbf{E}_3 = \begin{bmatrix} 0 & 0 \\ 0 & 1 \end{bmatrix}. \tag{4.12}$$

$\bar{H}_{\mathbb{S}}$ has dimension $3n_p$.

We approximate the space $\mathbf{H}_{hub} = H_{hub} \times H_{hub} \times H_{\mathbb{S}}$ by $\bar{\mathbf{H}}_{hub} \stackrel{\text{def}}{=} \bar{H}_{hub} \times \bar{H}_{hub} \times \bar{H}_{\mathbb{S}}$, a space of dimension $n_v = 2n_h + 2n_h + 3n_p$. Given a function $\mathbf{u} \in \bar{H}_{hub}$, we write $\bar{\mathbf{u}}$ for the coefficients of $\mathbf{u}$ expanded in terms of the basis $\{\psi'_k \mathbf{e}_i\}$. Similarly, we write $\bar{\mathbf{v}}$ and $\bar{\mathbf{Q}}$ for the coefficients corresponding to $\mathbf{v}$ and $\mathbf{Q}$, and write $\bar{\mathbf{z}} = (\bar{\mathbf{u}}, \bar{\mathbf{v}}, \bar{\mathbf{Q}})$.

We discretize the displacement equations (4.4) by searching for solutions in our discretized spaces and require the equations (4.4) to only hold for test functions (ζ, η, K) which are in $\bar{\mathbf{H}}$. This is equivalent to requiring the weak equations (4.4) to hold for the n_v basis functions of $\bar{\mathbf{H}}_{hub}$, $\{(\psi'_k \mathbf{e}_i, 0, 0)\} \cup \{(0, \psi'_k \mathbf{e}_i, 0)\} \cup \{(0, 0, \psi_k \mathbf{E}_i)\}$. The discretized displacement equations then become a n_v-dimensional system of differential equations in the unknowns $\bar{\mathbf{z}} = (\bar{\mathbf{u}}, \bar{\mathbf{v}}, \bar{\mathbf{Q}})$:

$$\begin{aligned} M'_2 \dot{\bar{\mathbf{u}}} &= \mathbf{f}^1(\bar{\mathbf{z}}) \\ M'_2 \dot{\bar{\mathbf{v}}} &= \mathbf{f}^2(\bar{\mathbf{z}}) \\ M_3 \dot{\bar{\mathbf{Q}}} &= \mathbf{f}^3(\bar{\mathbf{z}}) \,, \end{aligned} \tag{4.13}$$

where

$$\begin{aligned} \mathbf{f}^1_{(i-1)n_h+k} &= \int_{\mathcal{B}} \mathbf{v} \cdot \psi'_k \mathbf{e}_i, \ 1 \le k \le n_h, \ i = 1, 2 \\ \mathbf{f}^2_{(i-1)n_h+k} &= -\int_{\mathcal{B}} \mathbf{P} : D(\psi'_k \mathbf{e}_i) + \int_{\Gamma_e} \big(\mathbf{h} + \omega^2 \mathbf{R} X\big) \cdot \psi'_k \mathbf{e}_i, \ 1 \le k \le n_h, \ i = 1, 2 \\ \mathbf{f}^3_{(i-1)n_p+k} &= \int_{\mathcal{B}} \left(-\frac{1}{\tau} \mathbf{Q} + \dot{\mathbf{S}}_e \right) : \psi_k \mathbf{E}_i, \ 1 \le k \le n_p, \ i = 1, 2, 3 \,. \end{aligned} \tag{4.14}$$

Furthermore, M'_2 and M_3 are symmetric positive definite matrices related to the mass matrices M and M' for the shape functions ψ' and ψ'_k. They are defined as follows:

$$\begin{aligned} M_{ij} &= \int_{\mathcal{B}} \psi_i \psi_j, \ 1 \le i, j \le n_p \,, \qquad M'_{ij} = \int_{\mathcal{B}} \psi'_i \psi'_j, \ 1 \le i, j \le n_h \,, \\ M'_2 &= \begin{bmatrix} M' & 0 \\ 0 & M' \end{bmatrix}, \qquad M_3 = \begin{bmatrix} M & 0 & 0 \\ 0 & M & 0 \\ 0 & 0 & M \end{bmatrix}. \end{aligned} \tag{4.15}$$

We may similarly discretize the linearized equations and steady state solution equations. It can be verified that the discretization of the linearized equations is the same as the linearization of the discretized equations. The discretized linear equations are

$$\begin{aligned} M'_2 \dot{\hat{\bar{\mathbf{u}}}} &= \hat{\mathbf{f}}^1(\hat{\bar{\mathbf{z}}}) \\ M'_2 \dot{\hat{\bar{\mathbf{v}}}} &= \hat{\mathbf{f}}^2(\hat{\bar{\mathbf{z}}}) \\ M_3 \dot{\hat{\bar{\mathbf{Q}}}} &= \hat{\mathbf{f}}^3(\hat{\bar{\mathbf{z}}}) \,, \end{aligned} \tag{4.16}$$

where

$$
\begin{aligned}
\hat{\mathbf{f}}^1_{(i-1)n_h+k} &= \int_{\mathcal{B}} \hat{\mathbf{v}} \cdot \psi'_k \mathbf{e}_i, \ 1 \le k \le n_h, \ i = 1,2 \\
\hat{\mathbf{f}}^2_{(i-1)n_h+k} &= -\int_{\mathcal{B}} \hat{\mathbf{P}} : D(\psi'_k \mathbf{e}_i) + \int_{\Gamma_e} \left(\hat{\mathbf{h}} + \omega^2 \mathbf{R} X \right) \cdot \psi'_k \mathbf{e}_i, \ 1 \le k \le n_h, \ i = 1,2 \\
\hat{\mathbf{f}}^3_{(i-1)n_p+k} &= \int_{\mathcal{B}} \left(-\frac{1}{\tau} \hat{\mathbf{Q}} + \widehat{\dot{\mathbf{S}}_e} \right) : \psi_k \mathbf{E}_i, \ 1 \le k \le n_p, \ i = 1,2,3 \,.
\end{aligned}
\tag{4.17}
$$

Below, we compute the discretized steady state equations $\bar{\mathcal{S}}(\widetilde{\bar{\mathbf{z}}}) = \mathbf{0}$ and its linearization. For ease of notation, we drop the $\widetilde{\ }$ used to denote the transformed variables. The discretized steady state equations are:

$$
\begin{aligned}
\bar{\mathbf{0}} &= (M'_2)^{-1} \mathbf{g}^1(\bar{\mathbf{z}}) \\
\bar{\mathbf{0}} &= (M'_2)^{-1} \mathbf{g}^2(\bar{\mathbf{z}}) \\
\bar{\mathbf{0}} &= (M_3)^{-1} \mathbf{g}^3(\bar{\mathbf{z}}) \,,
\end{aligned}
\tag{4.18}
$$

where

$$
\begin{aligned}
\mathbf{g}^1_{(i-1)n_h+k} &= \int_{\mathcal{B}} (\mathbf{v} + \mathbf{\Omega} X - (D\mathbf{u} + \mathbf{I}) \mathbf{\Omega} X) \cdot \psi'_k \mathbf{e}_i, \ 1 \le k \le n_h, \ i = 1,2 \\
\mathbf{g}^2_{(i-1)n_h+k} &= -\int_{\mathcal{B}} \left[-\frac{1}{\rho_R} \mathbf{P} : D(\psi'_k \mathbf{e}_i) - (D\mathbf{v} + \mathbf{\Omega}) \mathbf{\Omega} X \cdot \eta \right] \\
&\quad + \int_{\Gamma_e} \mathbf{h} \cdot \psi'_k \mathbf{e}_i, \ 1 \le k \le n_h, \ i = 1,2 \\
\mathbf{g}^3_{(i-1)n_p+k} &= \int_{\mathcal{B}} \left(-\frac{1}{\tau} \mathbf{Q} + \dot{\mathbf{S}}_e \right) : \psi_k \mathbf{E}_i \\
&\quad + \int_{\mathcal{B}} (-D\mathbf{Q}\mathbf{\Omega} X + \mathbf{\Omega}\mathbf{Q} - \mathbf{Q}\mathbf{\Omega}) : \psi_k \mathbf{E}_i, \ 1 \le k \le n_p, \ i = 1,2,3 \,.
\end{aligned}
\tag{4.19}
$$

The linearization of $\bar{\mathcal{S}}(\bar{\mathbf{z}})$, denoted $\widehat{\bar{\mathcal{S}}}(\hat{\bar{\mathbf{z}}})$, is given by

$$
\begin{aligned}
&(M'_2)^{-1} \hat{\mathbf{g}}^1(\hat{\bar{\mathbf{z}}}) \\
&(M'_2)^{-1} \hat{\mathbf{g}}^2(\hat{\bar{\mathbf{z}}}) \\
&(M_3)^{-1} \hat{\mathbf{g}}^3(\hat{\bar{\mathbf{z}}}) \,,
\end{aligned}
\tag{4.20}
$$

where

$$
\begin{aligned}
\hat{\mathbf{g}}^1_{(i-1)n_h+k} &= \int_{\mathcal{B}} (\hat{\mathbf{v}} - D\hat{\mathbf{u}}\mathbf{\Omega}X) \cdot \psi'_k \mathbf{e}_i,\ 1 \le k \le n_h,\ i = 1,2 \\
\hat{\mathbf{g}}^2_{(i-1)n_h+k} &= -\int_{\mathcal{B}} \left[-\frac{1}{\rho_R} \widehat{\mathbf{P}} : D(\psi'_k \mathbf{e}_i) - D\hat{\mathbf{v}}\mathbf{\Omega}X \cdot \eta \right] \\
&\quad + \int_{\Gamma_e} \widehat{\mathbf{h}} \cdot \psi'_k \mathbf{e}_i,\ 1 \le k \le n_h,\ i = 1,2 \qquad (4.21) \\
\hat{\mathbf{g}}^3_{(i-1)n_p+k} &= \int_{\mathcal{B}} \left(-\frac{1}{\tau} \widehat{\mathbf{Q}} + \widehat{\dot{\mathbf{S}}}_e \right) : \psi_k \mathbf{E}_i \\
&\quad + \int_{\mathcal{B}} \left(-D\widehat{\mathbf{Q}}\mathbf{\Omega}X + \mathbf{\Omega}\widehat{\mathbf{Q}} - \widehat{\mathbf{Q}}\mathbf{\Omega} \right) : \psi_k \mathbf{E}_i,\ 1 \le k \le n_p,\ i = 1,2,3\,.
\end{aligned}
$$

We also write $\mathbf{M}\dot{\bar{\mathbf{z}}} = \bar{\mathbf{f}}(\bar{\mathbf{z}}), \mathbf{M}\dot{\hat{\bar{\mathbf{z}}}} = \hat{\bar{\mathbf{f}}}(\hat{\bar{\mathbf{z}}}), \mathbf{0} = \mathbf{M}^{-1}\bar{\mathbf{g}}(\bar{\mathbf{z}})$, and $\mathbf{0} = \mathbf{M}^{-1}\hat{\bar{\mathbf{g}}}(\hat{\bar{\mathbf{z}}})$ for the above equations, where $\bar{\mathbf{f}} = (\bar{\mathbf{f}}^1, \bar{\mathbf{f}}^2, \bar{\mathbf{f}}^3), \hat{\bar{\mathbf{f}}} = (\hat{\bar{\mathbf{f}}}^1, \hat{\bar{\mathbf{f}}}^2, \hat{\bar{\mathbf{f}}}^3), \bar{\mathbf{g}} = (\bar{\mathbf{g}}^1, \bar{\mathbf{g}}^2, \bar{\mathbf{g}}^3), \hat{\bar{\mathbf{g}}} = (\hat{\bar{\mathbf{g}}}^1, \hat{\bar{\mathbf{g}}}^2, \hat{\bar{\mathbf{g}}}^3)$, and $\mathbf{M} = \mathrm{diag}(M'_2, M'_2, M_3)$.

4.4 Numerical solution of the discretized equations

The discretized displacement equations (4.13) is a first order system of ODE and as such we can numerically integrate it using any number of ODE methods. We choose the 8th order explicit Runge-Kutta method of Dormand and Prince [16, 11]. In addition to being high order, this method has a larger stability region than lower order explicit Runge-Kutta methods, which is useful since we have found the evolution equations to be moderately stiff. When comparing its performance with Dormand and Prince's 5th order method [10] we find that the two methods require very similar computational effort to achieve stability, but that the higher order method is far more accurate.

To apply our Runge-Kutta method, we must be able to evaluate the integrals which occur in the definition of $\bar{\mathbf{f}}$. We numerically evaluate the integrals over the domain $\mathcal{B}$ using 10th order (i.e. five quadrature points in each direction) Gaussian quadrature over the reference element $\tilde{E}$. We also use quadrature to evaluate the matrices M and M'. These symmetric positive definite matrices are sparse due to the locality of the basis functions ψ_k and we invert them using the direct sparse solver CHOLMOD by Timothy Davis [9, 32, 8, 7, 6]. If M and M' are distributed over several processors due to domain decomposition, we invert them iteratively using Conjugate Gradients.

The linearized displacement equations (4.16) can be evolved using the same methods. We note that the linearized displacement equations depend on the solution to the displacement equations. Therefore, we either evolve the two equations at the same time or we evolve the displacement equations first, store the solution values, and interpolate them as needed by the linearized equations.

The discretized steady state equations (4.18) require us to find the zero of a system of n_v equations in n_v variables. We use Newton's method, which requires us to invert the Jacobian matrix of the system. The Jacobian matrix is given by the linear operator $\mathbf{M}^{-1}\hat{\bar{\mathbf{g}}}$, i.e. the composition of the inverse of the mass matrix $\mathbf{M}$ with the linear operator $\hat{\bar{\mathbf{g}}}$. $\hat{\bar{\mathbf{g}}}$ is respresented by a non-symmetric sparse matrix, which we invert using the direct sparse solver SuperLU [21].

Below we frequently refer to the linear operator $\mathbf{M}^{-1}\hat{\bar{\mathbf{g}}}$, which we denote $\mathcal{A}$. Recall that $\hat{\bar{\mathbf{g}}}$ is a linearization about some $\mathbf{z} \in \bar{\mathbf{H}}$. When it is necessary to emphasize this dependence, we write $\mathcal{A}[\mathbf{z}]$. If we are considering a purely elastic tire, we can ignore the $\widehat{\mathbf{Q}}$ variable and consider $\mathcal{A}$ as only a function of $(\hat{\boldsymbol{\phi}}, \hat{\boldsymbol{\nu}})$. In this case, we write $\mathcal{A}_e$.

4.5 Eigenvalues of the Steady State Problem

Given a steady state solution $\mathbf{z}$, the eigenvalues of the operator $\mathcal{A}[\mathbf{z}]$ yield useful information. For example, eigenvalues with positive real part indicate that the steady state solution is linearly unstable and eigenvalues that are purely imaginary indicate time periodic solutions of the linearized discretized equations.

We use the ARPACK software to compute selected eigenvalues of $\mathcal{A}[\mathbf{z}]$, which is suitable since $\mathcal{A}[\mathbf{z}]$ is the composition of two large sparse matrices and ARPACK requires only matrix-vector products. ARPACK is capable of finding eigenvalues according to many different criteria, such as largest real part or smallest magnitude. However, it performs best when searching for the largest magnitude eigenvalues. For our problem, ARPACK was unable to find eigenvalues of any criterion other than largest magnitude. Because we study the smallest magnitude eigenvalues of $\mathcal{A}[\mathbf{z}]$, we apply ARPACK to the inverse of $\mathcal{A}[\mathbf{z}]$. This requires sparse matrix solves, and as with solving the steady state problem with Newton's method, we use SuperLU.

We note that others have used a Newton type method [24, 14, 20] to solve the steady state problem with viscoelasticity. These works only apply Newton's method to the equations without viscoelasticity. A viscoelastic update is computed from the approximate solutions and the process is repeated until convergence. We apply Newton's method to the full viscoelastic system, $\mathbf{M}^{-1}\bar{\mathbf{g}}[\mathbf{z}]$. We gain superlinear convergence at the expense of solving linear systems over twice as large as the system of equations without viscoelasticity. This is an acceptable cost, since we need to form the full matrix $\mathcal{A}[\mathbf{z}]$ to solve the eigenvalue problem (described in the next section), which requires significantly more computational effort than solving the steady state problem.

4.6 Numerical computation of the operator $\mathcal{U}_T$

In order to search for time periodic solutions, we must numerically compute the functions $\mathcal{G}_T, \mathcal{F}_T$, and hence the operator $\mathcal{U}_T$. In the case of treaded tire, where the period T is fixed,

we choose the number of elements in the circumreferential direction, e_c, to be a multiple of β, the number of tread blocks, so that we can compute $\mathcal{U}_T$ by shifting the values of the nodes. Specifically, if after time T the tire has rotated over n tread blocks, we shift the values at the nodes $n\, e_c/\beta$ elements counterclockwise.

If such a choice of elements is not possible or if T is varying as may be the case with a smooth tire, Fourier series yield a numerical approximation to $\mathcal{U}_T$ with spectral accuracy. We denote this approximation $\bar{\mathcal{U}}_T$. We remark that for this section, $\widehat{\ }$ will be used to denote Fourier coefficients and not tangent directions.

Consider a 2π periodic function $f(\theta)$ with Fourier representation $f(\theta) = \sum_{-\infty}^{\infty} \hat{f}_k e^{\hat{\imath} k\theta}$. If $f(\theta)$ is shifted to the right by an angle θ_1, we then have

$$f(\theta - \theta_1) = \sum_{-\infty}^{\infty} (\hat{f}_k e^{-\hat{\imath} k\theta_1}) e^{\hat{\imath} k\theta}. \tag{4.22}$$

Hence, a shift by θ_1 can be computed by multiplying the kth Fourier coefficients by a factor of $e^{-\hat{\imath} k\theta_1}$. Next, we consider a function g defined on $\mathcal{B}$ written in polar coordinates $g(r,\theta)$ with Fourier representation $\sum_{-\infty}^{\infty} \hat{g}_k(r) e^{\hat{\imath} k\theta}$. The operator $\mathcal{U}_T$ shifts g by an angle of ωT, hence

$$\mathcal{U}_T(g) = \sum_{-\infty}^{\infty} (\hat{g}_k(r) e^{-\hat{\imath} k\omega T}) e^{\hat{\imath} k\theta}. \tag{4.23}$$

To approximate $\mathcal{U}_T(g)$ numerically, consider a function described by our finite element framework, $g = \sum_{k=1}^{n_p} g_k \psi_k$. If we consider the nodes and shape functions as arranged in a two-dimensional grid instead of a list, we can write $g = \sum_{i=1}^{n_c} \sum_{j=1}^{n_r} g_{ij} \psi_{ij}$. Holding j fixed, appy the discrete Fourier transform to the i index to obtain the Fourier coefficients $\hat{g}_{ij}$. As above, multiply the Fourier series by a factor of $e^{-\hat{\imath} i\omega T}$ to form $\hat{h}_{ij}$:

$$\hat{h}_{ij} \stackrel{\text{def}}{=} e^{-\hat{\imath} i\omega T} \hat{g}_{ij}\,. \tag{4.24}$$

We apply the inverse discrete Fourier transform on the i index of $\hat{h}_{ij}$ to obtain coefficients h_{ij}, and finally we set

$$\bar{\mathcal{U}}_T(g) = \sum_{i=1}^{n_c} \sum_{j=1}^{n_r} h_{ij} \psi_{ij}. \tag{4.25}$$

Lastly, we note that the time derivative of $\mathcal{U}_T(g(T))$ is needed to compute $\frac{d}{dT}\mathcal{G}_T$, where $g(X,T)$ is now a time-dependent function. As computed in flag3.2, $\frac{d}{dT}\mathcal{U}_T$ can be expressed as $\mathcal{U}_T(\frac{d}{dT}g - Dg\Omega X)$. Thus we could numerically approximate $\frac{d}{dT}\mathcal{U}_T$ by using the finite element framework to compute Dg and then appyling $\bar{\mathcal{U}}_T$ to $(\frac{d}{dT}g - Dg\Omega X)$. To be numerically consistent, however, we must instead compute $\frac{d}{dT}\bar{\mathcal{U}}_T(g(T))$, i.e. take the derivative with respect to time of the numerical procedure for computing $\mathcal{U}_T(g(T))$. Given $g(T) = \sum_{i=1}^{n_c} \sum_{j=1}^{n_r} g_{ij}(T)\psi_{ij}$ and its temporal derivative $g_T(T) = \sum_{i=1}^{n_c} \sum_{j=1}^{n_r} (g_{ij})_T(T)\psi_{ij}$, $\frac{d}{dT}\bar{\mathcal{U}}_T(g(T))$ can be computed as follows: Compute $\widehat{g_{ij}}(T)$ and $\widehat{(g_{ij})_T}(T)$ using the discrete Fourier transform. Form

$$\hat{f}_{ij}(T) \stackrel{\text{def}}{=} e^{-\hat{\imath} i\omega T} \widehat{(g_{ij})_T}(T) + (-\hat{\imath} i\omega) e^{-\hat{\imath} i\omega T} \widehat{g_{ij}}(T). \tag{4.26}$$

Apply the inverse discrete Fourier transform to $\hat{f}_{ij}(T)$ to obtain coefficients $f_{ij}(T)$. We then have

$$\frac{d}{dT}\bar{\mathcal{U}}_T(g(T)) = \sum_{i=1}^{n_c}\sum_{j=1}^{n_r} f_{ij}(T)\psi_{ijf}\,. \tag{4.27}$$

4.7 Solving the time periodic equations

In the following two sections, we present two different methods to find time periodic solutions: minimizing $\mathcal{G}_T(\mathbf{z}_0)$ using the Levenberg-Marquardt algorithm and solving $\mathcal{F}_T(\mathbf{z}_0) = \mathbf{0}$ using a Newton-Krylov method.

Minimization of the time periodic functional $\mathcal{G}_T$

Once we numerically solve the evolution equations and compute the operator $\bar{\mathcal{U}}_T$, we can numerically compute the function $\mathcal{G}_T(\mathbf{z}_0)$ for $\mathbf{z}_0$ in $\bar{\mathbf{H}}_{hub}$. We denote the discrete version of $\mathcal{G}_T$ as $\bar{\mathcal{G}}_T$:

$$\bar{\mathcal{G}}_T(\bar{\mathbf{z}}_0) = \frac{1}{2}\int_{\mathcal{B}} \|\bar{\mathcal{U}}_T\boldsymbol{\phi}(T) - \boldsymbol{\phi}_0\|^2 + \|\bar{\mathcal{U}}_T\boldsymbol{\nu}(T) - \boldsymbol{\nu}_0\|^2 + \|\mathbf{R}\bar{\mathcal{U}}_T\mathbf{Q}(T)\mathbf{R}^\mathsf{T} - \mathbf{Q}_0\|^2\,, \tag{4.28}$$

where $(\mathbf{u}, \mathbf{v}, \mathbf{Q}) \in \bar{\mathbf{H}}_{hub}$ have an initial condition given by the coefficients $\bar{\mathbf{z}}_0$, $(\mathbf{u}, \mathbf{v}, \mathbf{Q})$ evolve according to the discretized evolution equations, and the integrals are computed with Gaussian quadrature. Also, the norms are the same as in §3.1; i.e. they are nondimensionalized by constants u_{char}, v_{char} and Q_{char}. These constants are chosen so that the three terms of $\bar{\mathcal{G}}_T$ are of the same order for our problems of interest.

We minimize $\bar{\mathcal{G}}_T$ to find time periodic solutions using the Levenberg-Marquardt algorithm. We choose this minimization algorithm because we were unable to find minima of $\bar{\mathcal{G}}_T$ using algorithms that only require the derivative of $\bar{\mathcal{G}}_T$, such as BFGS algorithms or nonlinear conjugate gradient.

In order to apply Levenberg-Marquardt, we write $\bar{\mathcal{G}}_T$ as a sum of squares. We define the scalar functions $\mathbf{r}_i$, $i = 1, \ldots, 7$:

$$\begin{aligned}
\mathbf{r}_1 &= (\bar{\mathcal{U}}_T\boldsymbol{\phi}(T) - \boldsymbol{\phi}_0)\cdot\mathbf{e}^1\\
\mathbf{r}_2 &= (\bar{\mathcal{U}}_T\boldsymbol{\phi}(T) - \boldsymbol{\phi}_0)\cdot\mathbf{e}^2\\
\mathbf{r}_3 &= (\bar{\mathcal{U}}_T\boldsymbol{\nu}(T) - \boldsymbol{\nu}_0)\cdot\mathbf{e}^1\\
\mathbf{r}_4 &= (\bar{\mathcal{U}}_T\boldsymbol{\nu}(T) - \boldsymbol{\nu}_0)\cdot\mathbf{e}^2\\
\mathbf{r}_5 &= (\mathbf{R}\bar{\mathcal{U}}_T\mathbf{Q}(T)\mathbf{R}^\mathsf{T} - \mathbf{Q}_0) : \mathbf{E}^1\\
\mathbf{r}_6 &= \sqrt{2}(\mathbf{R}\bar{\mathcal{U}}_T\mathbf{Q}(T)\mathbf{R}^\mathsf{T} - \mathbf{Q}_0) : \mathbf{E}^2\\
\mathbf{r}_7 &= (\mathbf{R}\bar{\mathcal{U}}_T\mathbf{Q}(T)\mathbf{R}^\mathsf{T} - \mathbf{Q}_0) : \mathbf{E}^3\,.
\end{aligned} \tag{4.29}$$

Using the $\mathbf{r}_i$, $\bar{\mathcal{G}}_T$ is expressed as an integral over a sum of squaures:

$$\bar{\mathcal{G}}_T = \int_{\mathcal{B}} \sum_{i=1}^{7} \mathbf{r}_i^2 \,. \tag{4.30}$$

The integral above is evaluated using Gaussian quadrature over $n_g = 25 e_c e_r$ quadrature points q_j with weights w_j, $j = 1, \ldots, n_g$. Writing r_{ij} for $w_j \mathbf{r}_i$ evaluated at q_j, yields $\bar{\mathcal{G}}_T$ as a sum of squares:

$$\bar{\mathcal{G}}_T = \sum_{j=1}^{n_g} \sum_{i=1}^{7} r_{ij}^2 = \sum_{k=1}^{7 n_g} r_k^2 \,, \tag{4.31}$$

where the r_k are the r_{ij} arranged as a single list.

To implement Levenberg-Marquardt, we must be able to compute the Jacobian matrix $\mathbf{J}$ of the r_k. We compute the derivative of the $\mathbf{r}_i$ in the direction of a tangent $\hat{\mathbf{z}}_0$:

$$\begin{aligned}
\hat{\mathbf{r}}_1 &= (\bar{\mathcal{U}}_T \hat{\boldsymbol{\phi}}(T) - \hat{\boldsymbol{\phi}}_0) \cdot \mathbf{e}^1 \\
\hat{\mathbf{r}}_2 &= (\bar{\mathcal{U}}_T \hat{\boldsymbol{\phi}}(T) - \hat{\boldsymbol{\phi}}_0) \cdot \mathbf{e}^2 \\
\hat{\mathbf{r}}_3 &= (\bar{\mathcal{U}}_T \hat{\boldsymbol{\nu}}(T) - \hat{\boldsymbol{\nu}}_0) \cdot \mathbf{e}^1 \\
\hat{\mathbf{r}}_4 &= (\bar{\mathcal{U}}_T \hat{\boldsymbol{\nu}}(T) - \hat{\boldsymbol{\nu}}_0) \cdot \mathbf{e}^2 \\
\hat{\mathbf{r}}_5 &= (\mathbf{R} \bar{\mathcal{U}}_T \widehat{\mathbf{Q}}(T) \mathbf{R}^{\mathsf{T}} - \widehat{\mathbf{Q}}_0) : \mathbf{E}^1 \\
\hat{\mathbf{r}}_6 &= \sqrt{2} (\mathbf{R} \bar{\mathcal{U}}_T \widehat{\mathbf{Q}}(T) \mathbf{R}^{\mathsf{T}} - \widehat{\mathbf{Q}}_0) : \mathbf{E}^2 \\
\hat{\mathbf{r}}_7 &= (\mathbf{R} \bar{\mathcal{U}}_T \widehat{\mathbf{Q}}(T) \mathbf{R}^{\mathsf{T}} - \widehat{\mathbf{Q}}_0) : \mathbf{E}^3 \,,
\end{aligned} \tag{4.32}$$

where $(\hat{\boldsymbol{\phi}}, \hat{\boldsymbol{\nu}}, \widehat{\mathbf{Q}}) \in \bar{\mathbf{H}}_{hub}$ have initial condition given by $\hat{\mathbf{z}}_0$ and evolve according to the discretized linearized equations. We compute the $\hat{r}_k$ from the $\hat{\mathbf{r}}_i$ in the same manner we obtained the r_k from the $\mathbf{r}_i$. The Jacobian matrix $\mathbf{J}$ is then given by setting $\hat{\mathbf{z}}_0$ to be the lth basis function of $\bar{\mathbf{H}}_{hub}$, computing the corresponding $\hat{r}_k$, and letting $\mathbf{J}_{kl} = \hat{r}_k$.

Once we have calculated $\mathbf{J}$, our implementation of the Levenberg-Marquardt algorithm requires the SVD decomposition of $\mathbf{J}$, which we solve using LAPACK or SCALAPACK.

Newton-Krylov solution to $\mathcal{F}_T = \mathbf{0}$

The same techniques used to compute $\bar{\mathcal{G}}_T$ also allow us to compute $\bar{\mathcal{F}}_T$, the discrete version of $\mathcal{F}_T$ and to compute $\widehat{\bar{\mathcal{F}}}_T$, the discrete version of the derivative of $\widehat{\mathcal{F}}_T$. Namely, we evolve the discretized or linear discretized equations and apply the operator $\bar{\mathcal{U}}_T$. To solve $\bar{\mathcal{F}}_T = \mathbf{0}$, which is a large system of equations, we apply Newton's method. The iterative solver GMRES allows us to invert the Jacobian of $\bar{\mathcal{F}}_T$ by calculating only matrix-vector products; namely $\widehat{\bar{\mathcal{F}}}_T$. This requires first computing a solution $\mathbf{z}(X, t)$ to the equations (2.47) and then evolving the linearized equations (2.52) about $\mathbf{z}$ for multiple initial conditions $\hat{\mathbf{z}}_0$. Since the values of $\mathbf{z}(X, t)$ are needed to evolve the linearized equations, the values of $\mathbf{z}(X, t)$ are stored for all time steps and interpolated (to 8th order, [16]) as needed by the Runge-Kutta time stepper for the linearized equations.

4.8 Parallelization

There are many opportunities for parallelization in the numerical algorithms described above. For the steady state and eigenvalue problems, the main computational cost is performing matrix-vector solves for the large sparse matrix $\mathcal{A}$. We achieve some speedup by using the SuperLU_Dist version of SuperLU. Since we are not memory limited, we use the SuperLU_Dist routines that depend on $\mathcal{A}$ being stored on each processor.

The computation of $\mathbf{J}$ and its SVD decomposition are the most expensive aspects of minimizing the time periodic functional $\bar{\mathcal{G}}$. The computation of $\mathbf{J}$ requires evolving n_v solutions of the linearized displacement equations. However, the n_v solutions can be evolved completely independent of each other, leading to an embarassingly parallel problem, for which we achieved nearly perfect speedup. We also achieved very good speedup by calculating the SVD of $\mathbf{J}$ with ScaLAPACK.

The computational bottleneck for the Newton-Krylov method is evolving the linear equations (4.16) needed for the matrix-vector products in the inner loop of GMRES. We parallelize this by finite element domain decomposition.

Chapter 5

Results

5.1 Choice of units and constants

Our choice of units is Newtons (N), megagrams (Mg), and seconds (s). This choice implies our unit for length is milimeters (mm).

In the remainder of the results section, we use the following values for constants, unless otherwise noted. The tire has inner radius $r_1 = 240$mm and outer radius $r_2 = 400$mm. The density of the tire is $\rho = 1 \times 10^{-9}$ Mg/mm^3. The bulk modulus κ and shear modulus μ are 689 N/mm^2 and 6.89 N/mm^2, respectively. The dimensionless viscosity parameter ν has value 1 and the relaxation time is .01 seconds. The distance from the axis to the road, h, is 380 mm and the road strength parameter δ is 1000 N/mm^2. The tire tread thickness parameter ε is 0.1.

We must also define the road force function $\gamma(x)$, which must be monotonically increasing for $x > 0$ and satisfy $\gamma(x) = 0$ for $x \leq 0$. A simple choice would be

$$\begin{cases} \gamma(x) = 0, & x \leq 0 \\ \gamma(x) = x, & x \geq 0\,. \end{cases} \tag{5.1}$$

However, this choice of γ is not smooth and leads to non-smooth discretized equations. Instead we choose the smooth function

$$\begin{cases} \gamma(x) = 0, & x \leq 0 \\ \gamma(x) = \exp(x - x^{-1}), & x \geq 0\,. \end{cases} \tag{5.2}$$

This function has the drawback of converging to zero exponentially fast as $x \to 0$ from the right, resulting in an extremeley weak road for small road penetration.

5.2 Example computation of a time periodic solution

We describe a typical computation of a time periodic solution of a treaded tire for both the Levenberg-Marquardt algorithm and for the Newton-Krylov method.

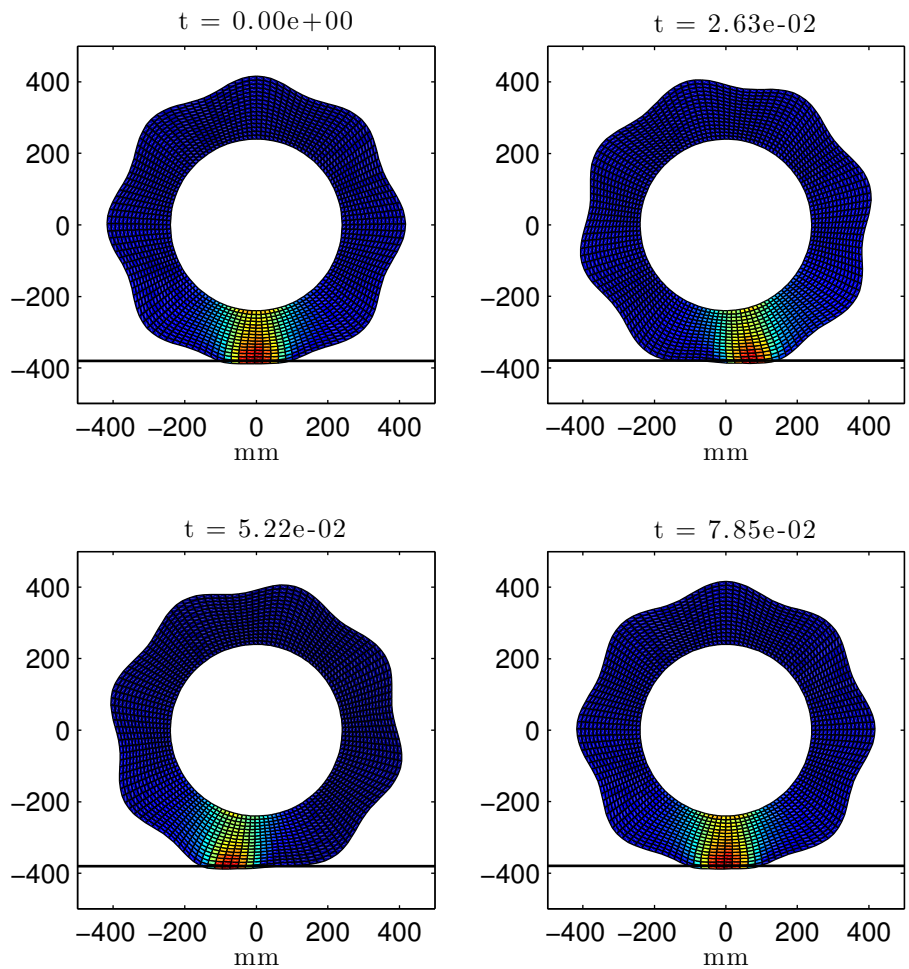

Figure 5.1: Plot of the tire as it rotates counterclockwise from one tread to the next. Red indicates high first principal stress while blue indicates low first principal stress.

The Levenberg-Marquardt algorithm

We choose mesh size $e_c = 16$, $e_r = 2$ and the tire has $\beta = 8$ treads and is rolling with frequency $\omega = 100$ Hertz. The tire is rotated such that each tread lines up with its neighbor, which implies $T = 2\pi/(\beta\omega)$.

We take 2000 time steps to compute the evolution of the tire as well as the computation of the Jacobian matrix. This number is chosen to be big enough so that the time stepping remains stable. We have found that with our 8th order method, a number of time steps that ensures stability is also large enough so that the time stepping has converged.

The road strenth parameter δ is incrementally increased from 0. We use quadratic Lagrangian interpolation to predict the initial condition for each increment based on the previous ones.

For each increment of δ, we apply the Levenberg-Marquardt minimization to find the time periodic solution. Levenberg-Marquardt decreases the objective function $\bar{\mathcal{G}}_T$ approximately by a factor of 10^{25} and we observe superlinear convergence.

The δ increment size is variable and depends on the number of Levenberg-Marquardt Jacobian computations required to find a minimium. We increase the δ increment if only one Jacobian computation is required and decrease it if more than 2 Jacobian computations are required. The computation of the Jacobian dominates the calculation and requires 45 minutes for each Jacobian computation using 48 processors. The number of δ increments is typically 40, requiring a total of 22.5 hours.

The Newton-Krylov algorithm

We choose mesh size $e_c = 32$, $e_r = 4$ (see Fig. 5.1), $\omega = 10$ Hertz, and we take 10000 time steps to evolve the weak equations and linearized weak equations. We first perform a true steady state calculation to determine the deformation of the tire at rest on the road. This is used as an initial guess for Newton's method, which then solves $\bar{\mathcal{F}}_T = \mathbf{0}$ to approximately 8 digits of accuracy. Within each Newton iteration, GMRES performs linear solves on the Jacobian of $\bar{\mathcal{F}}_T$. Setting the tolerance on the GMRES residual to 1×10^{-3} is sufficient for Newton's method to perform well and obtain superlinear convergence. A typical number of GMRES iterations for this tolerance is 12 and a typical number of Newton iterations is 5.

The GMRES algorithm dominates the computation and each iteration requires approximately 15 minutes on 32 processors, hence the entire simulation requires approximately $15 \times 5 \times 12$ minutes $= 15$ hours.

It is also possible to incrementally increase the road strength, rotation speed, or tread amplitude until the desired values are reached as we did with the Levenberg-Marquardt algorithm, but we find this unnecessary in the above computation.

Comparison of the two methods

The main advantage of the Newton-Krylov method is that it scales very well. We are not required to form any matrices since the GMRES algorithm only requires matrix-vector products. In contrast, the Levenberg-Marquardt method bottleneck is forming and storing the dense matrix $\mathbf{J}$, which has size $n_v \times n_g$. This makes it an order n_v^2 algorithm, whereas the Newton-Krylov method is order n_v. Furthermore, computing the SVD of $\mathbf{J}$ is an order n_v^3 operation, which would eventually become the bottleneck of the Levenberg-Marquardtz algorithm if the mesh size is increased and the number of time steps is held fixed. For this reason, we are able to compute time periodic solutions for larger mesh sizes with the Newton-Kyrlov method than the Levenberg-Marquardt method.

However, the Newton-Krylov method is more sensitive to the relaxation time of the problem. The larger τ is, the more iterations GMRES requires to converge. The Levenberg-Marquardt algorithm does not display this sensitivity, which is perhaps due to its access of the entire Jacobian matrix instead of only several matrix-vector products.

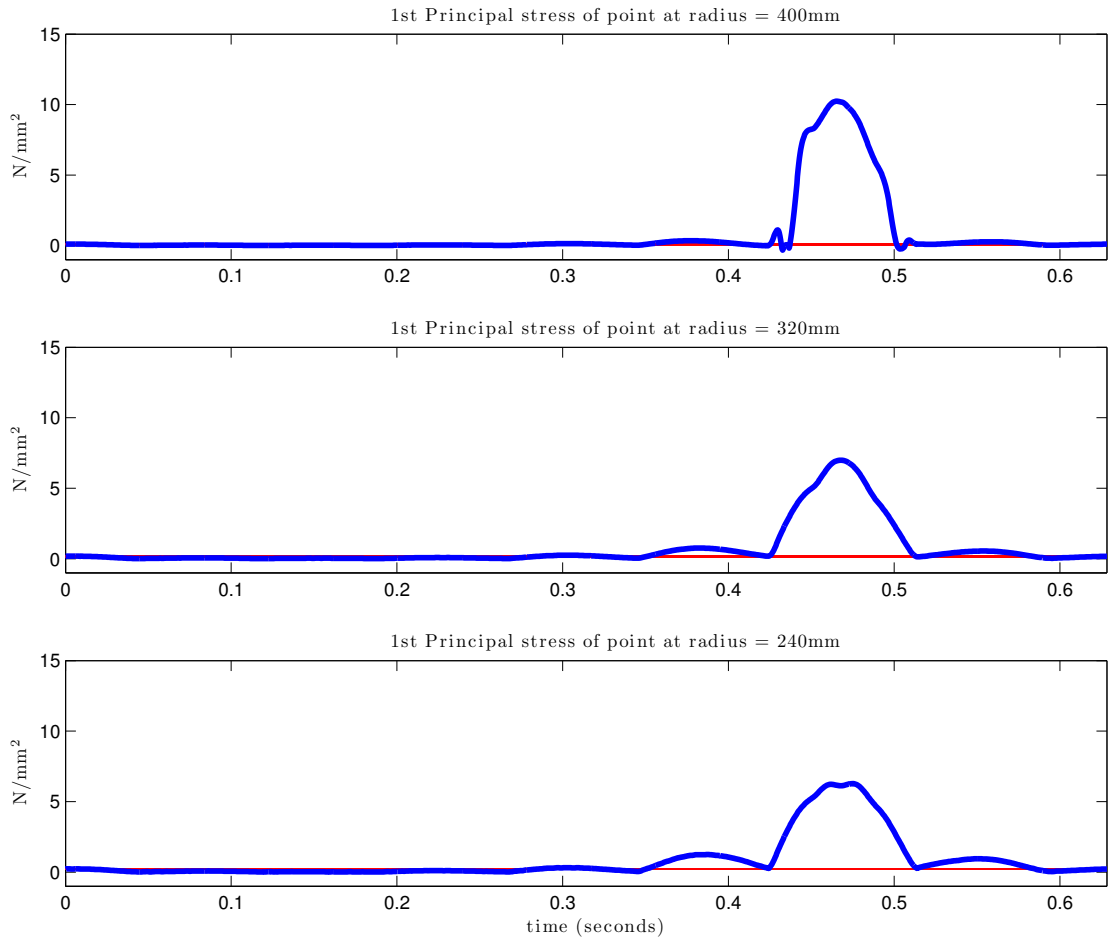

Figure 5.2: Plots of the evolution of the first principal stress over one revolution. The plots represent points at different distances from the hub, from furthest to closest.

5.3 Time evolution of stress of the treaded tire

Given a time periodic solution for the treaded tire computed by the methods above, we evaluate the first principal stress at various locations on the tire. We note some of the features of the stress caused by the presence of the treads, which could not be captured by a steady rolling computation. For these examples, we use the time periodic solution computed by the Newton-Krylov method as described in §5.2.

Fig. 5.1 shows the principal stress of the entire tire at various points in time, while Fig. 5.2 shows first first principal stresses at a material point as it makes one full revolution around the tire. At time $t = 0$, the material point begins on the positive x^1-axis. The first principal stress spikes as the material point nears contact with the road. The first principal stress is largest at the outer boundary of the tire where contact with the road is made. We note that the double peak in the first principal stress for a material point on the hub occurs

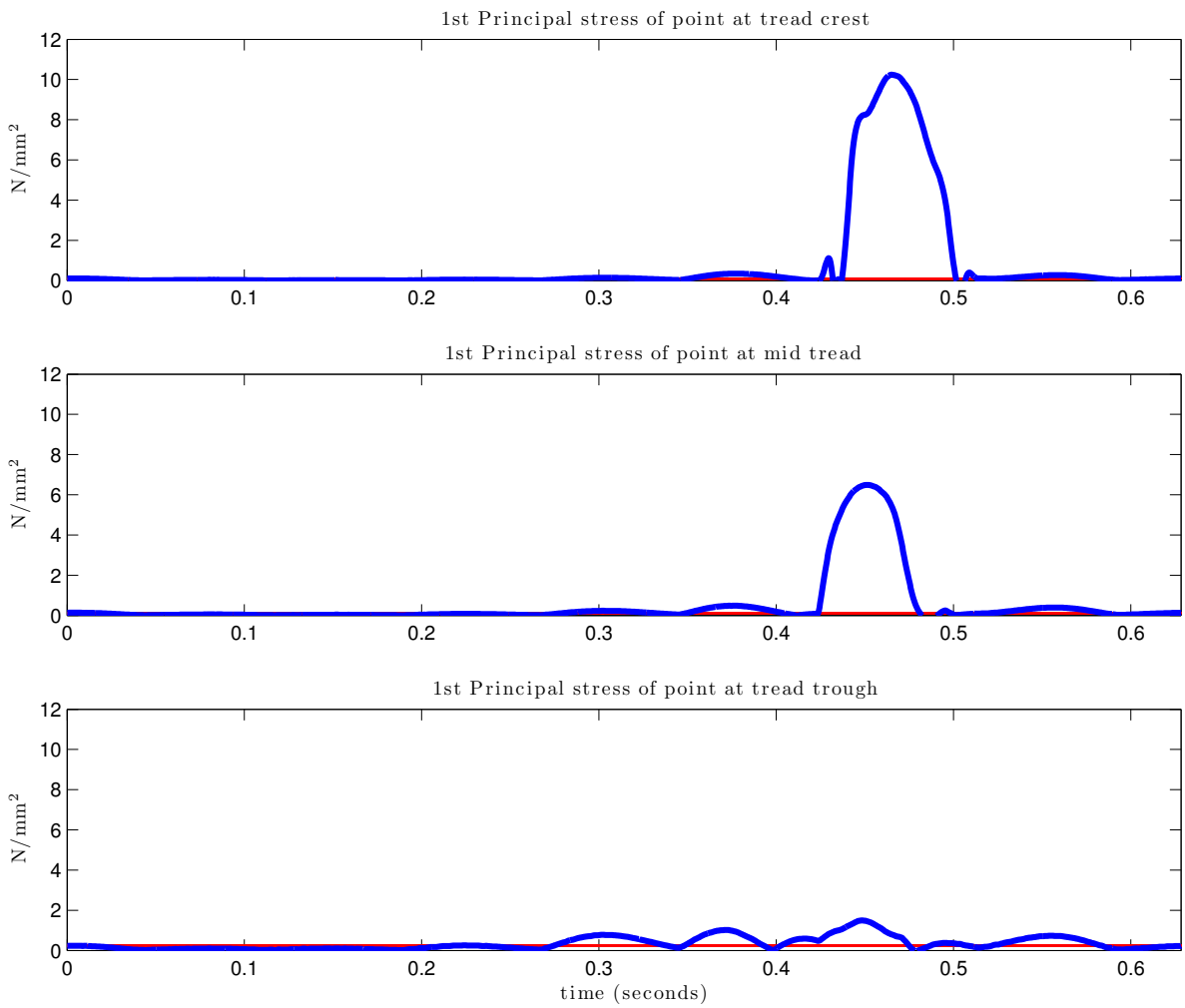

Figure 5.3: Plots of the evolution of the first principal stress over one revolution. The plots represent points at different locations along the edge of the tire. The top plot is at a tread peak, the bottom plot is at a tread trough, and the third plot is midway between.

because of high shear stresses on either side of the portion of the hub closest to the road.

Fig. 5.3 quantifes the difference in stresses at different points along a tread. The first principal stress decreases as we move from the tread crest to the tread trough. We note that the first principal stress along the tread trough has small increases during the time that adjascent tread troughs are coming in contact with the road (approximately during milliseconds 4-5 and 6-7 in the bottom plot in Fig. 5.3). This is caused by the tread trough being squeezed by the adjacent treads due to its concave geometry.

We plot the traction experienced by a material point along the edge as it rotates with the tire in Fig. 5.4. Since the traction is defined to be a vector pointing in the upward direction, we only plot the magnitude. As expected, the traction is largest at the tread peak and smallest at the tread trough.

In Fig. 5.5 we observe the shear stress along the hub of the tire, specifically $\mathbf{PN} \cdot \mathbf{t}$, where $\mathbf{N}$ is the outward normal along the hub and $\mathbf{t}$ is the tangent vector to the hub pointing in the counterclockwise direction. This figure indicates that the largest shear stresses on the hub occur radially in line with the tread troughs.

5.4 A rotating viscoelastic oval

We present an example where the numerical method for finding time periodic solutions can capture the natural oscillations of a viscoelastic body. This demonstrates that the time periodic framework accurately captures motions that would not be present in any steady state calculation.

We consider a rotating oval-shaped body, which is modeled in the tire framework by setting $\beta = 2, \varepsilon = 0.4$. The oval is spun at 20 Hertz and collides with the road, which we expect to excite the fundamental of oscillation. By computing the smallest eigenvalue and corresponding eigenvector of the oval when stationary, we observe the fundamental mode (see Fig. 5.6) which has a period of oscillation approximately 1.7×10^{-2} seconds.

We compute a time periodic solution for a half revolution of the oval, which has a period of approximately 0.15 seconds and hence ample time to observe oscillations of the fundamental mode. The computed time periodic solution shows that the fundamental mode is excited as the oval contacts the road. In Fig. 5.7 we see good agreement between the angular displacement of the computed time periodic solution of the oval and the oscillations predicted by the fundamental mode analysis.

5.5 Example computation of steady state solutions and eigenvalues

We turn our attention from time periodic solutions of treaded tires to steady state computations of smooth tires, which requres Newton's method to solve the nonlinear equations (4.18). For a typical computation of a steady state solution for the smooth tire, we choose

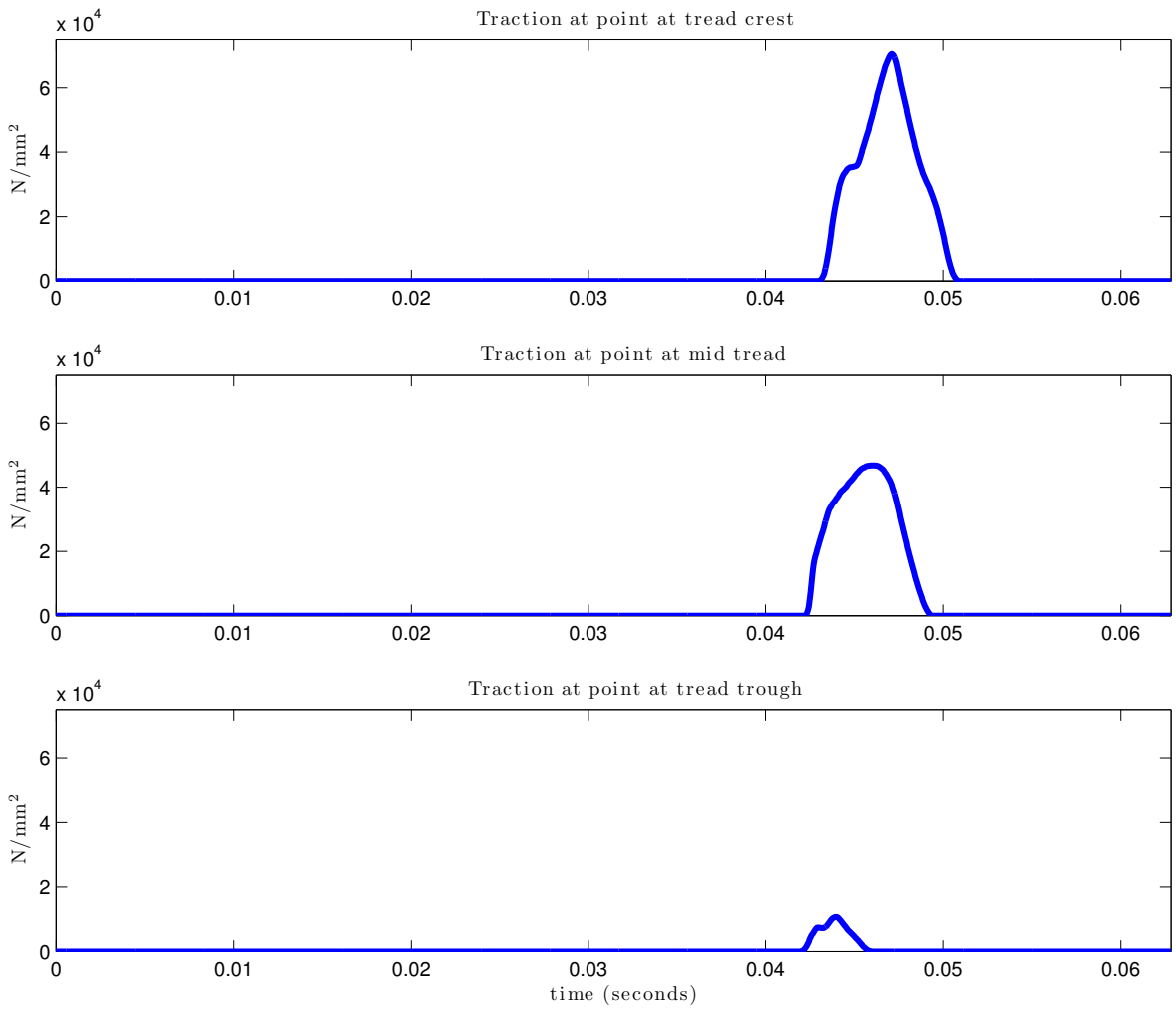

Figure 5.4: Plots of traction over one tire revolution. The plots represent points at different locations along the edge of the tire. The top plot is at a tread peak, the bottom plot is at a tread trough, and the middle plot is midway between.

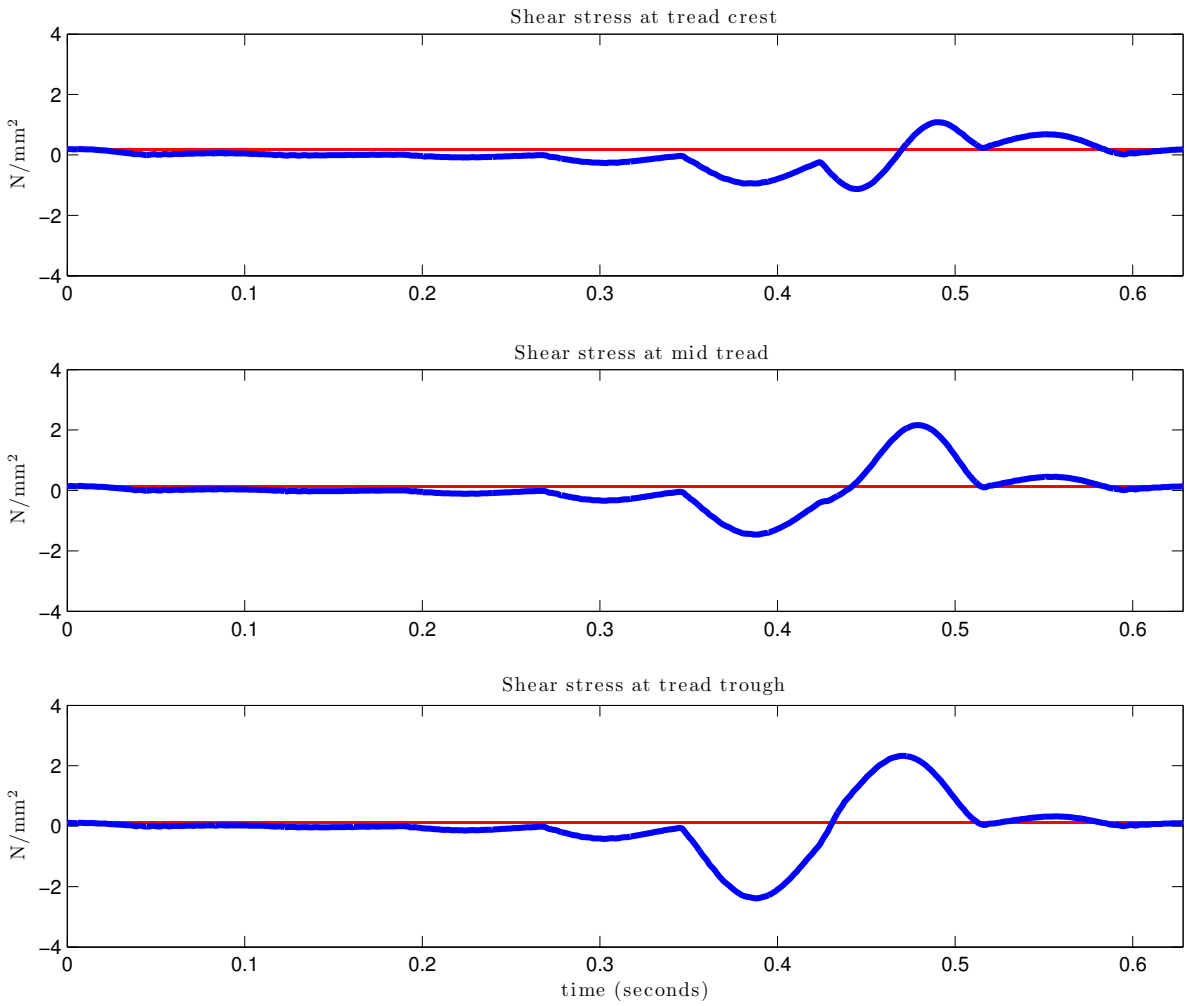

Figure 5.5: Plots of shear stresses of material points along the hub over one tire revolution. The plots represent points at different locations along the hub of the tire. The top plot is radially in line with a tread peak, the bottom plot with a tread trough, and the middle plot is midway between.

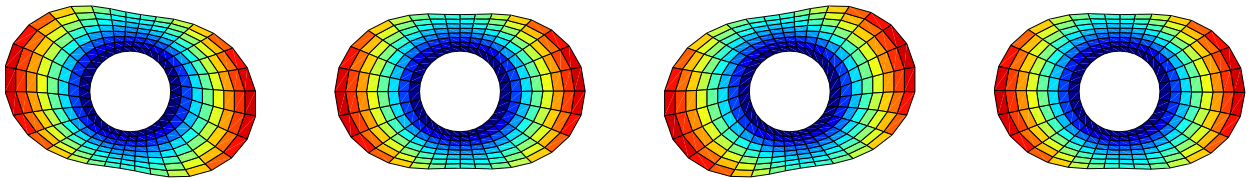

Figure 5.6: Plots of a simple oscillating mode of the oval over one period.

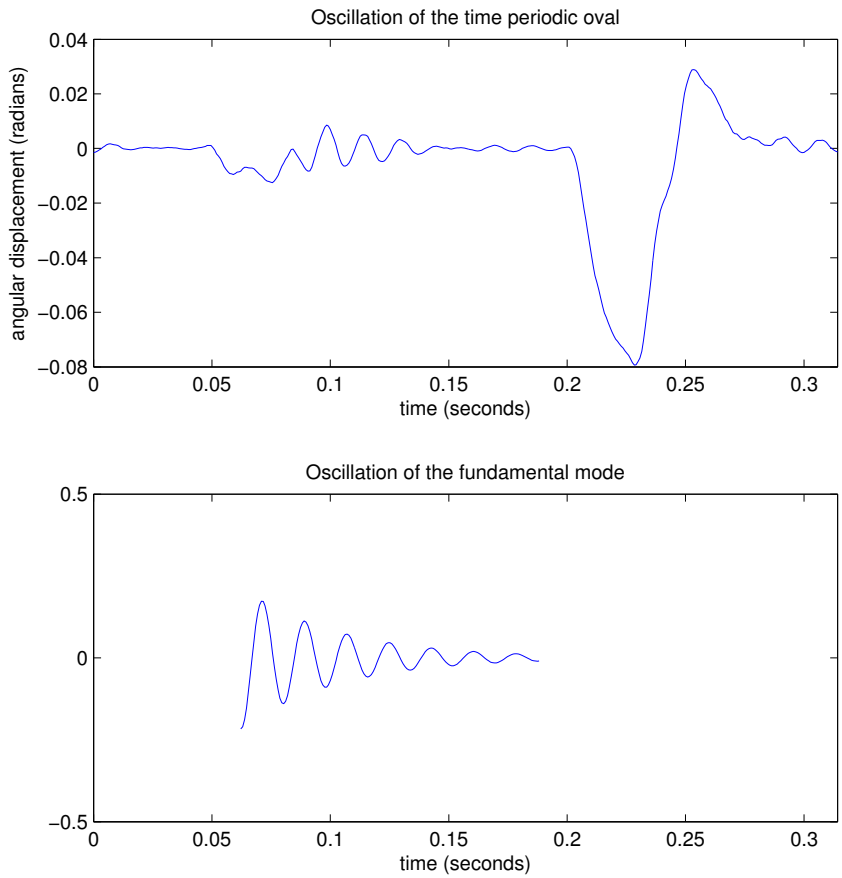

Figure 5.7: The top plot is angular displacement of the right-most tip of the oval over a full revolution of the oval. The oscillation near $0.05 - 0.15$ seconds corresponds to the opposite end (left-most tip) of the oval contacting the road. The large displacement near $0.2 - 0.27$ seconds corresponds to the right-most tip itself contacting the road. The bottom plot displays $\mathrm{Re}\,(e^{\lambda t})$, where λ is the eigenvalue corresponding to the fundamental mode. The similar frequency and rate of decay of the two plots near 0.1 seconds indicate the excitation of the fundamental mode is captured in the top plot.

mesh size $e_c = 64, e_r = 8$. Newton's method typically requires no more than 5 iterations to decrease the norm between successive iterations by a factor of 10^{12}. Often we compute a sequence of steady state solutions by varying ω and using the Lagrangian interpolation method described in §5.2. In this case, usually only a single iteration of Newton's method is required after the first few steps in the sequence. The computation bottleneck of this method is performing sparse linear solves on the 58112×58112 matrix $\mathcal{A}$ once per Newton iteration. The solve for the first Newton iteration requires about 15 seconds on 4 processors and solves for subsequent Newton iterations require about 8 seconds, since we may reuse the row permutation used for the first solve.

Once we have computed a steady state solution, we may apply the ARPACK software to compute the smallest eigenvalues of $\mathcal{A}$. ARPACK requires the user to choose the number of eigenvalues to compute and to choose the size of the Krylov subspace used to search for the eigenvalues. These choices can affect whether the ARPACK algorithm converges and how quickly. We find that searching for 80 eigenvalues with a Krylov subspace dimension of 300 was most efficient, requiring approximately 460 sparse matrix solves. However, since the matrix only needs to be factored once, each solve only takes 0.4 seconds. Thus the total ARPACK algorithm completes in 184 seconds with 4 processors.

5.6 Bifurcations of the free spinning tire

Elastic case

Oden and Lin [24] discovered that for a free spinning elastic tire, the steady state solution bifucates as the tire speed is increased. Given any tire speed ω, they found a radially symmetric solution $\mathbf{z}_\omega$ of the steady state problem. They provided evidence that below a critical speed ω_c, $\mathbf{z}_\omega$ is the only solution to the steady state problem but for $\omega > \omega_c$ the radially symmetric solution $\mathbf{z}_\omega$ may bifurcate at speeds ω_i, $i = 1, 2, 3, \ldots$ to a steady state solution with i standing waves. As ω increases, the number of standing waves on the stationary solutions decreases until a bifurcation into a two-peak or even one-peak solution is found. The bifurcation points correspond to the Jacobian matrix of the steady state solution problem (4.18) about $\mathbf{z}_\omega$, $\mathcal{A}_e[\mathbf{z}_\omega]$, becoming singular.

We observe the same phenomenon with our tire simulation, and in addition to observing the singularity of $\mathcal{A}_e[\mathbf{z}_\omega]$ for certain values of ω, we follow eigenvalues of $\mathcal{A}_e[\mathbf{z}_\omega]$ as they approach zero. In Fig. 5.8 we plot the smallest eigenvalues of the operator $\mathcal{A}_e[\mathbf{z}_\omega]$ as ω varies. When $\omega < \omega_c$, the eigenvalues are all purely imaginary. This is explained by the Hamiltonian nature of the free spinning elastic tire described in §3.4. The operator $\mathcal{A}_e$ is equal to the Jacobian of $\bar{\mathcal{S}}_H$, so we may apply the result that if $D^2\bar{\mathcal{H}}$ is positive definite then the eigenvalues of $\mathcal{A}_e$ are purely imaginary. When $\omega = 0$, the axisymmetric solution is the identity configuration and we directly compute that $D^2\bar{\mathcal{H}}$ is positive definite. As we increase ω to ω_c, we numerically observe that $D^2\bar{\mathcal{H}} = \mathcal{J}^{-1}\mathcal{A}_e$ remains non-singular, hence positive definite. Thus we expect that the eigenvalues of $\mathcal{A}_e$ are purely imaginary, which our

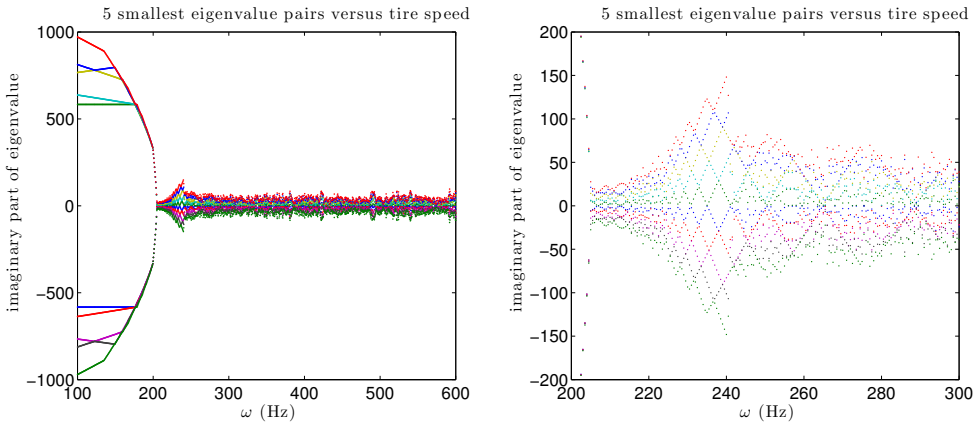

Figure 5.8: Plots of the smallest eigenvalues of $\mathcal{A}_e[\mathbf{z}_\omega]$. Here ω_c is near 210 Hertz.

eigenvalue computations confirm. For $\omega \geq \omega_c$, we do not necessarily expect purely imaginary eigenvalues and in fact, we do observe eigenvalues with a real part. Eigenvalues with a real component are discussed below shortly.

In the plot on the left of Fig. 5.8, we can see the smallest eigenvalues are bounded away from 0 initially and then rapidly move toward 0 near 210 Hertz. At the point where they collide with 0, $\mathcal{A}_e[\mathbf{z}_\omega]$ has a loss of rank, which indicates ω_c. The plot on the right of Fig. 5.8 is a zoomed-in portion of the plot on the left. There we can see a series of Xs that increase in frequency as we approach $\omega_c \approx 210$ from the right. These Xs correspond to the i-peak standing wave solutions found by Oden and Lin, and where the Xs cross zero indicates the bifurcation speed ω_i where $\mathcal{A}_e[\mathbf{z}_\omega]$ is singular. The sporadic eigenvalues not corresponding to the Xs appear to be due the discretization of the equations and do not persist when the mesh is refined. Occasionally these eigenvalues have a non-zero real component, but we do not observe any of these eigenvalues with corresponding eigenvectors that are resolved by our mesh. If we plot only the eigenvalues that correspond to the $\omega_i, i = 2, \ldots, 12$, we obtain Fig. 5.9. We denote these eigenvalues as $\lambda_i(\omega)$ with complex conjugate $\bar{\lambda}_i(\omega)$. Note that $\lambda_i(\omega_i) = 0$. For each λ_i and $\bar{\lambda}_i$ there is a complex conjugate pair of eigenvectors. We refer to the eigenvectors as $\mathbf{e}_i(\omega)$ and we plot the real $\boldsymbol{\phi}$ component of two of the $\mathbf{e}_i$ in Fig. 5.10.

In addition to the standing wave eigenvectors with i peaks we discover other eigenvectors which correspond to other bifurcation speeds. We plot these eigenvectors in Fig. 5.11 and note that these eigenvectors have more complexity in the radial direction than the eigenvectors discovered by Oden and Lin. To investigate this, we note that the rotational symmetry of our problem implies that eigenvectors must have a certain form. Since $\mathbf{z}_\omega$ is axisymmetric, $\mathcal{A}_e[\mathbf{z}_\omega]$ commutes with a family of rotation operators $\mathcal{R}(\theta)$ defined by

$$\mathcal{R}(\theta) \begin{pmatrix} \hat{\boldsymbol{\phi}}(X) \\ \hat{\boldsymbol{\nu}}(X) \end{pmatrix} = \begin{pmatrix} \mathbf{R}(\theta)\hat{\boldsymbol{\phi}}(\mathbf{R}^\mathsf{T}(\theta)X) \\ \mathbf{R}(\theta)\hat{\boldsymbol{\nu}}(\mathbf{R}^\mathsf{T}(\theta)X) \end{pmatrix} . \tag{5.3}$$

Hence any eigenvector $\hat{\mathbf{z}} = (\hat{\boldsymbol{\phi}}, \hat{\boldsymbol{\nu}})$ of $\mathcal{A}_e$ associated to a distinct eigenvalue must also be an

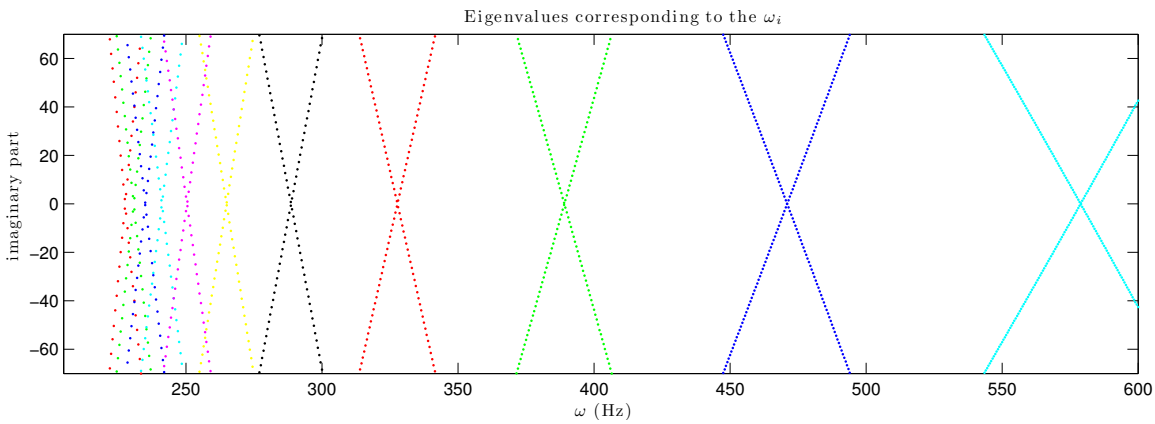

Figure 5.9: Plot of the λ_i and $\bar{\lambda}_i$. The leftmost X corresponds to λ_{12} while the rightmost X corresponds to λ_2.

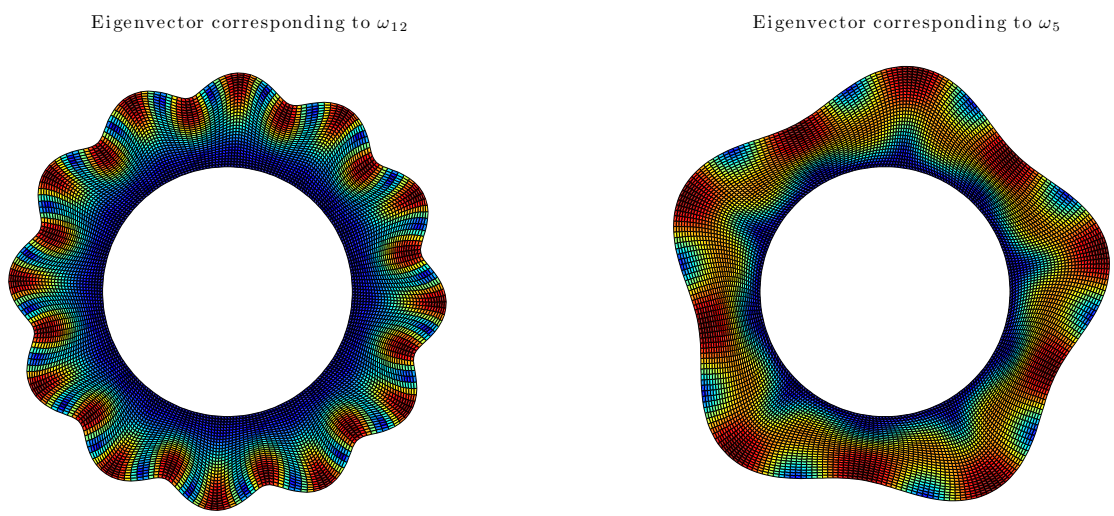

Figure 5.10: Plot of eigenvectors corresponding to ω_{12} and ω_5. The plots are colored according to the displacement from the reference configuration, with red being high displacment and blue being little displacement.

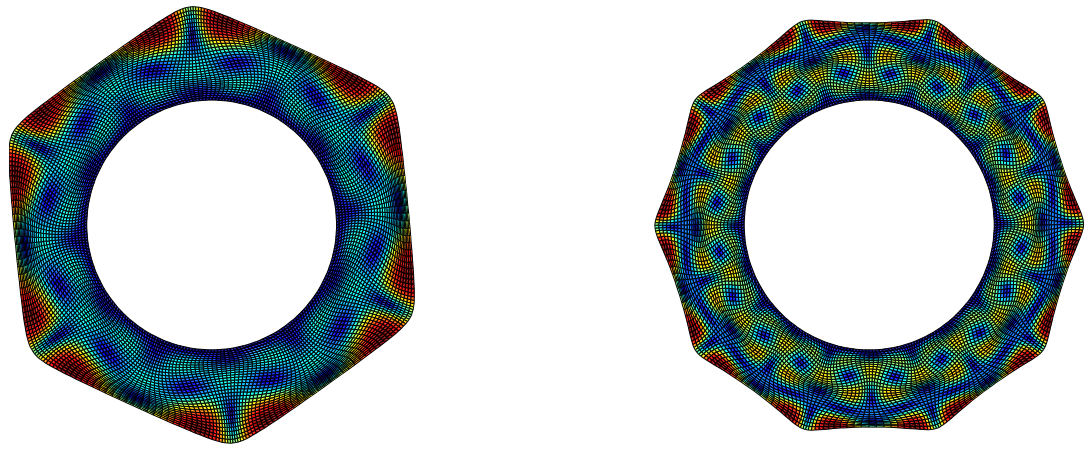

Figure 5.11: Plot of the real $\boldsymbol{\phi}$ component of eigenvectors outside of the N-peak hierarchy discoverd by Oden and Lin. The plots are colored according to the displacement from the reference configuration, with red being high displacment and blue being little displacement.

eigenvector of $\mathcal{R}(\theta)$ for all θ. This implies that $\hat{\mathbf{z}} = (\hat{\boldsymbol{\phi}}, \hat{\boldsymbol{\nu}})$, written as a function of polar coordinates, is of the form

$$\begin{aligned} \hat{\boldsymbol{\phi}}(r,\theta) &= a_1(r)e^{i(k+1)\theta}\begin{bmatrix} 1 \\ -i \end{bmatrix} + a_2(r)e^{i(k-1)\theta}\begin{bmatrix} 1 \\ i \end{bmatrix} \\ \hat{\boldsymbol{\nu}}(r,\theta) &= a_3(r)e^{i(k+1)\theta}\begin{bmatrix} 1 \\ -i \end{bmatrix} + a_4(r)e^{i(k-1)\theta}\begin{bmatrix} 1 \\ i \end{bmatrix} \end{aligned} \tag{5.4}$$

Here k is a fixed integer and the $a_i(r)$ are functions that depend only on the radial direction r. Also, it can be verified that the above eigenfunction is invariant with respect to $\mathcal{R}(\theta)$ for $\theta = 2\pi n/k$; hence the standing wave solutions with N peaks must be in the above form with $k = N$ or $k = -N$.

Given a numerically calculated eigenvector with N peaks, we can compute its Fourier series in the θ direction. As expected due to (5.4), we observe that all Fourier modes are 0 except for two modes: $N \pm 1$ or $-N \pm 1$. We repeat this computation for each value of r to determine the functions $a_i(r)$. By plotting the a_i we can compare the radial complexity of different eigenvectors. As in the upper left plot in Fig. 5.12, we observe the $a_i(r)$ corresponding to the $\mathbf{e}_i$ have one local extremum. The $a_i(r)$ corresponding to other eigenvectors has more radial complexity with $2, 3, 4$ or more local extrema.

We find an N-peak hierarchy of eigenfunctions with a_i having two local extrema. These eigenvalues are denoted $\mathbf{e}_{i,2}$ with corresponding eigenvalues and bifurcation speeds denoted by $\lambda_{i,2}$ and $\omega_{i,2}$, respectively. Fig. 5.13 shows the corresponding paths of their eigenvalues. As in Fig. 5.11 and 5.12, we find eigenvalues with more radial complexity than the $\mathbf{e}_{i,2}$. This suggests that the standing wave solutions may be described by a two-dimensional hierarcy $\mathbf{e}_{i,j}$; where i is the number of peaks in the circumreferential direction and j is the number

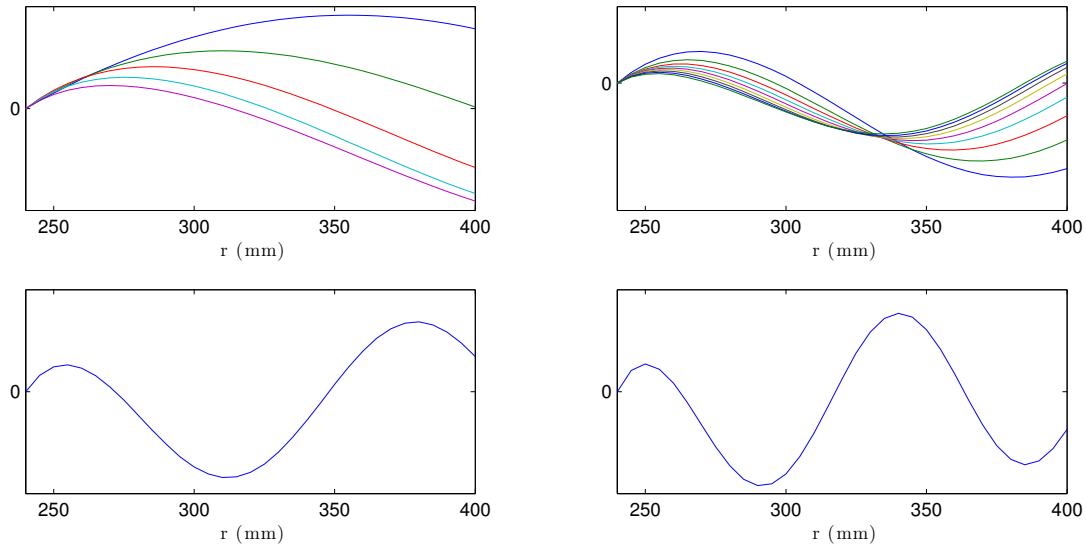

Figure 5.12: Plots of the real part of a_1 for various eigenvectors. The top left plot corresponds to the $\mathbf{e}_i$. The top right plot corresponds to N-peak bifurcations with extra radial complexity. The bottom plots correspond to eigenvectors with even greater radial complexity.

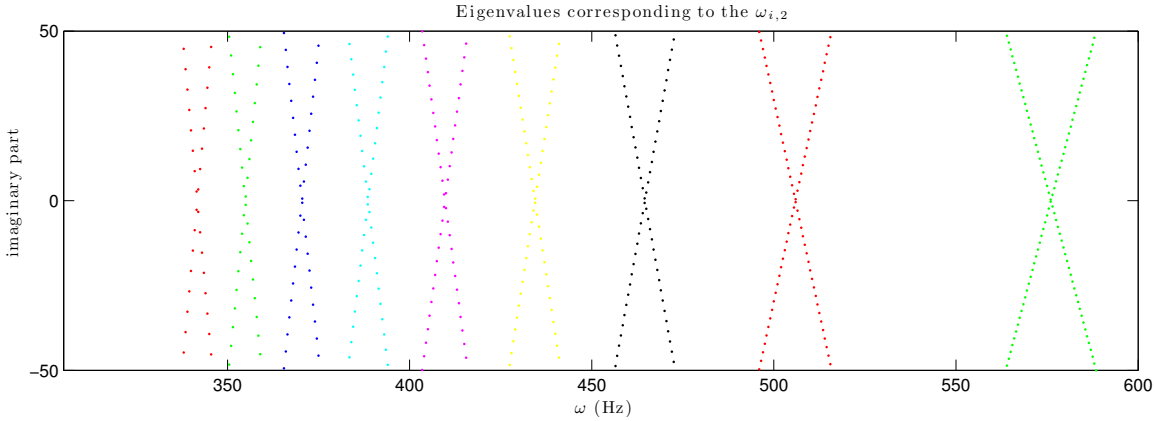

Figure 5.13: Plot of the $\lambda_{i,2}$ and $\bar{\lambda}_{i,2}$. The leftmost X corresponds to $\lambda_{12,2}$ while the rightmost X corresponds to $\lambda_{4,2}$.

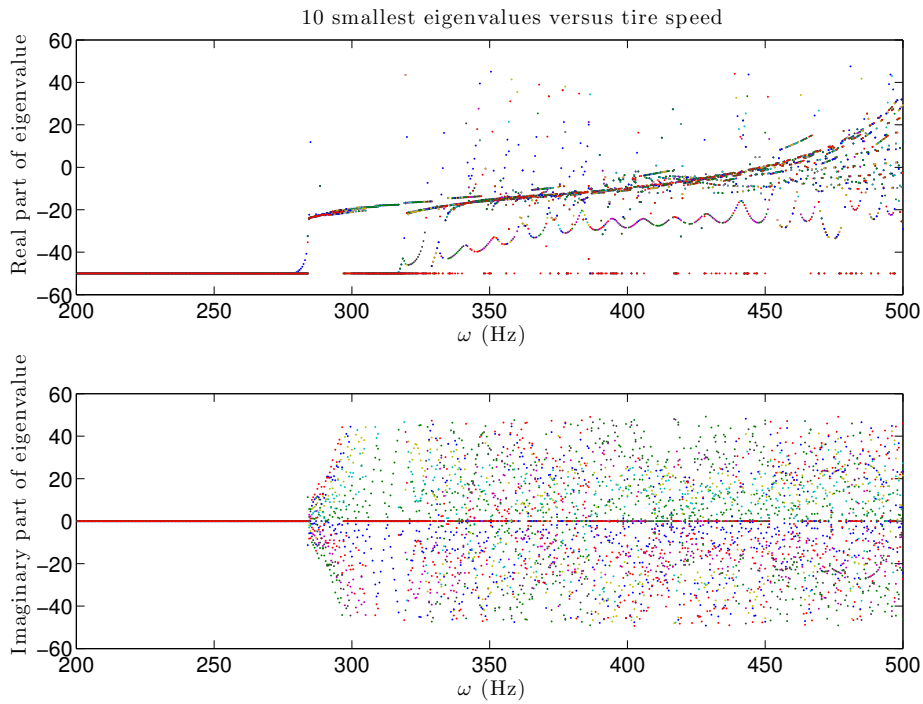

Figure 5.14: Plots of the smallest eigenvalues of $\mathcal{A}[\mathbf{z}_\omega^v]$ in the viscoelastic case. Here ω_c^v is near 285 Hertz.

of oscillations in the radial direction. It is an unresolved question whether the $\omega_{i,j}$ converge to ω_c as $i \to \infty$ for fixed j or if perhaps there is a distinct critical speed for each j.

Viscoelastic case

Adding viscoelasticity to the free spinning tire changes the eigenvalue picture considerably. We still find a single radially symmetric solution $\mathbf{z}_\omega^v$ for any tire speed ω, and we compute the eigenvalues of the operator $\mathcal{A}[\mathbf{z}_\omega^v]$, which we plot in Fig. 5.14.

One major difference between the eigenvalues in the elastic case (as in Fig. 5.8), is that the Hamiltonian structure is destroyed and we no longer expect purely imaginary eigenvalues. In fact, all of the eigenvalues we observe have a real component, there were no eigenvalues passing through 0, and the matrix $\mathcal{A}[\mathbf{z}_\omega^v]$ always remains non-singular. Thus we find no bifurcation speeds that lead to other steady state solutions. Yet there is still an event analogous to the critical bifurcation speed from above, at which point the many eigenvalues approach 0, although they do not pass through 0. We call this speed ω_c^v, which is approximately 285 hertz.

We also observe eigenvalues of $\mathcal{A}[\mathbf{z}_\omega^v]$, denoted λ_i^v, which are analagous to the λ_i of the elastic case. By "analagous", we mean that the imaginary part of the λ_i^v form Xs and the corresponding eigenvectors, denoted $\mathbf{e}_i^v$, have a similar structure to the $\mathbf{e}_i$. Unlike the $\mathbf{e}_i$, the

$\mathbf{e}_i^v$ have a viscoelastic stress component which we plot in Fig. 5.15.

As was the case with the λ_i, the λ_i^v correspond to a series of X's in the imaginary component of the eigenvalue plot. The X's increase in frequency as we approach ω_c^v and we call the speed where these X's cross zero ω_i^v. However, the ω_i^v are not bifurcation speeds, since their corresponding eigenvalues have a non-zero real component. Instead, we refer to them as pseudobifurcation speeds. We plot these eigenvalues in Fig. 5.16, and obtain a very similar picture to Fig. 5.9, with the addition of a real component.

As in the elastic case, we find eigenvectors and eigenvalues that do not correspond to the standing wave eigenvectors with i peaks identified by Oden and Lin. This suggests there is a two-dimensional hierarchy $\mathbf{e}_{i,j}^v$ in the viscoelastic setting as well as the elastic setting.

5.7 Instability of the linear viscoelastic model

Perhaps the most noteworthy observation from Fig. 5.16 is that the real part of the λ_i^v increases as we increase ω until the real part is greater than zero at ω_3^v, indicating an unstable mode.

We perturbed the stationary solution corresponding to tire speed 461 Hertz $\approx \omega_3^v$ in the direction $\mathbf{e}_3^v$ and allowed the tire to evolve with this initial configuration. Surprisingly, we observed the system exponentially gain energy to the point that our numerical time stepper returned NaNs. We observed the same phenomenon with any initial condition evolved at rotation speeds greater than approximately 420 Hertz.

Fig. 5.17 shows the exponential increase in elastic energy. To ensure that this nonphysical behavior of the linear viscoelastic model was not caused by any numerical issues, Fig. 5.17 shows the energy for several mesh sizes. Reducing the time step size and refining the mesh did not significantly affect the rate of exponential increase. We also repeated the experiment with the elastic model using analogous initial conditions: $\mathbf{z}_\omega$ perturbed in the direction $\mathbf{e}_3$ with tire speed $\omega = 470$ Hertz $\approx \omega_3$. Fig. 5.18 indicates that the elastic model shows no increase in energy and that the numerical simulation shows no signs of instability. These results provide evidence that it is the viscoelastic model itself that causes the nonphysical exponential increase in energy.

We recall that our viscoelastic model was proposed by Govindjee and Simo [15], which in turn is based on the theory of J.C. Simo [31]. The model of Simo is used in many finite element programs and similar approaches are taken [17, 18]. That this viscoelastic model can lead to increasing elastic energy is not as surprising if we consider the later work of Govindjee and Reese, which points out some of the drawbacks of the model of Simo. Govindjee and Reese note in [28] the linearity of the Simo's model restricts its validity to strain states near equilibrium and that it has not been proven that Simo's model satisfies the 2nd Law of Thermodynamics. At high speeds the strain state of our tire is far from equilibrium, hence it is plausible that Simo's model becomes invalid and leads to our observation of exponentially increasing elastic energy. To address these issues, Govindjee and Reese [29] proposed a nonlinear viscoelastic model which can be shown to satisfy the 2nd Law of

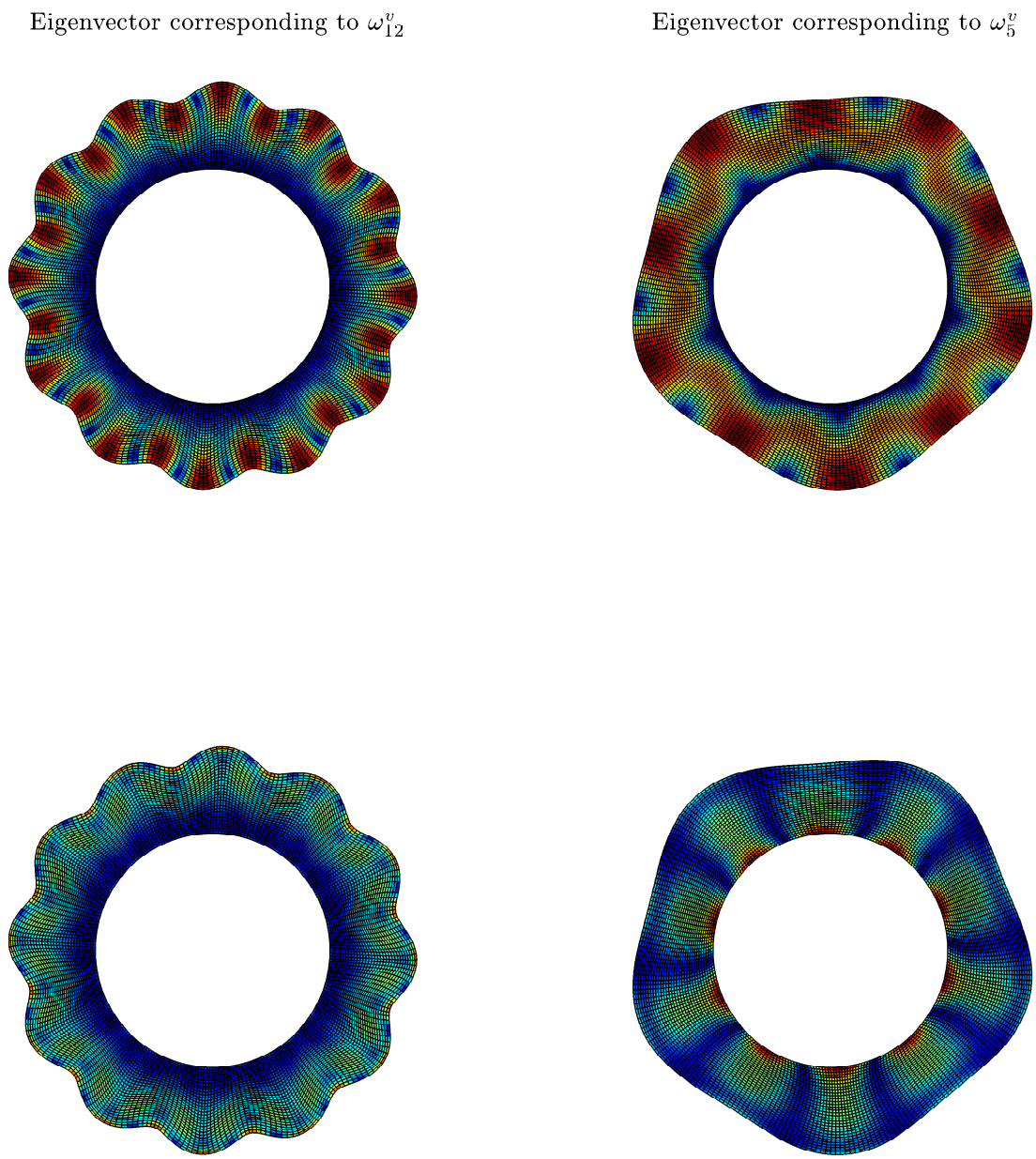

Figure 5.15: Plot of eigenvectors corresponding to ω_{12}^v and ω_5^v. The plots on the top are colored according to the displacement from the reference configuration, with red being high displacment and blue being little displacement. The plots below are colored according to the frobenius norm of the viscoelastic stress tensor.

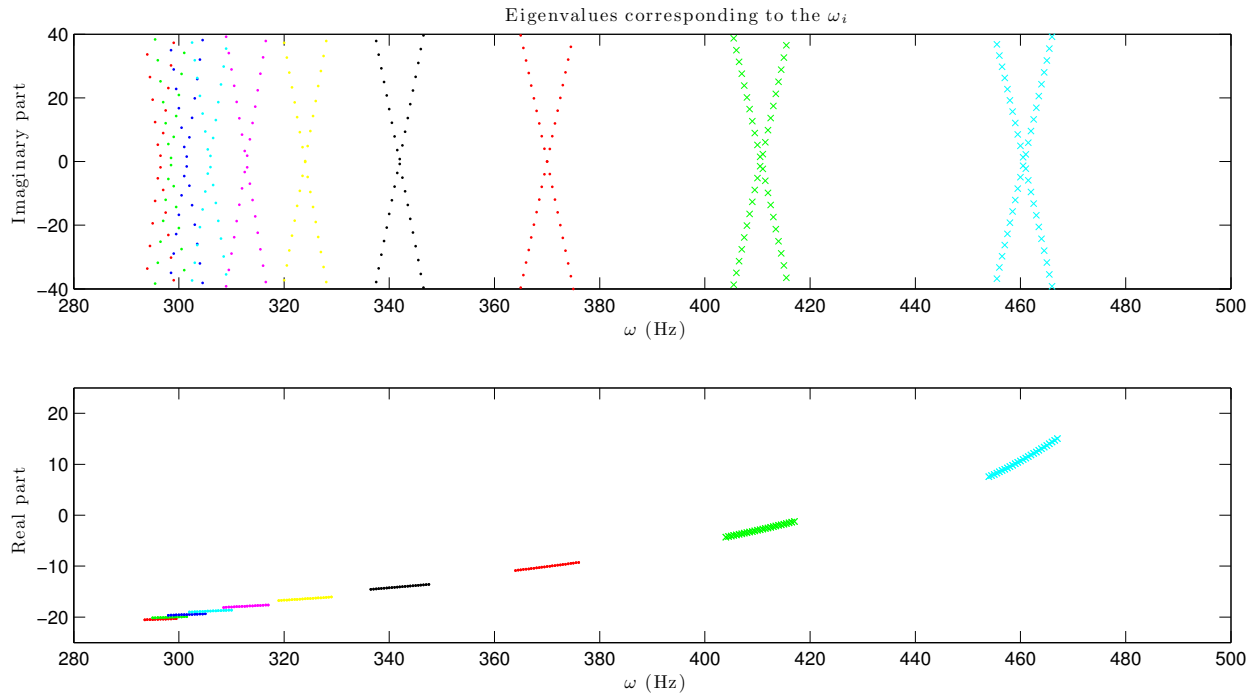

Figure 5.16: Plot of the real and imaginary components of the eigenvalues corresponding to the ω_i^v. The leftmost X corresponds to ω_{12}^v while the rightmost X corresponds to ω_3^v.

Thermodynamics. We shall refer to this model as the nonlinear model and refer to Simo's model as the linear model, which we described in §2.7. We apply the nonlinear model to our constitutive relations.

Recall the stored energy function $\mathbf{\Psi}_e$ from §2.6

$$\mathbf{\Psi}_e = \frac{\kappa}{4}\left(I_3 - \log I_3 - 1\right) + \frac{\mu}{2}(1-s)\left(I_1 - \log I_3 - 3\right) + \frac{\mu}{2}s\left(I_2 - 2\log I_3 - 3\right)\,, \tag{5.5}$$

which depends on the invariants I_1, I_2, I_3 of $\mathbf{C}$. In addition to $\mathbf{\Psi}_e$, consider a second stored energy function $\mathbf{\Psi}_v$ which depends on the invariants of an internal variable $\mathbf{b}_e$, I_1^e, I_2^e, I_3^e:

$$\mathbf{\Psi}_v = \nu\left(\frac{\kappa}{4}\left(I_3^e - \log I_3^e - 1\right) + \frac{\mu}{2}(1-s)\left(I_1^e - \log I_3^e - 3\right) + \frac{\mu}{2}s\left(I_2^e - 2\log I_3^e - 3\right)\right)\,. \tag{5.6}$$

In the plane strain case that we consider, the internal variable $\mathbf{b}_e$ is a tensor on $\mathbb{R}^2$ and the invariants I_1^e, I_2^e, I_3^e are obtained from the augmented tensor $\begin{bmatrix} \mathbf{b}_e & 0 \\ 0 & 1 \end{bmatrix}$.

As with the linear model, we can define the first Piola-Kirkhhoff stress tensor by

$$\mathbf{P} = \mathbf{P}_e + \mathbf{P}_v\,, \tag{5.7}$$

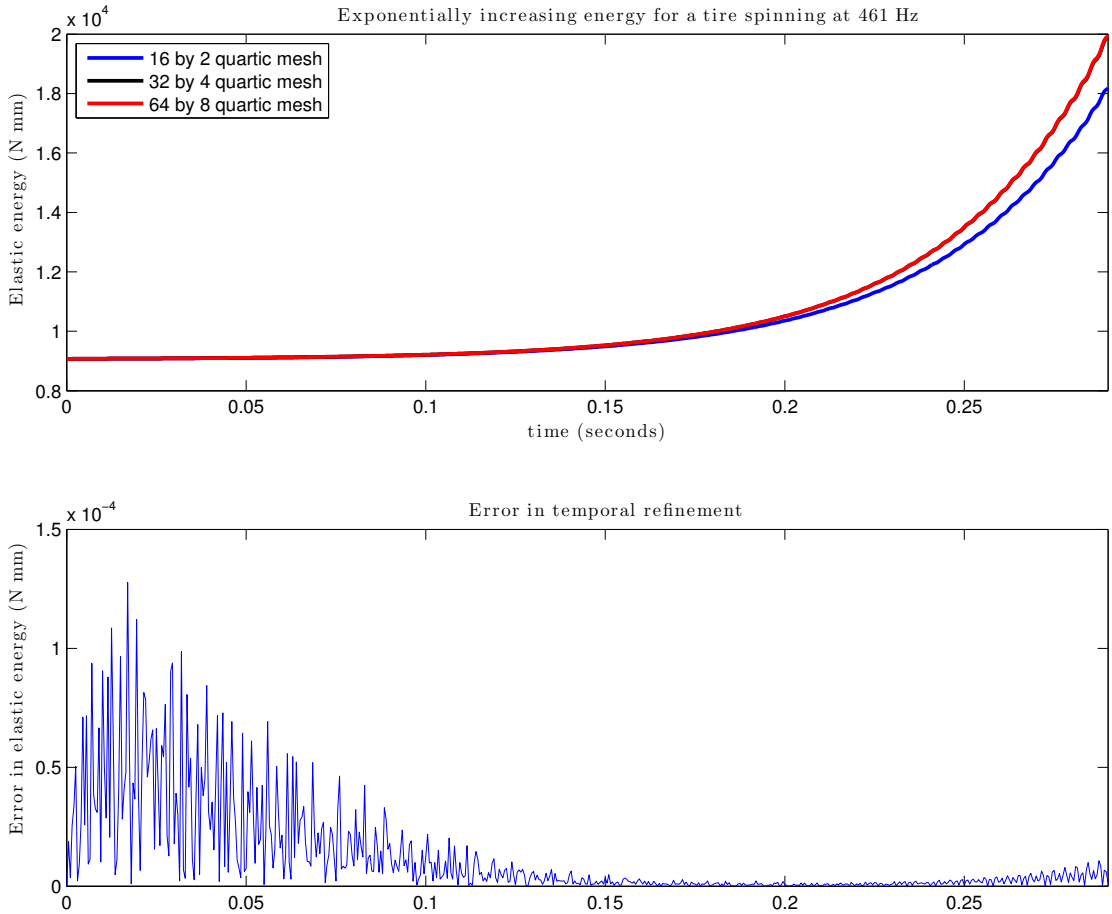

Figure 5.17: The upper plot shows the elastic energy for the steady state solution to the linear viscoelastic model perturbed in the direction of $\mathbf{e}_3^v$. We repeat the calculation for three mesh sizes. The discrepancy between the finer meshes is barely visible on the plot. The lower plot shows the error when halving the time step for the finest mesh.

where $\mathbf{P}_e$ is given by $\partial\mathbf{\Psi}_e/\partial\mathbf{F}$. In contrast to the linear model, $\mathbf{P}_v$ is now given by

$$\begin{aligned}\mathbf{P}_v &= 2\frac{\partial\mathbf{\Psi}_v}{\partial\mathbf{b}_e}\mathbf{b}_e\mathbf{F}^{-\mathsf{T}} \\ &= \nu\left(\frac{\kappa}{2}(I_3^e-1)\mathbf{I}+\mu(1-s)(\mathbf{b}_e-\mathbf{I})+\mu s(I_1^e\mathbf{b}_e-\mathbf{b}_e^2-2\mathbf{I})\right)\mathbf{F}^{-\mathsf{T}}\,.\end{aligned} \tag{5.8}$$

The model is complete given the dynamics for the interval variable $\mathbf{b}_e$:

$$\dot{\mathbf{b}}_e = \boldsymbol{\ell}\mathbf{b}_e + \mathbf{b}_e\boldsymbol{\ell}^{\mathsf{T}} - 2\mathcal{V}(\boldsymbol{\tau}_e)\mathbf{b}_e\,, \tag{5.9}$$

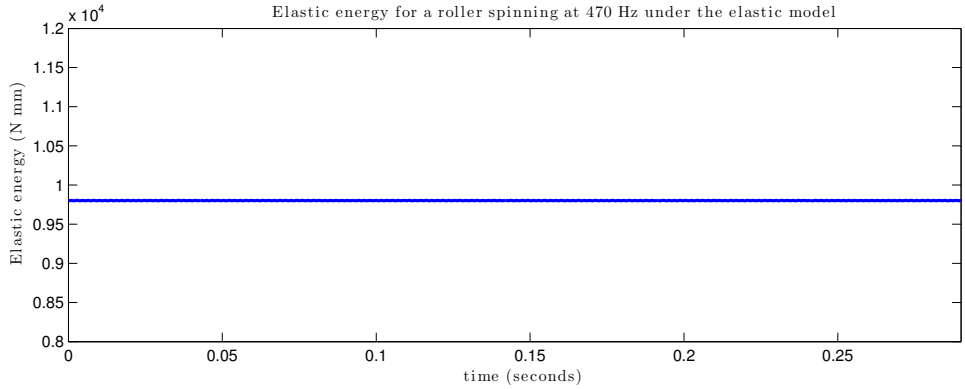

Figure 5.18: We plot the elastic energy for the steady state solution to the elastic model perturbed in the direction of $\mathbf{e}_3^v$. Unlike the viscoelastic case, the elastic energy does not increase.

where

$$\begin{aligned} \boldsymbol{\ell} &= \dot{\mathbf{F}}\mathbf{F}^{-1} \\ \boldsymbol{\tau}_e &= 2\frac{\partial \boldsymbol{\Psi}_v}{\partial \mathbf{b}_e}\mathbf{b}_e \\ \mathcal{V}(\boldsymbol{\tau}_e) &= C_1\left(\boldsymbol{\tau}_e - \frac{1}{2}(\operatorname{tr}\boldsymbol{\tau}_e)\mathbf{I}\right) + C_2\frac{1}{2}(\operatorname{tr}\boldsymbol{\tau}_e)\mathbf{I}\,. \end{aligned} \tag{5.10}$$

For positive constants C_1, C_2, it can be shown that for an evolution problem with free or Dirichlet boundary conditions, the total energy $\mathcal{E} = \int_{\mathcal{B}} \boldsymbol{\Psi}_e + \int_{\mathcal{B}} \boldsymbol{\Psi}_v + \frac{\rho_R}{2}\int_{\mathcal{B}} \boldsymbol{\nu}\cdot\boldsymbol{\nu}$ is non-increasing.

C_1 and C_2 control the volumetric and deviatoric viscoelastic response, respectively. We choose the constants C_1, C_2 so that the viscoelastic reponse for the nonlinear model approximately matches that of the linear model. To compare the response of the two models, we evolve two initial states with $\omega = 0$: one the expands the tire and one that twists the tire. The first state consists of an initial velocity that expands the tire radially. We then compare the radial displacement on the edge of the tire given by the two models. The second state consists of an initial velocity that twists the tire counterclockwise and we compare the vertical displacement of a point on the rightmost edge of the tire. The two initial states are intended to measure the volumetric and deviatoric viscoelastic responses, respectively.

We find that

$$C_1 = \frac{1}{2\mu\tau} \qquad C_2 = \frac{1}{2\kappa\tau} \tag{5.11}$$

gives very close agreement between the models for these initial states. In Fig. 5.19 and Fig. 5.20 we plot the results of these tests.

Given these choices of parameters, we evolve the nonlinear model under the same initial conditions and tire speed used to produce Fig. 5.17 and observed no blow up. We plot the

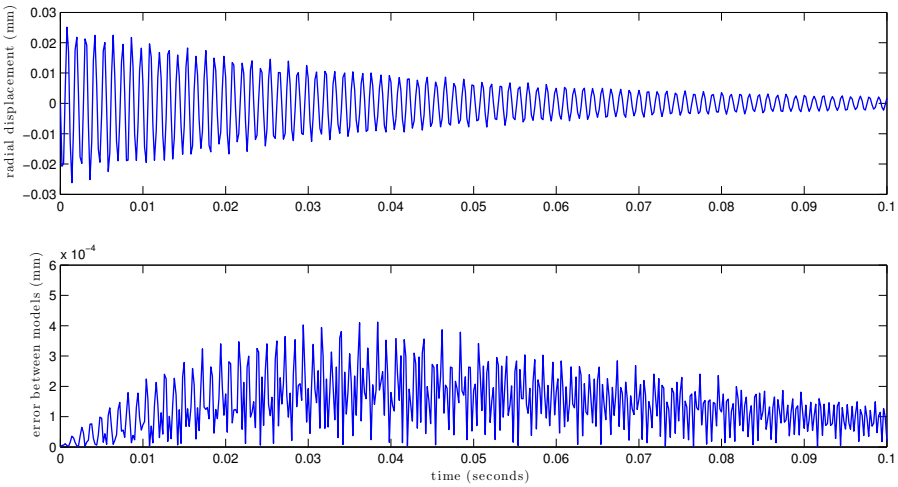

Figure 5.19: The top plot shows the radial displacement on the edge of the tire for the expanding initial state for the two viscoelasticity models. The bottom plot shows the error between the models. The error between the models is several orders of magnitude smaller than the displacement so that only a single plot can be seen in the top panel.

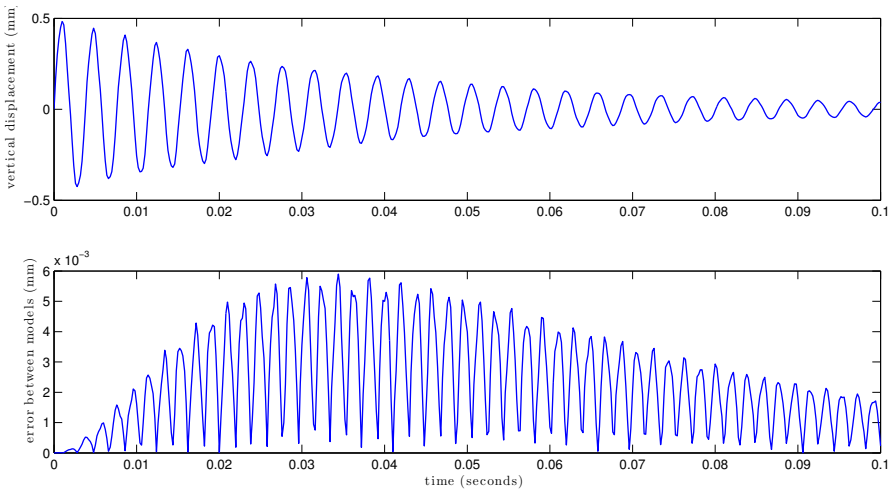

Figure 5.20: The top plot shows the vertical displacements of the rightmost edge of the tire for the twisting initial state. The bottom plot shows the error between the models. The error between the models is several orders of magnitude smaller than the displacement so that only a single plot can be seen in the top panel.

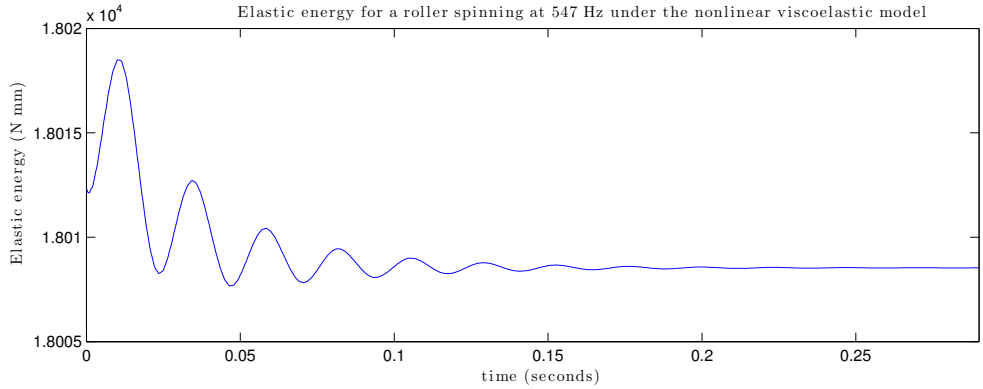

Figure 5.21: Plot of the elastic energy for the same initial condition as in Fig. 5.17, but using the nonlinear model of viscoelasticity. Unlike the linear viscoelastic model case, the elastic energy does not increase, on average.

evolution of the elastic energy according to the nonlinear model in Fig. 5.21. For a large range of viscoelastic parameters, we observed blow up in the linear model, but never in the nonlinear model.

We note that the nonlinear model fits into our entire numerical framework with no significant changes or major computational expense. The storage requirements are identical since instead of storing the symmetric matrix $\mathbf{Q}$ in the linear model, we store the symmetric matrix $\mathbf{b}_e$. There is a small percentage of extra computation due to the fact that the time evolution of $\mathbf{b}_e$ depends nonlinearly on $\mathbf{b}_e$, as opposed to the evolution of $\mathbf{Q}$ which is linear with respect to $\mathbf{Q}$. This is partially mitigated by the fact that the dependence of $\dot{\mathbf{b}}_e$ on $\boldsymbol{\phi}$ and $\boldsymbol{\nu}$ is simpler than than dependence of $\dot{\mathbf{Q}}$ on $\boldsymbol{\phi}$ and $\boldsymbol{\nu}$. Using the nonlinear viscoelastic model, we are able to compute time periodic solutions of the treaded tire and find stationary solutions.

In addition to computing time periodic solutions, we may also perform the same eigenvalue analysis with the nonlinear model as we did with the linear model in §5.6. Recall that with the linear viscoelastic model we observed in Fig. 5.16 eigenvalues with steadily increasing real part. Fig. 5.22 and Fig. 5.23 show the analogous picture for the nonlinear model. We observe that the real part of the eigenvalues for the nonlinear model remains negative and bounded well away from zero. The real part of an eignevalue associated with an N-peak solution decreases as ω increases, which is the opposite of the behavior in the linear model case.

We conclude that while the linear viscoelastic model works well for a large regime of tire speeds, there are conditions under which it can lead to a nonphysical increase in the elastic energy. The nonlinear model, which can be shown to satisfy the 2nd Law of Thermodynamics, exhibits no nonphysical increase in elastic energy.

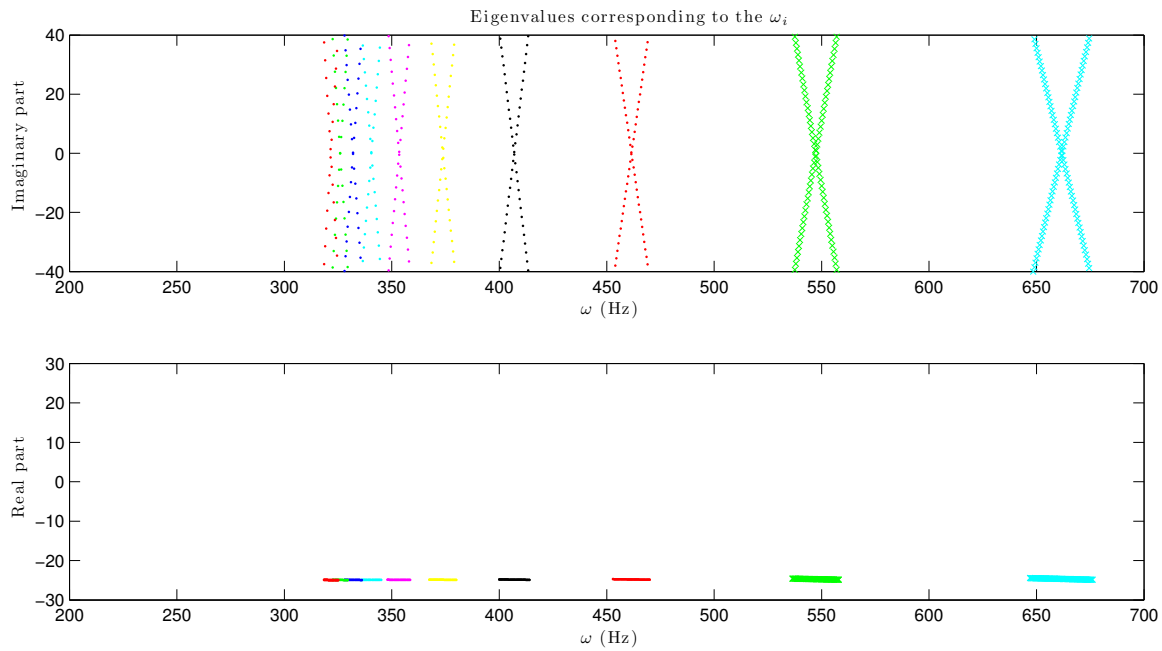

Figure 5.22: Plot of the real and imaginary components of the eigenvalues corresponding to the ω_i^v using the nonlinear viscoelastic model. The leftmost X corresponds to ω_{12}^v while the rightmost X corresponds to ω_3^v. The real part of the eigenvalues is negative, bounded well away from zero, and sloping downward.

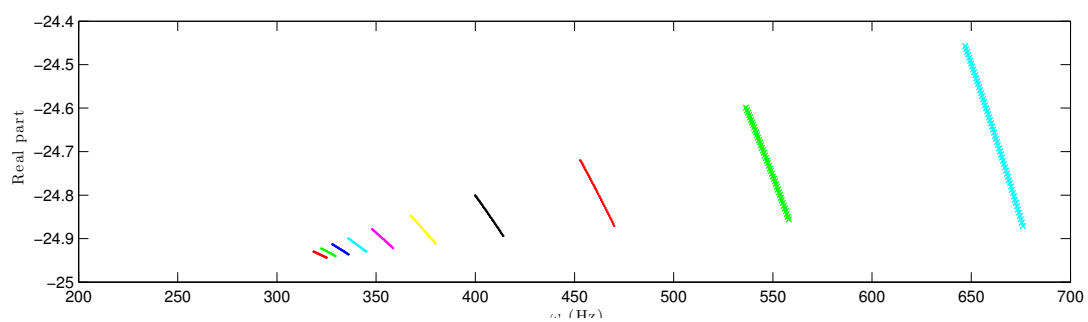

Figure 5.23: Rescaled version of the lower plot of 5.22, which shows the slope of the real part of the eigenvalues.

Chapter 6

Conclusions

We have described a framework to compute time periodic motions of a viscoelastic two-dimensional tire rolling on a road and we have applied two algorithms, Levenberg-Marquardt and Newton-Krylov, to find solutions. While the Levenberg-Marquardt algorithm is less sensitive to the viscoelastic parameters, the Newton-Krylov method is more efficient and scales well to large problems. Either of these methods can compute the motion and stresses for a steadily rolling treaded tire, for which the stationary solution approach does not apply. We are able to investigate the evolution of stresses along various points of the tire, such as tread peaks and troughs, as they come in contact with the road. The time periodic methodology naturally captures the fundamental oscillations of viscoelastic bodies.

Oden and Lin [24] discovered a class of N-peak standing wave stationary solutions for the free spinning elastic tire. We discover a larger class of standing wave solutions that display increasing radial complexity. Whereas Oden and Lin noticed N-peak standing waves due to the linearized operator becoming singular, we follow the corresponding eigenvalues that become 0. These eigenvalues are purely imaginary, which we prove for low speeds using the Hamiltonian structure of the problem. We repeat our analysis with the addition of viscoelasticity and discover that there are no standing wave solution bifurcations, but that eigenvalues persist with corresponding eigenvectors analagous the N-peak standing waves.

These eigenvalues have a non-zero real part due to the viscoelasticity, and we observe that at high tire speeds, the real part of these eigenvalues becomes greater than 0. This leads us to discover that our viscoelastic model, based on the linear viscoelastic model of J.C. Simo [31], can cause nonphsyical growth of the elastic energy of the tire. We implement a nonlinear model proposed by Govindjee and Reese [29] for which the 2nd Law of Thermodynamics can be proven. With this viscoelastic model, we do not observe any nonphysical growth and the real part of the eigenvalues corresponding to N-peak standing waves remains negative. For high tire speeds, we conclude that the nonlinear viscoelastic model is more appropriate.

Bibliography

[1] D. M. Ambrose and J. Wilkening, *Computation of symmetric, time-periodic solutions of the vortex sheet with surface tension*, Proc. Nat. Acad. Sci. (2009), (submitted).

[2] _____, *Computation of time-periodic solutions of the Benjamin-Ono equation*, J. Nonlinear Sci. (2009), (accepted).

[3] J.M. Ball, *Convexity conditions and existence theorems in nonlinear elasticity*, Arch. Rat. Mech. Anal. **63** (1977), 337–403.

[4] J.M. Bass, *Three-dimensional finite deformation, rolling contact of a hyperelastic cylinder: Formulation of the and computational results*, Computers and Structures **26** (1987), 991–1004.

[5] S. Blosser, M. Newman, T. McMahon, and R. Wassmer, *Estimating annual waste tire generation, diversion and disposal in California*, `http://www.ciwmb.ca.gov/agendas/mtgdocs/2007/04/00021853.ppt`, 2007.

[6] T. A. Davis and W. W. Hager, *Modifying a sparse Cholesky factorization*, SIAM Journal on Matrix Analysis and Applications **20** (1999), no. 3, 606–627.

[7] _____, *Multiple-rank modifications of a sparse Cholesky factorization*, SIAM Journal on Matrix Analysis and Applications **22** (2001), no. 4, 997–1013.

[8] _____, *Row modifications of a sparse Cholesky factorization*, SIAM Journal on Matrix Analysis and Applications **26** (2005), no. 3, 621–639.

[9] _____, *Dynamic supernodes in sparse Cholesky update/downdate and triangular solves*, ACM Trans. Math. Software **35** (2009), no. 4.

[10] J.R. Dormand and P.J. Prince, *A family of embedded runge-kutta formulae*, J. Comput. Appl. Math. **6** (1980), 19–26.

[11] _____, *Practical runge-kutta processes*, SIAM J. Sci. and Stat. Comput. **10** (1989), 977–989.

[12] L.O. Faria, J.T. Oden, B. Yavari, W.W. Tworzydlo, J.M. Bass, and E.B. Becker, *Tire modeling by finite elements*, Tire Science and Technology **20** (1992), 33–56.

[13] S. Govindjee, *Firestone tire failure analysis*, Tech. report, 2001, (http://www.ce.berkeley.edu/∼sanjay/REPORT_WEB_Secure.PDF).

[14] S. Govindjee and P.A. Mihalic, *Viscoelastic constitutive relations for the steady spinning of a cylinder*, Tech. Report UCB/SEMM-98/02, 1998.

[15] S. Govindjee and J.C. Simo, *Mullins' effect and the strain amplitude dependence of the storage modulus*, Int. J. Solids Struct. **29** (1992), 1737–1751.

[16] E. Hairer, S. P. Nørsett, and G. Wanner, *Solving ordinary differential equations I. Nonstiff problems*, Springer-Verlag, 1987.

[17] G.A. Holzapfel, *On large strain viscoelasticity: continuum formulation and finite element applications to elastomeric structures*, International Journal for Numerical Methods in Engineering **39** (1996), 3903–3926.

[18] M. Kaliske and H. Rothert, *Formulation and implementation of three-dimensional viscoelasticity at small and finite strains*, Computational Mechanics **19** (1997), 238–239.

[19] R. Kennedy and J. Padovan, *Finite element analysis of steady and transiently moving/rolling nonlinear viscoelastic structure–ii. shell and three-dimensional simulations*, Computers and Structures **27** (1987), 249–257.

[20] P. Le Tallec and C. Rahier, *Numerical models of steady rolling for non-linear viscoelastic structures in finite deformations*, **37** (1994), 1159–1186.

[21] Xiaoye S. Li and James W. Demmel, *SuperLU_DIST: A scalable distributed-memory sparse direct solver for unsymmetric linear systems*, ACM Trans. Mathematical Software **29** (2003), no. 2, 110–140.

[22] F. DE S. Lynch, *A finite element method of viscoelastic stress analysis with application to rolling contract problems*, **1** (1969), 379–394.

[23] J. Marsden and T.J.R. Hughes, *Mathematical foundations of elasticity*, Prentice-Hall, Inc., Englewood Cliffs, New Jersey, 1983.

[24] J.T. Oden and R. Lin, *On the general rolling contact problem for finite deformations of a viscoelastic cylinder*.

[25] Saftey Assurance Office of Defect Investigation, *Engineering analysis report and initial decision regarding EA00-023: Firestone wilderness AT tires*, US Department of Transportation, National Highway Traffic Safety Administration, 2001.

[26] J. Padovan, *Finite element analysis of steady and transiently moving/rolling nonlinear viscoelastic structure–i. theory*, Computers and Structures **27** (1987), 249–257.

[27] J. Padovan and O. Paramodilok, *Transient and steady state viscoelastic rolling contact*, Computers and Structures **20** (1985), 545–553.

[28] S. Reese and S. Govindjee, *A presentation and comparison of two large deformation viscoelastic models*, ASME J. Engng. Mat. Tech. **119** (1997), 251–255.

[29] _____, *A theory of finite viscoelasticity and numerical aspects*, Int. J. Solids Structures **35** (1998), 3455–3482.

[30] T. Qi S. Müller and B.S. Yan, *On a new class of elastic deformations not allowing for cavitation*, Ann. Inst. Henri Poincaré (C) Analyse Nonlinéaire **11.2** (1994), 217–243.

[31] J.C. Simo, *On a fully three-dimensional finite-strain viscoelastic damage model: Formulation and computational aspects*, Comp. Meth. Appl. Mech. Engng. **60** (1987), 153–173.

[32] W. W. Hager Y. Chen, T. A. Davis and S. Rajamanickam, *Algorithm 887: Cholmod, supernodal sparse Cholesky factorization and update/downdate*, ACM Trans. Math. Software **35** (2009), no. 3.

Appendix A

The linearized equations

Recall the linearized equations (2.52):

$$
\begin{aligned}
\int_{\mathcal{B}} \dot{\hat{\boldsymbol{\phi}}} \cdot \zeta &= \int_{\mathcal{B}} \hat{\boldsymbol{\nu}} \cdot \zeta \\
\int_{\mathcal{B}} \rho_R \dot{\hat{\boldsymbol{\nu}}} \cdot \eta &= -\int_{\mathcal{B}} \widehat{\mathbf{P}} : D\eta + \int_{\Gamma_e} \widehat{\mathbf{h}} \cdot \eta \\
\int_{\mathcal{B}} \dot{\widehat{\mathbf{Q}}} : K &= \int_{\mathcal{B}} \left(-\frac{1}{\tau} \widehat{\mathbf{Q}} + \widehat{\dot{\mathbf{S}}}_e \right) : K \,.
\end{aligned}
\tag{A.1}
$$

We explicitly compute $\widehat{\mathbf{P}}, \widehat{\dot{\mathbf{S}}}_e$, and $\widehat{\mathbf{h}}$. We need several series of computations. The first set culminates in the computation of $\widehat{\mathbf{P}}$:

$$
\begin{aligned}
\widehat{\mathbf{F}} &= D\widehat{\boldsymbol{\phi}} \\
\widehat{\mathbf{C}} &= \widehat{\mathbf{F}}^{\mathsf{T}} \mathbf{F} + \mathbf{F}^{\mathsf{T}} \widehat{\mathbf{F}} \\
\widehat{I}_1 &= 2(\mathbf{F} : \widehat{\mathbf{F}}) \\
\widehat{I}_3 &= \widehat{\det \mathbf{C}} = 2I_3(\mathbf{F}^{-\mathsf{T}} : \widehat{\mathbf{F}}) \\
\widehat{\mathbf{F}^{-\mathsf{T}}} &= -\mathbf{F}^{-\mathsf{T}} \widehat{\mathbf{F}}^{\mathsf{T}} \mathbf{F}^{-\mathsf{T}} \\
\widehat{\mathbf{P}}_e &= \frac{\kappa}{2}(\widehat{I}_3 \mathbf{F}^{-\mathsf{T}} + (I_3 - 1)\widehat{\mathbf{F}^{-\mathsf{T}}}) \\
&\quad + \mu(1-s)(\widehat{\mathbf{F}} - \widehat{\mathbf{F}^{-\mathsf{T}}}) + \mu s(\widehat{I}_1 \mathbf{F} + I_1 \widehat{\mathbf{F}} - (\mathbf{F}\widehat{\mathbf{C}} + \widehat{\mathbf{F}}\mathbf{C}) - 2\widehat{\mathbf{F}^{-\mathsf{T}}}) \\
\widehat{\mathbf{P}}_v &= \nu \left(\widehat{\mathbf{F}} \mathbf{Q} + \mathbf{F} \widehat{\mathbf{Q}} \right) \\
\widehat{\mathbf{P}} &= \widehat{\mathbf{P}}_e + \widehat{\mathbf{P}}_v \,.
\end{aligned}
$$

The second set of computations culminates in $\widehat{\dot{\mathbf{S}}}_e$:

$$
\begin{aligned}
\widehat{\dot{\mathbf{F}}} &= D\widehat{\boldsymbol{\nu}} \\
\widehat{\dot{\mathbf{C}}} &= \widehat{\dot{\mathbf{F}}}^{\mathsf{T}}\mathbf{F} + \dot{\mathbf{F}}^{\mathsf{T}}\widehat{\mathbf{F}} + \widehat{\mathbf{F}}^{\mathsf{T}}\dot{\mathbf{F}} + \mathbf{F}^{\mathsf{T}}\widehat{\dot{\mathbf{F}}} \\
\widehat{\mathbf{C}^{-1}} &= -\mathbf{C}^{-1}\widehat{\mathbf{C}}\mathbf{C}^{-1} \\
\widehat{\dot{\mathbf{C}^{-1}}} &= -\widehat{\mathbf{C}^{-1}}\dot{\mathbf{C}}\mathbf{C}^{-1} - \mathbf{C}^{-1}\widehat{\dot{\mathbf{C}}}\mathbf{C}^{-1} - \mathbf{C}^{-1}\dot{\mathbf{C}}\widehat{\mathbf{C}^{-1}} \\
\widehat{\dot{\det \mathbf{C}}} &= \widehat{\det \mathbf{C}}\,\mathrm{tr}\left(\mathbf{C}^{-1}\dot{\mathbf{C}}\right) + \det \mathbf{C}\,\mathrm{tr}\left(\widehat{\mathbf{C}^{-1}}\dot{\mathbf{C}} + \mathbf{C}^{-1}\widehat{\dot{\mathbf{C}}}\right) \\
\widehat{\dot{\mathbf{S}}}_e &= \frac{\kappa}{2}\left[(\widehat{\dot{\det \mathbf{C}}})\mathbf{C}^{-1} + (\dot{\det \mathbf{C}})\widehat{\mathbf{C}^{-1}} + (\widehat{\det \mathbf{C}})\dot{\mathbf{C}^{-1}} + (\det \mathbf{C} - 1)\widehat{\dot{\mathbf{C}^{-1}}}\right] \\
&\quad + \mu(1-s)\left(-\widehat{\dot{\mathbf{C}^{-1}}}\right) + \mu s\left((\mathrm{tr}\,\widehat{\dot{\mathbf{C}}})\mathbf{I} - \widehat{\dot{\mathbf{C}}} - 2\widehat{\dot{\mathbf{C}^{-1}}}\right).
\end{aligned}
$$

Thirdly, we compute $\widehat{\mathbf{h}}$.

$$
\begin{aligned}
\widehat{x}_2 &= \widehat{\boldsymbol{\phi}}_2 \\
\widehat{\mathbf{h}} &= -\delta\gamma'(-h - x_2)\widehat{x}_2\mathbf{e}_2\,.
\end{aligned}
$$

Recall for the nonlinear viscoelastic model of Govindjee and Reese, we have that

$$
\begin{aligned}
\mathbf{P}_v &= \nu\left(\frac{\kappa}{2}(I_3^e - 1)\mathbf{I} + \mu(1-s)(\mathbf{b}_e - \mathbf{I}) + \mu s(I_1^e\mathbf{b}_e - \mathbf{b}_e^2 - 2\mathbf{I})\right)\mathbf{F}^{-\mathsf{T}} = \boldsymbol{\tau}_e\mathbf{F}^{-1} \\
\dot{\mathbf{b}}_e &= \boldsymbol{\ell}\mathbf{b}_e + \mathbf{b}_e\boldsymbol{\ell}^{\mathsf{T}} - 2\mathcal{V}(\boldsymbol{\tau}_e)\mathbf{b}_e\,.
\end{aligned}
$$

We compute $\dot{\widehat{\mathbf{b}}}_e$ and $\widehat{\mathbf{P}}_v$:

$$
\begin{aligned}
\widehat{I_1^e} &= (\widehat{\mathbf{b}}_e : \mathbf{I}) \\
\widehat{I_3^e} &= I_3^e(\mathbf{b}_e^{-1} : \widehat{\mathbf{b}}_e) \\
\widehat{\boldsymbol{\tau}_e} &= \nu\left(\frac{\kappa}{2}\widehat{I_3^e}\mathbf{I} + \mu(1-s)\widehat{\mathbf{b}}_e + \mu s(\widehat{I_1^e}\mathbf{b}_e + I_1^e\widehat{\mathbf{b}}_e - (\mathbf{b}_e\widehat{\mathbf{b}}_e + \widehat{\mathbf{b}}_e\mathbf{b}_e))\right) \\
\widehat{\mathbf{P}_v} &= \boldsymbol{\tau}_e\widehat{\mathbf{F}^{-\mathsf{T}}} + \widehat{\boldsymbol{\tau}_e}\mathbf{F}^{-\mathsf{T}} \\
\widehat{\boldsymbol{\ell}} &= \widehat{\dot{\mathbf{F}}}\mathbf{F}^{-1} + \dot{\mathbf{F}}\widehat{\mathbf{F}^{-1}} \\
\widehat{\mathcal{V}(\boldsymbol{\tau}_e)} &= \frac{1}{2\mu\tau}\left(\widehat{\boldsymbol{\tau}_e} - \frac{1}{2}(\mathrm{tr}\,\widehat{\boldsymbol{\tau}_e})\mathbf{I}\right) + \frac{1}{4\kappa\tau}(\mathrm{tr}\,\widehat{\boldsymbol{\tau}_e})\mathbf{I} \\
\dot{\widehat{\mathbf{b}}}_e &= \widehat{\boldsymbol{\ell}\mathbf{b}_e} + \widehat{\mathbf{b}_e\boldsymbol{\ell}^{\mathsf{T}}} - 2\widehat{\mathcal{V}(\boldsymbol{\tau}_e)\mathbf{b}_e} \\
&= (\widehat{\boldsymbol{\ell}}\mathbf{b}_e + \boldsymbol{\ell}\widehat{\mathbf{b}}_e) + (\widehat{\mathbf{b}}_e\boldsymbol{\ell}^{\mathsf{T}} + \mathbf{b}_e\widehat{\boldsymbol{\ell}^{\mathsf{T}}}) - 2(\widehat{\mathcal{V}(\boldsymbol{\tau}_e)}\mathbf{b}_e + \mathcal{V}(\boldsymbol{\tau}_e)\widehat{\mathbf{b}}_e)\,.
\end{aligned}
$$